

POLITECNICO DI MILANO  
Scuola di Ingegneria Industriale e dell'Informazione  
Corso di Laurea Magistrale in Engineering Physics  
Dipartimento di Fisica



# Resonant Micro-Opto-Mechanical Modulators and Switches by Femtosecond Laser Micromachining

Advisor: Dr. Roberto OSELLAME  
Co-Advisor: Dr. Andrea CRESPI

Thesis by:  
Riccardo MOTTA  
Matr. 898010

Academic Year 2018–2019



# Sommario

La microfabbricazione con laser a femtosecondi si è distinta, sin dalla sua nascita negli ultimi anni novanta, come uno strumento potente e versatile per la protipazione di dispositivi integrati. Questa tecnica è basata sull'impiego di impulsi laser a femtosecondi, focalizzati tramite un obiettivo da microscopio, per ottenere modifiche permanenti e localizzate dei materiali. La natura nonlineare dell'interazione fra gli impulsi laser e il materiale trasparente confina la regione di alterazione al punto focale, permettendo modifiche della parte interna del materiale senza interessarne la superficie e donando così alla tecnica ottime capacità di modellazione tridimensionale. Controllando i parametri di irraggiamento è possibile ottenere diversi tipi di alterazione del materiale, come modifiche di indice di rifrazione, cambi di fase, modifiche strutturali e formazione di vuoti. Inoltre, le dimensioni e i costi ridotti dell'apparato, uniti alla rapidità del processo di fabbricazione sono caratteristiche ideali per la protipazione dei dispositivi.

Tramite questa tecnica sono stati realizzati circuiti integrati in guida d'onda ad elevata complessità, con applicazioni che vanno dall'astrofotonica alla validazione sperimentale di modelli quantistici. La scrittura di guide d'onda per mezzo della modifica di indice di rifrazione è solo una delle possibilità di questa tecnica. In particolari condizioni di irraggiamento, e su particolari tipi di substrato, è possibile impiegare la tecnica cosiddetta FLICE (Femtosecond Laser Irradiation followed by Chemical Etching), con la quale si possono scavare microcanali con geometrie tridimensionali, sottraendo chimicamente e selettivamente la parte irradiata. Questo ha aperto la strada alla creazione di dispositivi microfluidici e dei cosiddetti lab-on-a-chip, per applicazioni d'avanguardia nell'analisi chimica e biologica. La possibilità di rimuovere materiale creando vuoti in praticamente ogni substrato ha arricchito ancor più lo spettro delle applicazioni di questa tecnica.

Dispositivi capaci di modulare o commutare il segnale ottico in guida d'onda, o in fibra, sono richiesti in numerose applicazioni. Nel vetro, a causa della mancanza di nonlinearietà e di proprietà conduttive, questo è ottenuto solitamente con un cambio di fase all'interno di una struttura interferometrica, attraverso la variazione di indice di rifrazione indotta da un riscaldamento localizzato. La grande limitazione di questi dispositivi è che, nella maggior parte dei casi, hanno tempi di risposta lenti, causati dalla dinamica della diffusione termica (che è nell'ordine dei millisecondi).

Lo scopo di questo lavoro è di indurre la modulazione o la commutazione di un segnale ottico attraverso l'oscillazione di microstrutture meccaniche. Sfruttando la risonanza di queste strutture ci aspettiamo di superare le limitazioni imposte dall'attuazione termica. L'idea generale dietro a questo lavoro è quella di sfruttare per la modulazione una guida d'onda, all'interno di un cantilever di dimensioni micrometriche, allineata perfettamente a una guida d'uscita davanti alla struttura. L'oscillazione meccanica dell'asta consente di modulare l'accoppiamento della luce fra le due guide inducendo un disallineamento laterale delle due. Analogamente, realizzeremo un commutatore opto-meccanico utilizzando due guide d'uscita, anziché una.

Nel primo capitolo è presentato un breve riassunto degli aspetti più rilevanti della teoria delle guide d'onda, seguito da un'introduzione alle tecnologie all'avanguardia nell'ambito dei commutatori, dove è data particolare attenzione ai sistemi micro-opto-elettro-meccanici (MOEMS). In seguito, sono presentati alcuni aspetti rilevanti della teoria usata per modellare le oscillazioni meccaniche in un'asta. Il primo capitolo si conclude con la presentazione di un modulatore micro-opto-meccanico, realizzato presso i laboratori del Dipartimento di Fisica nei mesi precedenti a questo lavoro di tesi, e su cui quest'ultimo trae il suo sviluppo.

Nel secondo capitolo, è presentata la microfabbricazione con laser a femtosecondi, sottolineando le sue capacità di microstrutturazione e gli aspetti più importanti dell'interazione radiazione-materia che la riguardano; sono poi presentati alcuni dispositivi esemplificativi.

L'apparato utilizzato e i metodi applicati durante la fabbricazione e la caratterizzazione dei dispositivi sono presentati nel terzo capitolo.

Il quarto capitolo riguarda l'analisi e lo sviluppo del modulatore ottico integrato, con il processo sperimentale utilizzato per ottimizzarlo. Si è ottenuto così un modulatore in grado di mostrare un contrasto tra picchi e minimi di 17 dB ad una frequenza di 72 kHz.

Il dispositivo ottimizzato è stato quindi usato come punto di partenza per la progettazione del direzionatore micro-opto-meccanico. Nel quinto capitolo, si presenta la progettazione del commutatore a due guide d'onda, assieme alla scelta sperimentale dei parametri utilizzati col fine di ottenere un dispositivo completo. Si è ottenuto così un prototipo in grado di commutare il segnale tra due guide di uscita in un tempo di 10  $\mu$ s, con un contrasto di 10 dB.

# Contents

<b>Sommario</b>	<b>I</b>
<b>List of figures</b>	<b>VII</b>
<b>List of tables</b>	<b>XIII</b>
<b>Introduction</b>	<b>1</b>
<b>1 Integrated-optics modulators and switches</b>	<b>3</b>
1.1 Waveguide optics . . . . .	3
1.1.1 Waveguide theory . . . . .	3
1.1.2 Losses in real devices . . . . .	6
1.1.3 Coupled-mode theory . . . . .	7
1.1.4 Fabrication technologies . . . . .	8
1.2 Integrated modulators and switches: state of the art . . . . .	10
1.2.1 Relevant figures of merit . . . . .	10
1.2.2 Technological overview . . . . .	11
1.2.3 MOEMS switches . . . . .	13
1.3 Oscillating cantilever . . . . .	17
1.3.1 The harmonic oscillator . . . . .	17
1.3.2 Damping and Q-factor . . . . .	18
1.3.3 Euler-Bernoulli beam theory . . . . .	19
1.3.4 Oscillation of cantilever beam . . . . .	20
1.3.5 Relation between models . . . . .	22
1.4 Cantilever modulators by femtosecond laser pulses: realized prototype	22
1.4.1 Device design and operation . . . . .	22
1.4.2 Realized prototype . . . . .	25
<b>2 Femtosecond laser micromachining</b>	<b>27</b>
2.1 Laser-matter interaction . . . . .	27
2.1.1 Absorption processes . . . . .	28
2.1.2 Optical breakdown and material modification . . . . .	29
2.1.3 Effect of irradiation parameters on the process . . . . .	30
2.2 Microstructuring capabilities . . . . .	33

2.2.1	Refractive index modification and waveguide writing . . . . .	33
2.2.2	Birefringent structures, nanogratings and FLICE . . . . .	34
2.2.3	Water assisted ablation . . . . .	35
2.3	Examples of devices . . . . .	37
<b>3</b>	<b>Materials and methods</b>	<b>43</b>
3.1	Fabrication setup . . . . .	43
3.1.1	Scheme of the apparatus . . . . .	43
3.1.2	Femtosecond laser source . . . . .	44
3.1.3	Translation stages . . . . .	45
3.2	Characterization of microstructures . . . . .	47
3.2.1	Optical microscope . . . . .	47
3.2.2	Actuation of resonant structures . . . . .	47
3.3	Characterization of waveguide device . . . . .	48
3.3.1	Microscope observation . . . . .	48
3.3.2	Optical transmission . . . . .	49
3.3.3	Guided mode . . . . .	49
3.3.4	Losses . . . . .	50
3.3.5	Coupling between waveguides . . . . .	50
3.4	Fiber-pigtailing . . . . .	52
<b>4</b>	<b>Optimization of the intensity modulator</b>	<b>55</b>
4.1	Analysis of previous cantilever modulators . . . . .	55
4.2	Maximization of the Extinction Ratio . . . . .	57
4.2.1	Waveguide optimization . . . . .	57
4.2.2	Maximization of the displacement . . . . .	57
4.2.3	Modulation improvement . . . . .	58
4.3	Asymmetry correction . . . . .	60
4.3.1	Analysis of the problem . . . . .	60
4.3.2	Correction of the fabrication method . . . . .	63
4.4	Fabrication and characterization of an optimized device . . . . .	66
<b>5</b>	<b>Design and realization of a resonant switch</b>	<b>75</b>
5.1	Design of the micro-opto-mechanical device . . . . .	75
5.1.1	Design constraints . . . . .	75
5.1.2	Quantitative considerations on the waveguides distance . . . . .	77
5.1.3	Design choices for managing the evanescent coupling . . . . .	79
5.1.4	Expected performance . . . . .	80
5.2	Optimization of design parameters . . . . .	81
5.2.1	Choice of the radius of curvature . . . . .	81
5.2.2	Determination of the coupling length . . . . .	83
5.2.3	Shutter synchronization . . . . .	87
5.2.4	Fabrication of preliminary structures . . . . .	87

5.3 Fabrication and characterisation of the switch . . . . .	90
<b>Conclusions</b>	<b>97</b>
<b>Bibliography</b>	<b>107</b>
<b>Ringraziamenti</b>	<b>109</b>



# List of Figures

1.1	Diagram of a three layer planar waveguide structure and of the first three guiding modes. [1] . . . . .	3
1.2	Diagram of possible modes of the three-layer structure.[1] . . . . .	4
1.3	Optical ray patterns for (a) air radiation modes, (b) substrate radiation modes, (c) guided mode.[1] . . . . .	5
1.4	Power in waveguide 1 (line) and waveguide 2 (dashed) when the two waveguides are identical. A reduction in power exchange can be seen when there is a $\Delta\beta$ between the first (+) and the second (*) waveguide. . . . .	8
1.5	Photoresist masking technique for channel waveguide fabrication.[1]	9
1.6	Comparison between state of the art switching technologies. Logarithmic scale is used for both axes.[2] . . . . .	12
1.7	1x2 switch with flexible double-electrode actuator. Left: neutral position; right: switched state.[3] . . . . .	13
1.8	(a)–(c) Deflection cycle of the electrostatic actuator (top view). (d) Electrical isolation of the electrodes using PECVD. (e) Bulges avoid flat contact between the electrodes[3] . . . . .	14
1.9	(a) Schematic of a microdisk add–drop multiplexer. (b) Calculated transmittance at through and drop ports against gap dimension.[4]	15
1.10	Schematic structure of the microdisk resonator with deformable waveguides. (a) At zero bias. (b) With voltage applied on the electrodes.[4] . . . . .	15
1.11	(a) Schematic diagram of the coupler switch with an electrostatic comb-drive actuator. (b) Normalized light intensities at the through and drop ports of the coupler switch, calculated as a function of the actuator displacement and gap G between the waveguides.[5]	16
1.12	Schematic of a mass bound to a base moving with respect to a reference. . . . .	17
1.13	Frequency response of three damped harmonic oscillators actuated from the base with resonance frequency $10^3$ rad/s, but different damping $\xi$ : 0.01(line), 0.1(dashed), 1(point-dashed). . . . .	18

1.14	(a) Example of beam with deflection $w$ and of one piece of length $dx$ . (b) Schematic representation of the strain $\epsilon$ induced by a rotation $\theta$ of a piece. (c) Representation of the forces acting on a piece: M: bending moment; S: shear force; $F = \mu dx \frac{\partial^2 w}{\partial t^2}$ : inertial force. . . .	19
1.15	Schematic of the cantilever structure. The waveguide (WG) in the cantilever is aligned with the one in the bulk but separated by a gap spacing as shown in A. During oscillation the two waveguide misalign with each other.[6] . . . . .	23
2.1	Absorption processes:(a) multiphoton ionization, (b) tunneling ionization and (c) avalanche ionization (free carrier absorption followed by impact ionization). VB, valence band; CB, conduction band.[7]	29
2.2	Energy density at threshold dependency from pulse duration, where $\eta$ is a fixed ionization probability. The model considers an illustrative material with electron recombination and diffusion time of respectively 1 fs and 500 ps.[8] . . . . .	31
2.3	Threshold pulse energies for different regimes in a fused silica sample. Squares represent the thresholds for smooth refractive index (regime 1), circles for birefringent structures and nanogratings (regime 2) and triangles for void formation (regime 3).[9] . . . . .	32
2.4	Finite-difference model of glass temperature versus pulse number, at a radial position of $2 \mu\text{m}$ from the center of the laser beam. The difference in heat accumulation is showed for three repetition rate.[10]	33
2.5	(a) Longitudinal and (b) transverse writing geometry.[11] . . . . .	34
2.6	Polarization-dependent nanostructure in the transverse writing geometry. The linear polarization $E$ is (a) perpendicular and (b) parallel to the scan direction $S$ . The case of circular polarization is shown in (c).[12] . . . . .	35
2.7	(a) Picture of the 3D microchannel based device.[13] (b) Side view of the internal thread fabricated in glass.[14] . . . . .	36
2.8	(a) Scheme of the irradiation pattern for the ablation and removal of a box structure. (b) Picture of a depleted box.[6] . . . . .	37
2.9	Optical microscope image of a typical tapered microchannel.[15] .	37
2.10	Schematic of the two detection methods. (a) Transmission measurement with He-Ne laser. (b) Fluorescence measurement with Ar laser.[16] . . . . .	38
2.11	(a) Schematic of the procedure for sidewall metal patterning in 3D glass microfluidic structures. (b) Photograph of the on-chip sidewall electrode taken at an angle of $45^\circ$ . The inset shows a close-up of the electrode.[17] . . . . .	39
2.12	Observation of a <i>C. elegans</i> worm changing its direction in the microchannel when the polarity of an electric field (3.5 V/cm) was switched at 7.5 s.[17] . . . . .	39

2.13	Schematic of the motion sensor.[18] . . . . .	40
2.14	(a) ILE (top) and stationary waveguide (bottom). (b) Output behaviour measured and simulated. (c) Particular of the double-compound flexure when moved (top) and in relaxed position (bottom).[18]	41
3.1	Schematic of the fabrication setup. BE1,2: beam expanders; $\lambda/2$ : half-waveplate; Pol: polarizer; SH: Shutter; PM: power-meter; OBJ: objective; V,H-TS:vertical and horizontal translation stages. . . . .	43
3.2	Schematic of the femtosecond laser source as presented by the producer.[19] . . . . .	44
3.3	Pictures of the translation stages together with the final elements of the fabrication setup (a) and the sample mounting (b). A: sample holder; B: two-axis gimbal. . . . .	46
3.4	Schematic of the setup for oscillation analysis. The bubble presents the detail of the front view of the support. . . . .	47
3.5	Microscope image of a waveguide facet. . . . .	48
3.6	Schematic of the optical setup for the characterization of the transmission. . . . .	49
3.7	Schematized directional coupler. $L_c$ : interaction length; $D_c$ : interaction distance. . . . .	50
3.8	Schematic of the setup for characterizing the coupling between waveguides. . . . .	51
3.9	Pictures of the pigtail setup. (a) Instrumentation (b) Zoom over the sample area after the glue has solidified. . . . .	53
4.1	Schematized structure of the device with an oscillating cantilever into a cavity and two aligned waveguides (red lines). . . . .	55
4.2	Largest oscillation (9 %) observable on the first device. The 23.7 kHz signal, with maximum 1.55 V and peak-to-peak 144 mV, is in yellow while the actuation voltage is in blue. . . . .	56
4.3	Simplified scheme of the function generation output. The dashed line represents the load resistance that has been removed. . . . .	58
4.4	Normalized output of the device, measured at the photodetector, when 20 V (a) and 40 V (b) peak-to-peak are applied onto the piezoelectric actuator. (c) Case of 40 V peak-to-peak applied onto two piezoelectric actuator. . . . .	59
4.5	(a) Representation of an oscillating cantilever and of the waveguides (red lines). (b-d) Simulations of the device output (blue line) and of the displacement of the tip (red dashed line) when: (b) $D = 4 \mu\text{m}$ , $d_{max} = 2 \mu\text{m}$ ; (c) $D = 4 \mu\text{m}$ , $d_{max} = 4 \mu\text{m}$ ; (d) $D = 4 \mu\text{m}$ , $d_{max} = 8 \mu\text{m}$ . . . . .	61

4.6	(a) Representation of the oscillating cantilever and of its waveguide when they are aligned with the output waveguide at rest position. (b) Simulations of the device output when $D = 0 \mu\text{m}$ and $d_{max} = 8 \mu\text{m}$ . . . . .	61
4.7	Least square fit (red dashed line) of the experimental data (blue line). . . . .	62
4.8	Detail of the cantilever basis. On the top side of the basis, a recess is clearly visible. . . . .	62
4.9	(a) 3D in scale representation of the boxes in which the substrate is divided for the ablation. (1-4) Lateral boxes: $150 \times 150 \times 1010 \mu\text{m}^3$ ; (5-8) Upper boxes: $25 \times 50 \times 1010 \mu\text{m}^3$ ; (9) Front box: $350 \times 300 \times 10 \mu\text{m}^3$ (measures refer to the longest edge of each box). (b) Fabrication direction as seen from above. . . . .	64
4.10	(a) Front view representation of the ablated boxes with the number indicating the new fabrication order of the lateral boxes. (b) Fabrication direction as seen from above. . . . .	64
4.11	Detail of the basis of the cantilever realized with the new method. No recess are present and the corners are sharp as desired. . . . .	65
4.12	Microscope images of the cantilever from top (a) and front (b) with dimensions. (c) Oblique camera photograph of the cantilever. . . . .	66
4.13	Measured frequency response of the custom voltage transformer when a capacitive load of $4.7 \text{ nF}$ was used. . . . .	67
4.14	Least square fit (blue line) of the transfer function derived from the measurements (stars). . . . .	69
4.15	Least square fitting (red dashed line) of the normalized oscillating output from the device (blue line). . . . .	69
4.16	Normalized output of the device, measured at the photodetector, when $18 \text{ V}$ (a), $40 \text{ V}$ (b) and $76 \text{ V}$ (c) peak-to-peak are applied onto the piezoelectric actuator. . . . .	71
4.17	Extinction ratio with respect to input voltage (peak-to-peak) onto the piezo actuator. . . . .	72
4.18	Displacement of the cantilever tip with respect to the peak-to-peak voltage input given to the piezoelectric actuator, as recovered from oscilloscope measurement. . . . .	72
4.19	Regression line (red) of the displacement behaving linearly with the input voltage. . . . .	73
5.1	Schematic of the cantilever (on the left) and of the waveguides (red lines). . . . .	75
5.2	Schematic of the two port output design. The two waveguide at a distance $D$ proceed parallel for the length $L_c$ , then they separate with the s-bending up to the desired spacing. . . . .	79

5.3	Simulation of the output from port one (blue line) and two (red dashed line) when they are separated by $D = 15 \mu\text{m}$ . The cantilever oscillates at 35 kHz with a maximum displacement of 4.5 $\mu\text{m}$ (a), 7.5 $\mu\text{m}$ (b) and 10.5 $\mu\text{m}$ (c). . . . .	81
5.4	Measured bending loss as function of the radius of curvature. . . . .	82
5.5	Schematic of the two bent waveguides (red lines) in the device with the discussed dimensions. . . . .	82
5.6	Splitting ratio measured (dots) and fitted (lines) for the three sets of couplers with interaction distance 13 $\mu\text{m}$ (o), 15 $\mu\text{m}$ (*) and 17 $\mu\text{m}$ (x). . . . .	83
5.7	Schematic representation of the complete coupler and of its half (structure used in the device). The two different coupling lengths and the contribution of the bent parts to the total phase in both cases are indicated. . . . .	84
5.8	Splitting ratios measured from the 14 couplers when the coupling distance was 13 $\mu\text{m}$ (a) and 15 $\mu\text{m}$ (b). The least square fit is also shown in the graphs. . . . .	85
5.9	Measured distances of the initial (blue stars) and final (red cross) point of each waveguide from the corresponding point of the reference one (0.1 mm/s) due to the opening and closing time of the shutter. The regression line is also shown for the initial (blu dashed line) and final (red pointed line) distances. . . . .	88
5.10	Schematic of Structure 1 (a) and Structure 2 (b) where the red lines are waveguides and the central black rectangle in (b) is the air spacing. . . . .	88
5.11	Microscope image of Structure 1 (left) and tructure 2 (right) at the interface between the waveguides when the separation between the output waveguides is $D = 15 \mu\text{m}$ . . . . .	89
5.12	Measurements of the output from waveguide 1 (blue line) and 2 (red dashed line) of the $D = 13 \mu\text{m}$ device when 12 V (a), 30 V (b) and 60 V (c) peak-to-peak are applied onto the piezoelectric actuator. The outputs have been normalized to the maximum voltage measured. . . . .	92
5.13	Measurements of the output from waveguide 1 (blue line) and 2 (red dashed line) of the $D = 15 \mu\text{m}$ device when 16 V (a), 70 V (b) and 120 V (c) peak-to-peak are applied onto the piezoelectric actuator. The outputs have been normalized to the maximum voltage measured. . . . .	95



# List of Tables

2.1	Parameter used in some relevant works on water assisted laser ablation. . . . .	36
5.1	Predicted values of some parameters discussed during the quantitative analysis of the constraints. The PI has been calculated in the case of an oscillation with amplitude $D/2$ . $T_{rest}$ : transmission from a single port at rest position; CT: cross talk; $L_{angle}$ : losses induced by the coupling angle between the cantilever and the output waveguide; PI: port isolation. . . . .	80
5.2	Parameters obtained from the fit of the measured splitting ratios. The standard deviation is retrieved from a linear regression of the total phase term $kL_C + \phi_0$ . . . . .	84
5.3	Parameters obtained from the fit of the measured splitting ratios. The percentage difference with the previous ones is indicated in the parentheses. . . . .	84
5.4	Parameters obtained from the fit of the measured splitting ratios when entering with horizontal polarization . . . . .	86
5.5	Measured losses, considering the sum of the contributions of both outputs. The IL of a reference straight waveguide has been subtracted to retrieve just the contribution of the interface. $L_{model}$ : expected losses from the model; $L_{glass}$ : losses due to the glass interface in Structure 1; $L_{air}$ : losses due to the air interface in Structure 2. . . . .	89
5.6	Relevant quantities measured from the switch at 30 V peak-to-peak actuation. . . . .	93
5.7	Relevant quantities measured from the switch at 70 V peak-to-peak actuation. . . . .	94



# Introduction

Femtosecond laser micromachining has stood out, from its birth in the late nineties, as a powerful and versatile technique for integrated device prototyping. This technique is based on femtosecond laser pulses, focalized with a microscope objective, to obtain permanent and localized modifications on many kind of substrates. The nonlinear nature of the interaction between laser pulses and transparent material confines the modified region to the focal point of the irradiation, thus enabling modifications in the bulk of the material without affecting the surface and providing the technique with a great 3D capability. By controlling the irradiation conditions, several kinds of material alteration can be obtained, such as refractive index modifications, phase changes, structural modification and void formation. Moreover, the reduced cost and dimensions of the equipment and the rapidity of the fabrication process are ideal features for device prototyping.

Complex integrated waveguides circuits have been realized in a wide field of applications, ranging from astrophotonics to the experimental evaluation of quantum models. Waveguide writing by the means of refractive index modification is just one of the possibilities of the technique. The creation of self-organized nanogratings in fused silica stands at the basis of the FLICE technique, with which microchannels can be excavated by selective chemical etching of the irradiated region. This paved the way to the realization of microfluidic and lab-on-a-chip devices, which stand at the cutting edge of microbiological analysis. Finally, the possibility of removing material by ablation in almost any substrate has enriched even more the portfolio of applications of femtosecond laser material processing.

In several applications, devices able to modulate and route the optical signal, within optical fiber networks or complex integrated-waveguide circuitry, are required. In glass, due to the lack of nonlinearity and conductive properties, this is usually obtained with a phase shifting inside an interferometric structure, which is given by a refractive index variation induced by a local heating. The main limitation of these devices is that in most cases they suffer from a slow response time, due to the thermal diffusion dynamics (in the order of ms).

The aim of this work is to achieve faster modulation and switching of an optical signal exploiting oscillations of mechanical microstructures. In particular, the main idea behind this work is to have a waveguide, embedded into a micro-cantilever beam, perfectly aligned with an output waveguide in front of the structure. The

mechanical oscillation of the micro-cantilever beam should be able to modulate the coupling of light between the two waveguides, by inducing a lateral misalignment. With a similar idea we intend to realize an opto-mechanical switch by using two output waveguides, instead than just one.

In Chapter 1, a summary of the most important aspects of waveguide theory is presented, followed by a brief review of the state of the art of integrated switching technologies, where a particular attention is given to the micro-opto-electro-mechanical systems (MOEMS). Then, some relevant aspects of the theory of mechanical oscillations are presented. The first chapters concludes with the presentation of the micro-opto-mechanical modulator realized in the laboratory of the Physics Departement in the past months, which is the starting point of this thesis work. In Chapter 2, femtosecond laser micromachining is presented, highlighting its microstructuring capabilities and the most important aspects of laser-matter interaction involved in the process. Relevant examples of devices realized by this technique are also given. The equipment used and the methods applied during the fabrication and characterization process are presented in Chapter 3. Chapter 4 concerns the analysis and the development of the optical modulator, with the experimental process followed to optimize such device. This optimized device is then used as a starting point for designing a micro-opto-mechanical switch. In Chapter 5, the design of the new device is presented, together with the choice of the parameters used to obtain a complete device.

# Chapter 1

## Integrated-optics modulators and switches

### 1.1 Waveguide optics

Waveguides are the basic element of integrated optical devices. They are structures presenting a higher refractive index with respect to the bulk and therefore able, thanks to the phenomenon of Total Internal Reflection, to guide optical modes. Analytical mode distributions cannot be derived in most of the cases, thus numerical or approximated methods are typically employed in real-world cases. However, analytical approaches can be useful to understand the basic physics of the devices.

#### 1.1.1 Waveguide theory

We consider for simplicity a three-layer structure such as the one in Figure 1.1 which has three refractive indices  $n_2 > n_3 \geq n_1$  and which is infinite on both y and z axis. Layers 1 and 3 are semi-infinite on x. An optical mode of that structure is defined as a solution of Maxwell's wave equation:

$$\nabla^2 \mathbf{E}(\mathbf{r}, t) - \frac{n^2(\mathbf{r})}{c^2} \frac{\partial^2 \mathbf{E}(\mathbf{r}, t)}{\partial t^2} = 0 \quad (1.1)$$

where  $\mathbf{E}$  is the electric field vector,  $\mathbf{r}$  the position vector,  $n$  the refractive index and  $c$  the speed of light in vacuum.

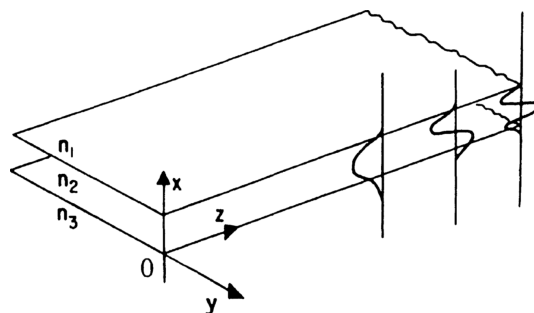


Figure 1.1: Diagram of a three layer planar waveguide structure and of the first three guiding modes. [1]

Assuming a monochromatic plane wave of frequency  $\omega$  propagating along  $z$  direction, the solution can take the form

$$\mathbf{E}(\mathbf{r}, t) = \mathbf{E}(x, y)e^{i(\omega t - \beta z)} \quad (1.2)$$

where  $\beta$  is the propagation constant along  $z$  direction and  $t$  is time.

Substituting the solution into the wave equation, and remembering the infinite extent along  $y$  direction, in each of the three regions we get the *Helmholtz equation*

$$\frac{\partial^2 E(x, y)}{\partial x^2} + (k^2 n_i^2 - \beta^2)E(x, y) = 0 \quad (1.3)$$

where  $k \equiv \omega/c$  and  $i = 1, 2, 3$  indicates the layer.

The solution of the *Helmholtz equation* can take sinusoidal or exponential shape, depending on  $k^2 n_i^2 - \beta^2$ . If  $\beta > kn_i$ , then real roots (eigenvalues) would give an exponential solution, if instead  $\beta < kn_i$ , roots will be imaginary and the solution will be sinusoidal. The solutions and their derivatives must satisfy continuity condition between layers and this leads to limited possibilities, as shown in Figure 1.2:

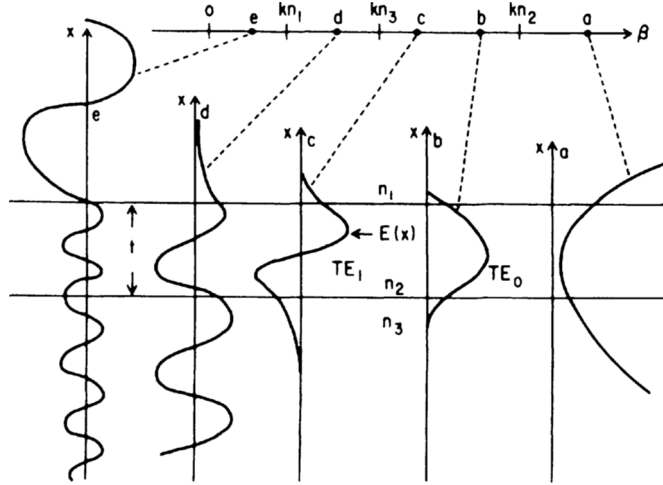


Figure 1.2: Diagram of possible modes of the three-layer structure.[1]

- $\beta > kn_i \forall i$ : the solution are exponential in every layer, getting a diverging field at infinite as shown in (a). This is unphysical, therefore this solution will be neglected.
- $\beta \leq kn_2, \beta > kn_{1,3}$ : This time the structure holds a discrete set of confined sinusoidal modes in the central layer, which exponentially decay in Both outer regions, as in (b) and (c). The second layer in this case is called *waveguide*.

- $\beta \leq kn_{2,3}$ ,  $\beta > kn_1$ : This is the so-called *Substrate radiation* mode, which is a mode propagating both in the second and third layer, as shown in (d). Thus, this mode cannot be sustained by the waveguide and it continuously transfers energy to the third layer.
- $\beta \leq kn_i \forall i$ : The one showed in (f) is called *Radiative mode*. It is not guided since energy can spread through all the space.

An intuitive way to understand this behaviour is to use ray-optics, Snell's and Fresnel laws. If we consider for example a *Transverse Electric*, i.e. with electric field normal to the propagation direction, plane wave propagating at an angle  $\phi$  with respect to the x axis, we can relate it to the propagation constant along z as  $\beta = kn_i \sin \phi$ . When an interface between two media is encountered, the Snell's law applies. If light is propagating from a layer with a higher refractive index  $n_2$  to one with a lower index  $n_{1,3}$ , Total Internal Reflection can occur if the angle is bigger than a critical angle  $\phi_c = \arcsin n_{1,3}/n_2$ . Three possible situations are presented in Figure 1.3. Only waves with  $\phi > \phi_c$  can be guided. Moreover, since the wavefronts of the multiple reflections can interfere, only those which interfere constructively can be guided, forming a discrete spectrum of modes. The number of modes that can be guided depends on the thickness of the guiding layer and on the refractive indexes. It is possible to have waveguides guiding just one optical mode, in that case they are called *single mode* waveguides.

The guided and radiative modes form a complete and orto-normal set, therefore power cannot be exchanged between them.

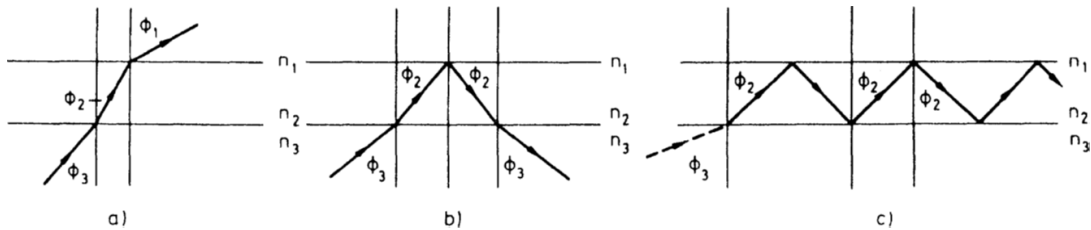


Figure 1.3: Optical ray patterns for (a) air radiation modes, (b) substrate radiation modes, (c) guided mode.[1]

The one discussed is generally called *planar waveguide* due to the 3 layer structure along one axis. Refractive index contrast can occur onto different axis, giving rise to three dimensional structures that can be understood by generalizing the above reasoning, but whose analytical solution is often complicated. A common example is the *channel waveguide*, presenting a rectangular cross section due to index contrast along x and y axis.

### 1.1.2 Losses in real devices

Theory predicts the guided mode to propagate completely unaltered throughout the waveguide, but experimentally no such behaviour is seen, due to different sources of loss that contribute in reducing the total power transmitted by a device. The usual term to address the overall signal reduction for a waveguide of a given length connecting an input port to an output port is *Insertion Loss* (IL), given by  $IL = 10 \log(P_{in}/P_{out})$ , being  $P_{in}$  the input power and  $P_{out}$  the output one. Insertion loss sum up different contributions:

$$IL = PL \cdot l + BL \cdot l_b + FL + CL \quad (1.4)$$

where  $l$  is the overall length,  $l_b$  is the length of a bent part and the other are terms that will be explained in the following:

- *Propagation loss* (PL): With this we refer to the losses the signal experience while propagating through the waveguide, usually due to impurities in the material that can give rise to scattering (voids, contaminant atoms, lattice defects, waveguide surfaces<sup>1</sup>) or absorption (interband transition, free carrier absorption)[1], but also due to the scattering of the waveguide surface[22]. This is a crucial term for large devices, since it multiplies with the length. It is usually expressed in dB/cm
- *Bending loss* (BL): This is a particular kind of propagation loss that the waveguide experience when it is bent. This is due to the waveguide irregularity that can cause mode conversion to a higher mode that is closer to cutoff, making it coupling light to the substrate radiation mode. *Bending Losses* are exponentially dependent on the radius of curvature and are expressed in dB/cm for a fixed radius
- *Fresnel loss* (FL): Back reflection is an inevitable source of loss when light crosses two materials with different refractive indices such as air and glass. It is expressed in dB and can be calculated using the Fresnel's law:

$$FL = -10 \log \left\{ 1 - \frac{(n_2 - n_1)^2}{(n_2 + n_1)^2} \right\} \quad (1.6)$$

where  $n_i$  indicates the refractive index of the two media.

---

<sup>1</sup>The waveguide surface induces a scattering contribution due to its roughness. This could be taken into account with the Rayleigh Criterion[1, 20]:

$$L_{rough} = -10 \log \left\{ \exp \left[ - \left( \frac{4\pi\sigma \cos \theta_i}{\lambda} \right)^2 \right] \right\} \quad (1.5)$$

where  $\sigma$  is the Root-Mean-Square (RMS) roughness of the surface,  $\theta_i$  is the incident angle and  $\lambda$  is the wavelength. The same term could also be used for evaluating the losses due to scattering at an interface[21]

- *Coupling loss* (CL): Coupling loss is a term, expressed in dB, that evaluates the mismatch between the field profile at the input stage ( $E_i(x, y)$ ) and the field profile of the guided mode ( $E_{wg}(x, y)$ ). The estimation of such mismatch can be done by the overlap integral of the two field distribution:

$$O = \frac{|\iint E_{wg}(x, y)E_i(x, y)dx dy|^2}{\iint |E_{wg}|^2 dx dy \iint |E_i|^2 dx dy}. \quad (1.7)$$

The coupling loss is then  $CL = -10 \log O$ . Since this term depends also on lateral misalignment, angular misalignment and field distribution dimension, it can be useful to model the light propagation with a Gaussian function to easily evaluate each contribution[20]. Lateral misalignment will be extensively discussed also in section 1.4.1.

### 1.1.3 Coupled-mode theory

As presented for the planar case in Section 1.1.1, the guided modes are exponentially decaying outside the waveguide. Therefore, the presence of a second waveguide in those decaying region could perturb the single waveguide mode distribution and cause optical power to leak from one waveguide to the other.

Actually, two close waveguides should be treated as a single structure presenting two orthogonal, symmetric and antisymmetric, two-waveguide modes propagating with their own phase velocity and therefore preserving their initial power. However, a simpler and more intuitive treatment can be the one presented by Yariv[23], considering two non-orthogonal one-waveguide modes coupled by perturbative terms that can exchange power.

The electric field propagating in a waveguide can be written as  $E(x, y, z) = A(z)\varepsilon(x, y)$  where  $A(z)$  is a complex amplitude including the phase term  $\exp(-i\beta z)$  and  $\varepsilon(x, y)$  is the field distribution of the mode, normalized so that  $P(z) = A(z)A^*(z)$ . The coupled mode equations describing the variation of the amplitude in each waveguide mode can be written as:

$$\begin{cases} \frac{dA_1(z)}{dz} = -i\beta_1 A_1(z) + k_{12}A_2(z) \\ \frac{dA_2(z)}{dz} = k_{21}A_1(z) - i\beta_2 A_2(z) \end{cases} \quad (1.8)$$

where  $k_{i,j}$  are imaginary terms describing coupling efficiency between waveguides. Assuming identical waveguides, we get  $\beta = \beta_i$  and  $k_{i,j} = -ik$ , where  $k$  is a real term called coupling coefficient that is typically exponentially dependent on the waveguide separation distance.

Solving the case in which light is initially present only in waveguide 1 ( $A_1(0) = 1$ ,  $A_2(0) = 0$ ) we get:

$$\begin{cases} A_1(z) = \cos(kz)e^{-i\beta z} \\ A_2(z) = -i \sin(kz)e^{-i\beta z}. \end{cases} \quad (1.9)$$

Therefore, the power in each waveguide is

$$\begin{cases} P_1(z) = \cos^2(kz) \\ P_2(z) = \sin^2(kz). \end{cases} \quad (1.10)$$

Power is exchanged periodically between the two modes so that at a length of  $L = \frac{\pi}{2k} + \frac{m\pi}{k}$  all the power in waveguide 1 is transferred to waveguide 2.

This is not the case when the two waveguides have a difference  $\Delta\beta$  in propagation constant, since there is a maximum power that can be exchanged. The solution of Equation 1.8, with initial condition  $A_1(0) = 1$ ,  $A_2(0) = 0$ , gives indeed  $P_1(z) = \frac{k^2}{g^2} \sin^2(gz)$  where  $g^2 = k^2 + (\frac{\Delta\beta}{2})^2$  as shown in Figure 1.4.

In a compact device, a typical way to tune the amount of power exchanged is by controlling either the interaction length  $L$  or the distance between the waveguides, i.e. interaction distance, which exponentially influences the coupling coefficient  $k$ .

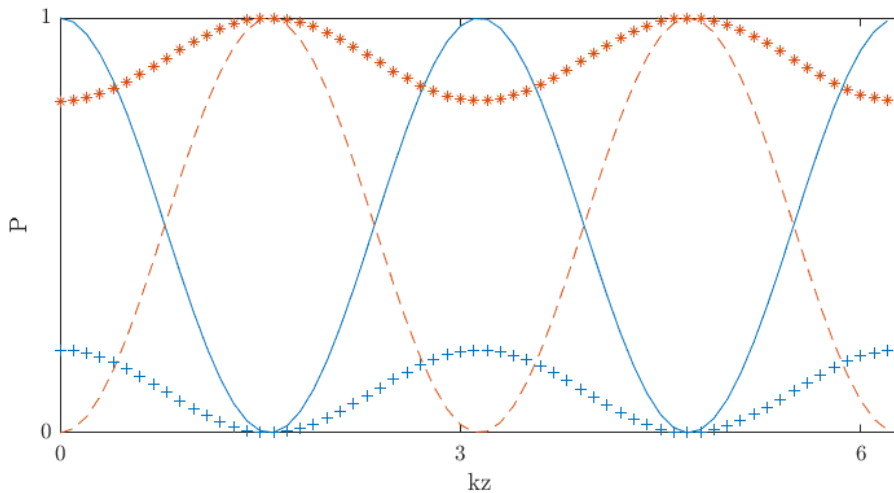


Figure 1.4: Power in waveguide 1 (line) and waveguide 2 (dashed) when the two waveguides are identical. A reduction in power exchange can be seen when there is a  $\Delta\beta$  between the first (+) and the second (\*) waveguide.

#### 1.1.4 Fabrication technologies

Optical waveguides can be fabricated using several different technologies, the choice of which depends on the application, the required performances, the material used and of course the available facilities.

Photolithographic processes are usually exploited, in particular for commercial applications and, in order to produce channel waveguides, distinct fabrication steps are needed to define the index contrast between different regions and to shape the waveguide itself.

One way to make the index contrast, particularly efficient with amorphous material, is to use thin film deposition. The film can be obtained by sputtering a purified solid material on a clean substrate pattern, or from a solution that dries into a dielectric film after a spinner has spread evenly the liquid on the substrate, or by using RF-discharge polymerization of an organic chemical monomer.

Another method, more effective with crystalline material, makes use of substitutional dopant atoms. Here the refractive index modification is obtained by inserting ions into the substrate lattice by diffusion from a source of dopants; to accelerate the diffusion, the sample is placed into a furnace at 700-1000°C. Ions exchange and migration can also be obtained applying an electric field between the source and the substrate, so that the ions are pushed beneath the surface, forming the waveguide. Ions can also be implanted impinging on the atom, once accelerated in vacuum.

Carrier-concentration-reduction is instead a technique used for semiconductors, exploiting the fact that free carriers reduce the refractive index, and thus, by reducing this concentration, one can create a region with higher refractive index contrast. This process is carried out via proton bombardment followed by thermal annealing.

A versatile method to fabricate waveguides in semiconductors is also epitaxial growth. Such technique allows to control both the index of refraction and the transparency window of the waveguide.

To get a channel waveguide, a typical rectangular shape must be given. To do this, depending on the method employed to define the index contrast, two main procedures are used. One is shown in Figure 1.5: a photoresist is deposited onto the film (planar waveguide) that was made using one of the already presented methods. The photoresist is then partially removed by UV-light or x-ray irradiation, after a contact printing mask has delimited the waveguide shape. Then, wet-etching or ion-beam-sputter etching are used to remove the part of the guiding film not masked by the photoresist, obtaining the desired channel waveguide. Another way is instead to put a mask, made of an oxide material able to resist to high temperature (such as  $SiO_2$  or  $Al_2O_3$ ), directly onto the substrate. Then, one of the previously mentioned method can be used to bury a waveguide on the non-masked part of the substrate.

A completely different fabrication method to fabricate waveguides that makes use just of focused ultrashort laser pulses will be discussed in Chapter 2, that is indeed the method adopted to fabricate waveguides in this thesis work.

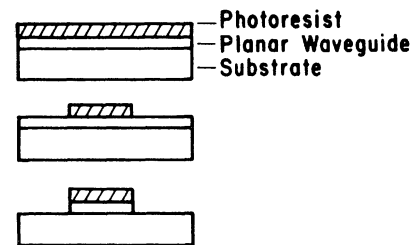


Figure 1.5: Photoresist masking technique for channel waveguide fabrication.[1]

## 1.2 Integrated modulators and switches: state of the art

Modern communication network, as well as integrated technologies, has an increasing request for *transparent* switches (optical cross-connectors) and modulators[2]. A switch is a device able to route a signal coming from one or more input ports into two or more output ports, for example a 1x2 or a 2x2. A modulator has just one input and one output, so it is a 1x1 device, and has the aim of altering one of the property of the propagating signal[24].

The request for transparent (or Opto-Opto-Opto) switches, i.e. devices that operate without the electrical conversion of the optical signal, is motivated by the performance they can grant. Indeed transparent switches are independent from the data rate of the protocol used[2], have decreased interconnection delays[25], larger bandwidth, lower power consumption and dissipation, a wavelength switching cost quite independent of the data bit-rate[26] and lower costs[27] with respect to non transparent devices. However, opaque (or Opto-Electro-Opto) switches, i.e. devices requiring conversion of the optical signal into an electrical one, are still the most used to route signal in Metropolitan Area Networks[28].

For what concerns modulation, in short distance network Direct Modulation is still dominant due to its simplicity, its lower hardware cost and its minimum power consumption[29], so transparent intensity modulator can take a leading role in long-haul communication.

It is common to refer to networks exploiting only transparent devices as *all-optical* in a loose sense, since the modulation and the switching are however driven by electrical signals.

### 1.2.1 Relevant figures of merit

To analyze the performance of a modulator or of a switch, several figures of merit can be defined. Switches and modulators actually share most of these parameters, even though it is different the importance given to each of them in the two cases. A list of few important parameters is reported below[1, 2, 30]:

- *Cross talk* (CT): it is the ratio of the output power coming from all undesired inputs and the output power coming from the desired input. For a modulator the equivalent is called *Contrast Ratio* (CR) or *Extinction Ratio* (ER) and represents the residual signal left when it is switched off, but more often its complementary, the *modulation depth*, is used.
- *Switching time* ( $t_{sw}$ ): it is the time needed to switch up an optical path, i.e. from 10 % to 90 % of its power. For a modulator it is common to find the *Modulation Frequency* ( $f_{mod}$ ) as an alternative.

- *Power consumption*: the power needed for the device to operate. In general, there could be a static and a dynamic consumption when a state of output has to be either maintained or switched. For electro-optical devices Voltage is often considered, instead of power.
- *Port isolation* (PI): It is the ratio between the output signal from a port, when the switching is off on that port, and the input signal. It is useful to evaluate the signal leakage. For a modulator it is equivalent to ER and CT, having just one port.

Of course, other parameters could be defined, depending on the application, such as *wavelength range*, *reliability* (the ability of establishing a connection with a low variance in specified parameters), and *cost*. A further very important parameter is IL, which we have already defined.

As mentioned, the attention given to each parameter is different for a modulator and a switch, as it is usually weighted more the speed for the first and the losses for the second[24]. Moreover, a particular feature of switches only is the *scalability*, i.e. the possibility to increase the number of ports.

### 1.2.2 Technological overview

The implementation of transparent switches and modulators involves a broad spectrum of technologies. Different technologies also require different materials, with consequences on the device cost, performance an application settings.

We will focus in particular, in Section 1.2.3, on MOEMS-based switches, which are the most relevant for the context of this thesis. For this reason, also in the following we will put our attention on the switches only. Actually, information about modulators can be directly inferred, being equivalent to a 1x1 switch. In particular, a list of the main technologies is reported with some representative performance parameters for each of them. Figure 1.6 presents a comparison of state of the art switch technologies with respect of switching time and scalability. Note that, in the following, reported IL don't include the coupling losses with the external fiber/connections.

- electro-optic: it is by far the fastest technology, reaching switching time of 0.7 ns [31], but it usually suffers from quite high IL ( $> 6.7$  dB for a 16x16[32]). It has a quite good scalability (32x32 in [33]). The design of the devices are often based on Mach Zender Interferometers or Microring resonators in which a refractive index change is induced by nonlinear effect due to the electric field such as Pockels or Kerr effect[2]. Other techniques, not rigorously defined as electro-optic, can be used, such as free carrier injection, to alter the refractive index. Design exploiting electro-absorption, such as the Franz-Keldysh effect or the quantum confined Stark effect, are also employed[24].

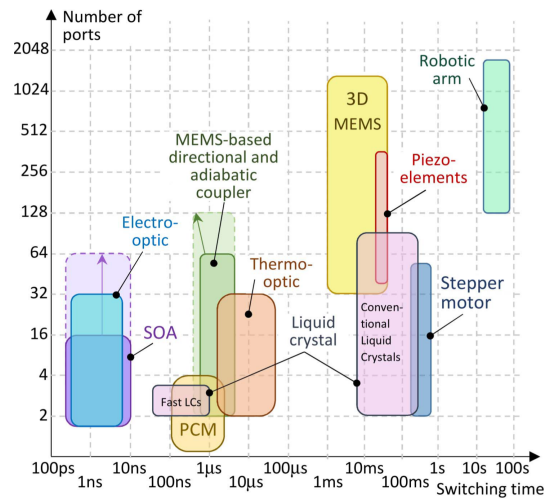


Figure 1.6: Comparison between state of the art switching technologies. Logarithmic scale is used for both axes.[2]

- thermo-optic: here the refractive index variation is induced by thermo-optic effect in structures similar to the ones used with the electro-optic effect. This leads to slower devices (2-30  $\mu\text{s}$ [2][31][34]) with slightly better IL (5.2 dB in a 16x16[34]) and comparable scalability.
- liquid crystals: the switch action here is given by the change in orientation of dipolar molecules of a nematic liquid crystal, by applying an external electrical field. Even though Liquid Crystal on Silicon (LCoS) is used in some commercial devices, it is not very fast, reaching 500 ms of switching time[35]. Combining the Kerr effect to isotropic liquid crystals has demonstrated to bring the switching time to less than one microseconds[36, 37]. Here the routing is not due to reorientation of the crystals, but on a refractive index change. Losses in these devices may be lower than 3 dB[37].
- semiconductor optical amplification (SOA): some semiconductors absorbing at the wavelength of the signal can also act as active material if properly pumped. This can be exploited to make SOA shutters. The switching mechanism here is based on couplers/splitters with a SOA shutter in each branch that acts as an ON/OFF gate, amplifying or absorbing the signal. SOA shutters, to implement in the coupling/splitting structure, are commercially available[38]. This is another very promising technique, since it can bring to switching time of few ns, it is scalable up to 64x64 ports[39] and has no losses (it is indeed an active material, so all the losses are compensated by a gain)[40].
- opto-mechanical: in these devices, mechanical structures and moving parts are used to precisely align waveguides or fibers, to deviate light paths with

mirrors, to alter properties in resonating or light-coupling structures or to alter collimation of light beams [2]. To do so, moving regions with diverse size may be employed: from commercial robotic arms[41], stepper motors[42] and piezoelectric[43], to micrometric MEMS devices[44]. Almost all opto-mechanical devices are characterized by low IL, good cross talk and very high scalability (for example 384x384 in [43]). Large-scale opto-mechanical devices, typically suffer from long switching times (even in the order of seconds[41]). Integrated MEMS can on the other hand reach the microsecond scale[44].

### 1.2.3 MOEMS switches

MOEMS switches can be divided into two main categories: free-space and waveguide devices. Free-space devices make use of micromirrors and microlenses to deviate and focus an input beam onto the desired output. The mirrors are usually moved by actuators or by electrostatic force. The light path has to be precisely engineered in order not to induce losses due to misalignment, mode mismatch and scattering from surfaces (as for the mirror). Waveguide devices on the other hand don't need any internal microlens or micromirror for shaping the optical path and can typically guarantee lower losses and compact size[45]. The switch is generally controlled by an actuator that either moves a fiber/waveguide or change the properties of coupling structures. We discuss a few examples here below.

**Moving fiber/waveguide** A way to deviate light is to directly move a waveguide or a fiber so that it couples to the right port. The design of such device is based on a cantilever beam in which the waveguide is integrated[46] or with the fiber bound onto it[3, 45, 47]. The actuation methods can be based on electrostatic comb actuators[45, 46], thermal actuators (based on bimetal effect or thermal expansion)[47] or individual electrostatic actuators[3]. As an example, the design based on the individual electrostatic actuators will be presented.

As shown in Figure 1.7 a fiber is mounted on a cantilever with two separate electrodes fixed on both sides. Two similar electrodes are placed on the fixed part of the structure, opposite to the ones on the cantilever. At the end of the fiber, two fixed output fibers are paired below a reversed V-groove that is needed in order to keep the alignment. As can be seen in Figure 1.8, When a voltage is applied

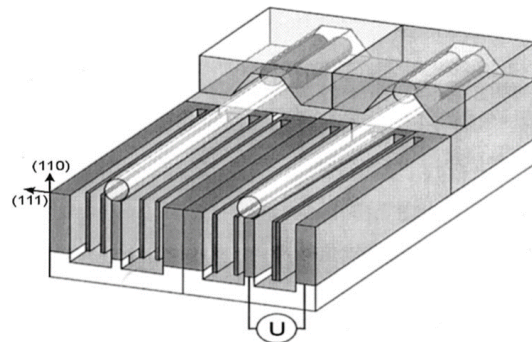


Figure 1.7: 1x2 switch with flexible double-electrode actuator. Left: neutral position; right: switched state.[3]

to the electrodes, at first their free ends bend, due to electrostatic attraction, and then the rest of the electrode mounted on the cantilever, which is free to move, is pulled towards the fixed one. This bends the cantilever (and so the fiber) in an S-shape towards the output, preventing losses due to angular misalignment. Moreover the fabrication method (Plasma Enhanced Chemical Vapor Deposition-PECVD), by avoiding flat contacts, prevents the electrodes from stick together after the voltage is switched off. Note that in this device, continuous power is needed to keep a given output state, because the rest position of the cantilever is between the two output.

Concerning the fabrication method, the mechanical structure is made by etching silicon with KOH after a silicon nitride mask is transferred. Then the electrical insulation is made by PECVD, which prevents the sticking of the electrodes, and the contact pads are coated with an Aluminum layer. The silicon structure is finally bonded on a substrate with UV-curing glue and the output fibers are assembled with the V-groove and aligned. The input fiber is fixed to the cantilever using resin.

This device presents IL lower than 1 dB,  $t_{sw} < 10$  ms and a CT  $< -50$  dB with a 40 V actuation.

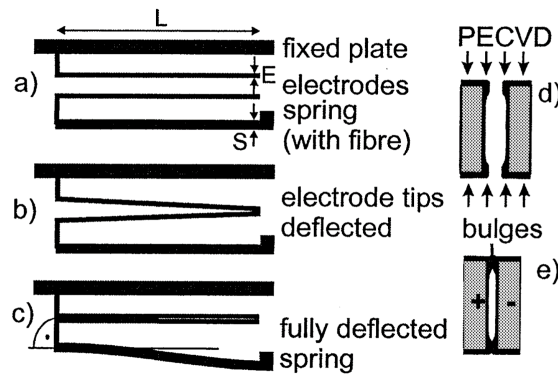


Figure 1.8: (a)–(c) Deflection cycle of the electrostatic actuator (top view). (d) Electrical isolation of the electrodes using PECVD. (e) Bulges avoid flat contact between the electrodes[3]

**Moving microdisk/microring resonators** In this kind of device, two waveguides are separated by a microdisk[4, 48] or a microring[49], which is optically resonating at a fixed wavelength. When light is coupled from one of the waveguide to the resonator, signal of the chosen wavelength can cross to the other waveguide. The switch is done by spoiling the quality factor attaching a lossy material to the resonator[49], or by changing the distance between the waveguides and the resonator[4, 48]. In these devices, driving power is only needed when light is sent to one of the two outputs, since the rest position of the structure is when light is

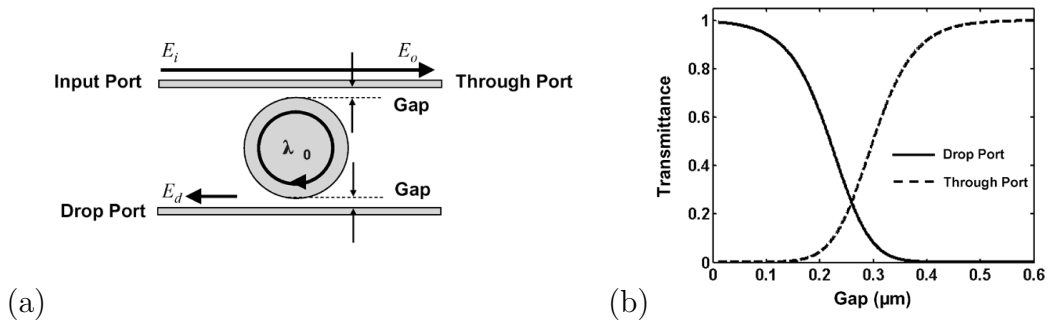


Figure 1.9: (a) Schematic of a microdisk add-drop multiplexer. (b) Calculated transmittance at through and drop ports against gap dimension.[4]

sent to the other output. We will now present some detail of the device proposed in [4].

As can be seen in Figure 1.9 the two waveguides are separated by a gap from the microdisk and, since the coupling depends exponentially from the coupling distance, almost no light couples to it. When the gap is reduced, the coupling increases and the resonant wavelength is progressively coupled to the drop port. In this device, a reduction of  $1 \mu\text{m}$  can change the coupling coefficient by five orders of magnitude, due to Si high refractive index, of which the device is made. To achieve this gap reduction, four electrostatic gap-closing actuators are used as in Figure 1.10.

The device is fabricated in a Silicon-on-Insulator platform by a single etching step after lithographic patterning.

The device is able to reach an ER on the through port of 9 dB with 61 V applied.

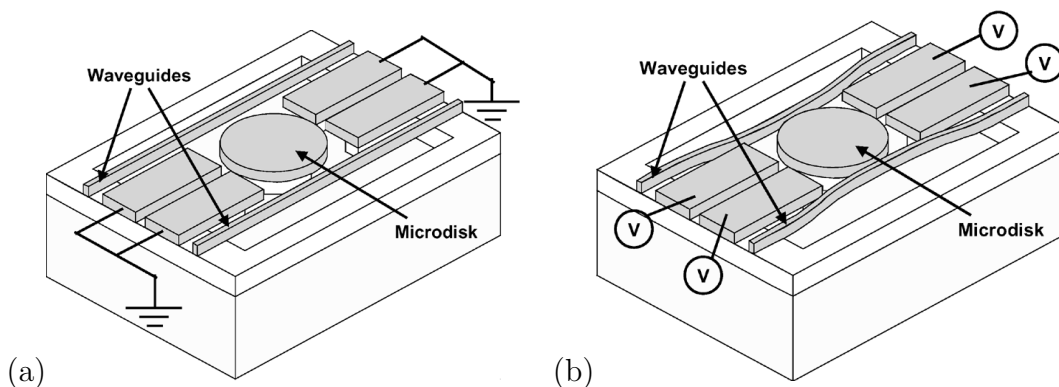


Figure 1.10: Schematic structure of the microdisk resonator with deformable waveguides. (a) At zero bias. (b) With voltage applied on the electrodes.[4]

**Moving directional coupler** Another way to implement an integrated switch is to use a directional coupler whose coupling coefficient  $k$  can be changed. A common way is to use thermo-optic[50] and electro-optic effects[51], but in MEMS devices  $k$  is controlled by moving one of the two waveguides closer to the other with an electrostatic actuator, exploiting the exponential dependence of  $k$  from the interaction distance[5, 52]. In particular the design of [5] will be presented here.

A symmetric directional coupler made of two suspended waveguides is designed with the interaction length required to keep the output at the through port. The motion of one of the waveguide is controlled by a comb actuator able to reduce the gap to the switch point as in Figure 1.11. The interaction length is fixed, therefore, reducing the coupling coefficient, the balance between the two output oscillates as in Figure 1.11.

With this design they were able to reach  $CT < -6.9$ ,  $PI > 6.2$ ,  $IL \sim 1$  dB and  $t_{sw} \sim 50 \mu s$ .

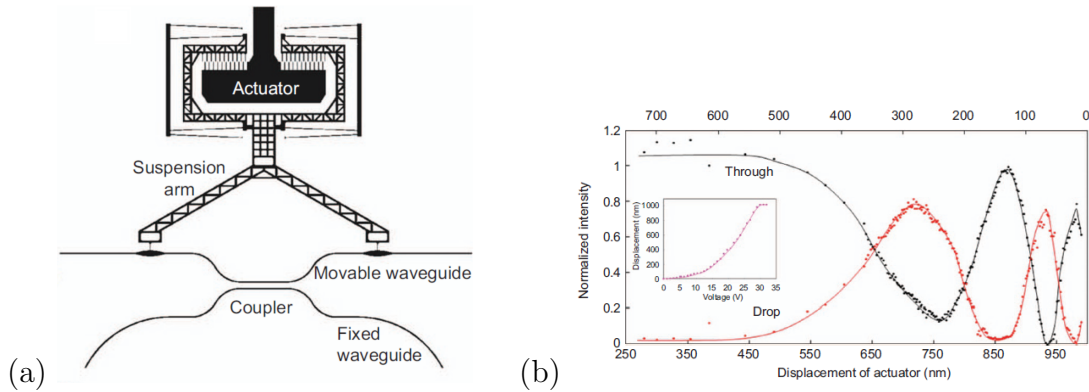


Figure 1.11: (a) Schematic diagram of the coupler switch with an electrostatic comb-drive actuator. (b) Normalized light intensities at the through and drop ports of the coupler switch, calculated as a function of the actuator displacement and gap  $G$  between the waveguides.[5]

## 1.3 Oscillating cantilever

### 1.3.1 The harmonic oscillator

Considering the structure schematized in Figure 1.12, we want to write the equation describing the relative motion  $x(t)$  of the mass  $m$  with respect to its base. When  $x(t) = 0$ , the mass is at the same position of its base. The mass is elastically connected to that base by a spring with stiffness  $k$ , which introduces a dragging force according to *Hooke's Law*:  $F_{drag} = -kx$ . The damping due to viscous friction is taken into account via a term proportional to the velocity  $-r\dot{x}$ . The mass is forced to oscillate through the absolute motion  $y(t)$  of the base. This is referred to an external origin, so that, when  $y(t) = 0$ , the base is in that point. The absolute position of the mass is thus  $x(t) + y(t)$ , contributing to the oscillator equation as  $m(x(t) + y(t))$ . This is analogous to consider the motion of the base as an opposing forcing term for the relative motion  $x(t)$ . The 1D harmonic oscillator equation in this case becomes:

$$m\ddot{x} + r\dot{x} + kx = -m\ddot{y}. \quad (1.11)$$

As we will see later, such equation is useful to model the oscillation of a cantilever beam that is actuated from its base, rather than forced from the free extremity. We would like now to obtain the frequency response of such a system. Given a sinusoidal motion of the base  $y = Y e^{-j(\omega t + \psi)}$ , the relative motion of the mass is known to be sinusoidal too,  $x = X e^{-j(\omega t + \phi)}$ . The relation is fully described by a transfer function whose modulus linearly links the amplitudes of the oscillations,  $X = |T(j\omega)|Y$ , while its argument determines the phase by  $\phi = \psi + \arg(T(j\omega))$ . Substituting the sinusoidal motions into the equation and considering that  $T(j\omega) = x(t)/y(t)$ , the transfer function takes the form:

$$T(j\omega) = \frac{m\omega^2}{-m\omega^2 + rj\omega + k} = \frac{\omega^2}{-\omega^2 + 2j\xi\Omega\omega + \Omega^2} \quad (1.12)$$

where  $\xi = r/(2\sqrt{mk})$  is the damping coefficient and  $\Omega = \sqrt{k/m}$  is the resonant angular frequency. The modulus takes the form of:

$$|T(j\omega)| = \frac{\omega^2}{\sqrt{\omega^4 + 2(2\xi^2 - 1)\Omega^2\omega^2 + \Omega^4}}. \quad (1.13)$$

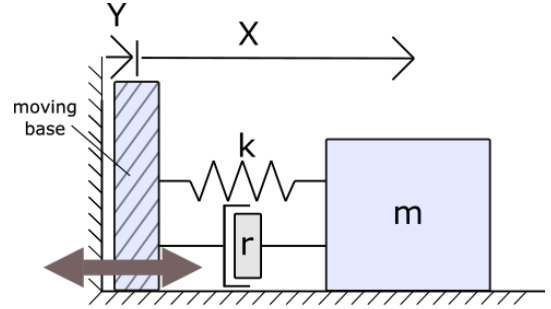


Figure 1.12: Schematic of a mass bound to a base moving with respect to a reference.

The Bode diagram in Figure 1.13 shows the typical response of a damped harmonic oscillator actuated from the base, with a resonant peak whose height increases (up to ideally infinite) when no friction is present. Outside the resonance peak, other two regions can be clearly identified: *rigid* and *suspended* foundation. The rigid foundation ( $\omega \ll \Omega$ ) is a region in which the ratio  $X/Y$  tends to zero, since the motion is slow enough to let the mass move rigidly with the base. In the suspended foundation ( $\omega \gg \Omega$ ) instead, the oscillation is so fast that the mass is unable to follow it. The mass stands still ( $x(t) + y(t) = 0$ ), while the base oscillates, thus the relative distance  $x$  is the exact opposite of the base motion  $y$ . In this case the ratio of the modulus  $X/Y$  tends to 1.

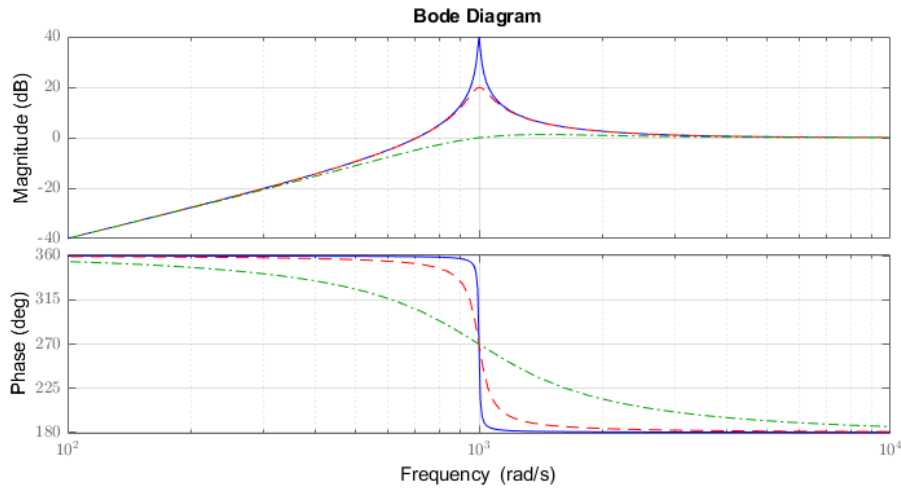


Figure 1.13: Frequency response of three damped harmonic oscillators actuated from the base with resonance frequency  $10^3$  rad/s, but different damping  $\xi$ : 0.01(line), 0.1(dashed), 1(point-dashed).

### 1.3.2 Damping and Q-factor

The structure presented in Section 1.3.1 constitutes a damped resonant system. In the time domain, a resonant system responds to an input pulse by oscillating, but the damping attenuates the oscillation with an exponential envelope. The time constant  $\tau$  of the exponential envelope is related to the damping by  $\tau = 1/\xi\Omega$ , so that when the damping increases, the oscillation attenuates faster.

In resonant systems, another figure of merit is typically used: the *Quality factor*. The quality factor, which is usually referred with  $Q$ , is linearly linked to the time constant and can be defined as  $Q = \tau\Omega/2 = 1/2\xi$ . The quality factor takes higher values when the oscillation is kept with low losses, indeed it can represent the ratio between the energy stored in the resonator and the energy lost per cycle due to the damping process. The quality factor also provide information on how selective

is the resonant peak with respect to the frequencies. Indeed it can be equivalently expressed as the ratio between the resonance frequency and the FWHM of the resonance peak  $Q = \Omega/\Delta\omega$ .

In our scope, the most important aspect of the Q factor is that it linearly links the amplitude of the base motion  $y(t)$  to the mass oscillation  $x(t)$  at resonance condition. In fact, when  $\omega = \Omega$ , the transfer function reduces to  $T(j\Omega) = -j/2\xi = -jQ$ . This leads to the important linear relation for the amplitudes:

$$X = QY. \quad (1.14)$$

Note that the resonant peak is not exactly at the resonant frequency since the maximum of the modulus is obtained at  $\omega_{peak} = \Omega/\sqrt{1+2\xi}$ , but for low damping condition (as it is in our case)  $\omega_{peak} \simeq \Omega$ .

### 1.3.3 Euler-Bernoulli beam theory

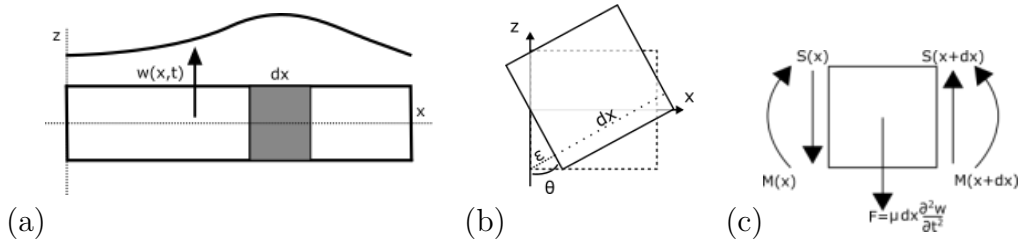


Figure 1.14: (a) Example of beam with deflection  $w$  and of one piece of length  $dx$ . (b) Schematic representation of the strain  $\epsilon$  induced by a rotation  $\theta$  of a piece. (c) Representation of the forces acting on a piece:  $M$ : bending moment;  $S$ : shear force;  $F = \mu dx \frac{\partial^2 w}{\partial t^2}$ : inertial force.

A simplified model that describes the mechanical properties of a beam is the so called Euler-Bernoulli beam theory, which is widely employed in Engineering. We will consider a beam whose  $x$  axis passes through the centroid of its cross-section. The beam deflection is indicated with the function  $w(x, t)$ .

In this model the beam, which is a continuous system, is discretized into an infinite amount of smaller pieces with width  $d_x$ , having their own mass, stiffness and damping (Figure 1.14 (a)). The stress  $\sigma$  is linearly related to the strain (elongation)  $\epsilon$  by the *Elastic modulus* (or *Young's modulus*)  $E$  via the *Hooke's law*:

$$\sigma = E \epsilon. \quad (1.15)$$

In this model the pieces are considered as undeformable, and the beam deformation is given by a rotation of its pieces as in Figure 1.14 (b). Thus, for each point of the cross section, at height  $z$  from the  $x$  axis, we can write the elongation as

$\epsilon = z \partial\theta/\partial x = z \partial^2 w(x, t)/\partial x^2$ , where  $\theta = \partial w(x, t)/\partial x$  is the rotating angle of the piece.

Considering again a single piece of the beam, the bending moment at the coordinate  $x$  is defined as positive when the compressive stress is on the positive  $z$ . It can be written as:

$$M(x) = \iint z \sigma(z) dy dz = EI \frac{\partial^2 w(x, t)}{\partial x^2} \quad (1.16)$$

where  $I$  is the *Second moment of area* (or *area moment of inertia*). This takes into account the distribution of the beam points with respect to its axis and is defined as:

$$I = \iint z^2 dy dz. \quad (1.17)$$

Multiplied together, the elastic modulus and the second moment of inertia give the *flexural rigidity*  $EI$ .

We will now consider the case of a beam that is free to bend along the  $z$  direction. Each piece of the beam, which is subject to multiple forces as in Figure 1.14 (c), should be in dynamic equilibrium condition. If we now impose rotational equilibrium, considering the bending moment  $M(x)$  and the shear forces  $S(x)$  acting on the two opposite faces of the piece, we get:

$$M(x + dx) - M(x) + S(x) \frac{dx}{2} + S(x + dx) \frac{dx}{2} = 0. \quad (1.18)$$

Developing its terms, this reduces to:

$$S(x) = -\frac{\partial M(x)}{\partial x} = -\frac{\partial}{\partial x} \left( EI \frac{\partial^2 w(x, t)}{\partial x^2} \right). \quad (1.19)$$

By imposing now the dynamic equilibrium also for translation and considering the inertial force due to the motion of the beam we can write:

$$S(x + dx) - S(x) - \mu dx \frac{\partial^2 w(x, t)}{\partial t^2} = 0 \quad (1.20)$$

where  $\mu$  is the mass per unit length.

From the two equilibrium condition we finally get the Euler-Bernoulli equation that can be used to describe the vibration of a beam:

$$\frac{\partial^2}{\partial x^2} \left( EI \frac{\partial^2 w(x, t)}{\partial x^2} \right) = -\mu \frac{\partial^2 w(x, t)}{\partial t^2}. \quad (1.21)$$

### 1.3.4 Oscillation of cantilever beam

We want now to solve the equation for the beam deflection  $w$  in the case of a beam with uniform section (the flexural rigidity  $EI$  is constant along  $x$ ).

A common practice is to use separation of variables. For time, a harmonic equation is get, which admits sinusoidal solutions. Therefore, we can consider a harmonic behaviour as

$$w(x, t) = W(x)e^{-i\omega t} \quad (1.22)$$

to solve the Euler-Bernoulli equation. The space dependent equation takes then the form of:

$$EI \frac{d^4 W(x)}{dx^4} - \mu\omega^2 W(x) = 0. \quad (1.23)$$

The solution takes the form:

$$W(x) = A_1 \cosh(\beta x) + A_2 \sinh(\beta x) + A_3 \cos(\beta x) + A_4 \sin(\beta x) \quad (1.24)$$

where  $\beta = \sqrt[4]{\frac{\mu\omega^2}{EI}}$ . Each deflection  $W$  is a *mode* of oscillation, characterized by a *natural frequency*  $\omega$ . The terms  $A_i$  are constants dependent on the boundary conditions.

We will now discuss the case of a cantilever beam of length  $L$ . One end ( $x = 0$ ) of the cantilever beam is fixed and unable to rotate, therefore  $w_n(0) = 0$  and  $\frac{dw_n}{dx}|_0 = 0$ . The free end instead is not affected by momentum and stress, so  $\frac{d^2 w}{dx^2}|_L = 0$  and  $\frac{d^3 w}{dx^3}|_L = 0$ .

With this condition, non-trivial solutions exist only if  $\cosh(\beta L) \cos(\beta L) + 1 = 0$ . Solving numerically, a discrete set of solution  $W_n$  is found in which the first roots  $R = \beta_n L / \pi$  will be:  $R_1 = 0.59686\dots$ ,  $R_2 = 1.49418\dots$ ,  $R_3 = 2.50025\dots$ ,  $R_4 = 3.49999\dots$ .

The natural frequencies can be expressed by the law

$$\omega_n = R_n^2 \left(\frac{\pi}{L}\right)^2 \sqrt{\frac{EI}{\mu}} \quad (1.25)$$

and the corresponding solutions of the space-dependent equation are:

$$W_n = A_1 \left[ (\cosh \beta_n x - \cos \beta_n x) + \frac{\cos \beta_n L + \cosh \beta_n L}{\sin \beta_n L + \sinh \beta_n L} (\sin \beta_n x - \sinh \beta_n x) \right]. \quad (1.26)$$

It is important to notice that the resonant frequencies in this problem are not simply multiples of the fundamental.

The second moment of inertia and the mass per unit length can be written in terms of cantilever thickness  $t$  and density  $\rho$ , so that  $I/\mu = t^2/12\rho$ . The thickness is the dimension of the cantilever parallel to the oscillation (in our case along  $z$ ).

The angular frequencies become:

$$\omega_n = R_n^2 \left(\frac{\pi}{L}\right)^2 \sqrt{\frac{Et^2}{12\rho}}. \quad (1.27)$$

### 1.3.5 Relation between models

In Section 1.3.4 we have recovered the natural frequencies of oscillation, or resonant frequencies, of a cantilever beam. At that frequencies the cantilever acts as the harmonic oscillator of Section 1.3.1, as proven by Sader[53].

To be able to use that model, equivalent stiffness and mass must be defined for each natural frequency, as discussed in [54], so that

$$k_{eq} = \frac{Ebt^3}{4L^3}; \quad m_{eq,n} = \frac{3\rho bL}{(\pi R_n)^4}. \quad (1.28)$$

Each natural frequency of the cantilever can thus be used as the resonance frequency in the harmonic oscillator model:

$$\Omega = \sqrt{\frac{k_{eq}}{m_{eq,n}}} = R_n^2 \left(\frac{\pi}{L}\right)^2 \sqrt{\frac{Et^2}{12\rho}} = \omega_n. \quad (1.29)$$

## 1.4 Cantilever modulators by femtosecond laser pulses: realized prototype

The work of this thesis is based on a device previously realized in Dr. Oselame's laboratories[6]. The device consisted in an oscillating cantilever structure with an embedded waveguide for integrate light modulation. The device was realized by femtosecond laser micromachining, a technique which will be discussed in the next chapter, and in particular Water Assisted Laser Ablation was used for the cantilever structure, while Laser Induced Refractive Index Change was used for waveguides. The structure was made in Eagle XG, a commercial aluminoborosilicate glass. The design and operation of the device will be discussed in the following as a preliminary step for our work.

### 1.4.1 Device design and operation

The device is based on a cantilever which can oscillate horizontally. The cantilever is equipped with a waveguide that is aligned with another in the bulk of the glass, when the cantilever is at its rest position. The idea behind this modulator is to exploit the cantilever oscillation to temporally modulate coupling losses due to lateral misalignment between the waveguide in the cantilever and the waveguide in the bulk. The structure is the one shown in Figure 1.15.

**Lateral misalignment losses** A first order mode, as the one propagating in single mode fibers or waveguides, has no nodes in the lateral distribution. In particular, the intensity profile can be roughly approximated by a Gaussian function,

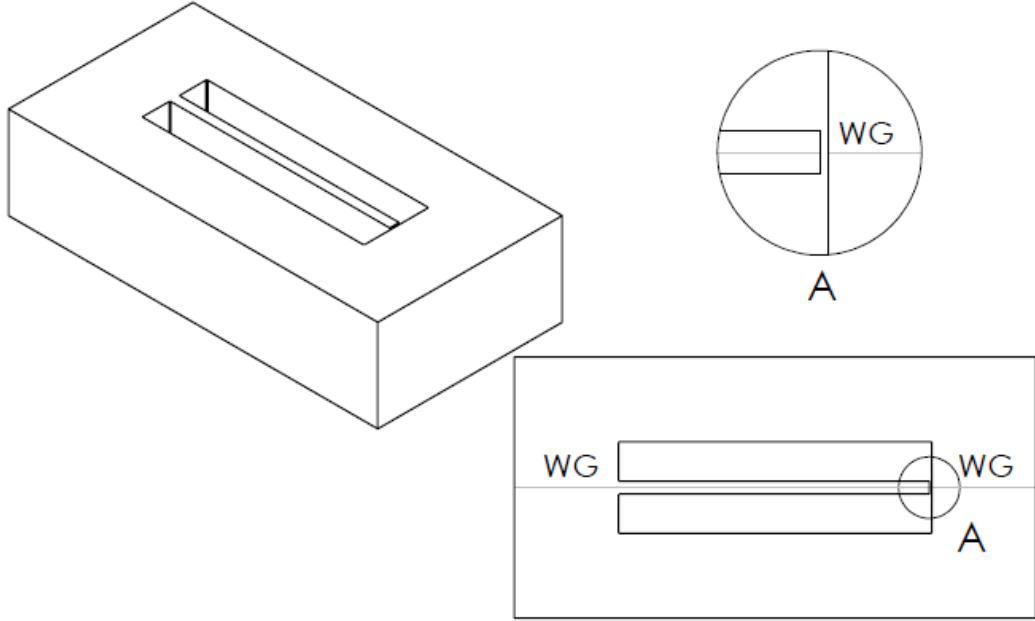


Figure 1.15: Schematic of the cantilever structure. The waveguide (WG) in the cantilever is aligned with the one in the bulk but separated by a gap spacing as shown in A. During oscillation the two waveguide misalign with each other.[6]

as anticipated in Section 1.1.2. The intensity profile can be written as

$$I(x, y) = I_0 e^{-\frac{2x^2}{\sigma_x^2}} e^{-\frac{2y^2}{\sigma_y^2}} \quad (1.30)$$

where  $I_0$  is the intensity maximum and  $\sigma_i$  indicates the dimension of the mode in the  $i$  direction, measured as the distance from the central part at which the intensity decrease up to  $I_0 e^{-2}$ . In this framework, the signal exiting from a waveguide could be described as a gaussian beam with beam waist at the end point of the waveguide. For simplicity we now neglect the beam expansion due to propagation, assuming to be within the Rayleigh range.

To evaluate the effect of a lateral displacement  $\mathbf{d} = d_x \mathbf{u}_x + d_y \mathbf{u}_y$  onto the coupling between light exiting the waveguide of the cantilever and the next waveguide, we should calculate the overlap integral between the field distribution, which, for first order modes, can be expressed in intensity terms as the coupling efficiency

$$\eta(d_x, d_y) = \left| \iint \sqrt{I(x, y)} \sqrt{I(x - d_x, y - d_y)} dx dy \right|^2 \quad (1.31)$$

where  $I$  has been normalized so that  $\iint I dx dy = 1$ . We used the same profile for both the cantilever waveguide and the bulk one since they are identical.

Using Equation 1.30, the two lateral contributions separate into two convolution integrals

$$\eta(d_x, d_y) = \left| \int \sqrt{I(x)} \sqrt{I(x - d_x)} dx \right|^2 \left| \int \sqrt{I(y)} \sqrt{I(y - d_y)} dy \right|^2 \quad (1.32)$$

that, due to properties of Gaussian functions, give another Gaussian function with variance equal to the sum of the variances. Since here the square of the mode dimension plays that role, the new Gaussian has  $\sigma_{conv}^2 = \sigma_1^2 + \sigma_2^2 = 2\sigma^2$  and the coupling efficiency becomes:

$$\eta(d_x, d_y) = e^{-\frac{d_x^2}{\sigma_x^2}} e^{-\frac{d_y^2}{\sigma_y^2}} \quad (1.33)$$

where an efficiency of 1 is assumed at no displacement, as mentioned for normalization. The above efficiency can be a good expression of the *Extinction Ratio*  $ER = -10 \log(\eta(d_x, d_y))$  and will be the base of most of the following studies.

Since, as we will see later, the only oscillation we want to induce is the in-plane one, the coupling efficiency reduces to

$$\eta(d_x) = \frac{I(d_x)}{I_0} = e^{-\frac{d_x^2}{\sigma_x^2}}. \quad (1.34)$$

**Geometry** The choice of the cantilever shape has been a crucial point for this device, since it can directly affect the displacement of the waveguide.

One limitation is given by the dimension of the waveguide mode, since a too thin cantilever could alter the mode distribution inducing losses due to scattering from its surfaces.

Another obvious limitation is given by the resolution limits of the fabrication technique, which are in the order of a micrometer.

From the mechanical point of view, we would like to excite a well-defined oscillation mode of the cantilever (in the plane). Therefore, its thickness and width should be made different, so that oscillations on orthogonal planes resonate at different frequencies. In particular, due to the characteristics of the fabrication technique, a cantilever thinner on the in-plane direction and wider in depth has to be preferred. The lowest-frequency oscillation mode is therefore lying in the plane of the substrate.

The length of the cantilever has been tuned following this reasoning: a shorter cantilever shows an higher resonant frequency, therefore a bigger Q factor, which is appreciated, but on the other hand its stiffness  $k$  increases, inducing an higher stress on the base that could break the cantilever.

**Actuation and behaviour** As explained, the modulation of the light signal is due to the displacement of the two waveguides induced by the oscillation of the cantilever beam. Such oscillation is actuated by a piezoelectric that moves the substrate in a similar way to the one presented in Section 1.3.1, so the substrate oscillation linearly reflects into an oscillation of the cantilever tip amplified by the Q factor. It is important to note that an oscillation at frequency  $f$  of the cantilever results in a modulation of frequency  $2f$  since, during a period of oscillation, the waveguides are aligned two times and not just once.

### 1.4.2 Realized prototype

The realized prototypes were made in Eagle XG, which has a density of  $\rho = 2380 \text{ kg m}^{-3}$  and an elastic modulus  $E = 73.6 \text{ GPa}$ . The thickness of the devices was designed to be  $t = 50 \text{ }\mu\text{m}$  in the in-plane direction while the height was fixed at  $b = 250 \text{ }\mu\text{m}$ . Two lengths were tested,  $L_1 = 1.2 \text{ mm}$  and  $L_2 = 1.5 \text{ mm}$ . Due to fabrication process, the thicknesses turned out to be  $t_1 = 38 \text{ }\mu\text{m}$  and  $t_2 = 41 \text{ }\mu\text{m}$  for the two cantilevers respectively. The resonant frequencies of the first in-plane mode of oscillation were measured to be  $f_1 = 23.8 \text{ kHz}$  and  $f_2 = 16.1 \text{ kHz}$ , in perfect agreement with the predictions from Equation 1.27. The measured Q factors were respectively  $Q_1 = 400$  and  $Q_2 = 520$ .

The waveguide was inscribed in the cantilever at a height of  $150 \text{ }\mu\text{m}$  from the bottom and presented a mode dimension of around  $8 \text{ }\mu\text{m}$ . The coupling efficiency with the fiber was about 70 %, corresponding to a loss of 1.55 dB.

Driving the piezo actuator with a sinusoidal signal with 20 V peak-to-peak amplitude, the device was able to modulate light with an ER of 0.4 dB, corresponding to a modulation depth of 9 %, which is far from a full modulation of the optical signal. Moreover, the modulation peaks were not symmetrically distributed in time.

In this thesis we aim to optimize the described device so to reach a complete and symmetric modulation and to further develop it into a 1x2 switch.



# Chapter 2

## Femtosecond laser micromachining

Femtosecond laser micromachining is a technique for structuring materials at micrometric size, by irradiation with focused ultrafast laser pulses.

The technique was born when Hirao's group, in 1996, showed that a permanent refractive index increase could be induced in the bulk of different transparent glasses by focusing subpicosecond pulses[55]. Before that, femtosecond laser pulses had proven effective for ablation processes[56]. From that time on, the ability of such technique to induce micrometrical refractive index increases, phase changes, structural modifications and void formation has been strongly developed, up to the point of producing devices with high complexity.

In transparent substrates femtosecond laser micromachining exploits the high intensity of focused subpicosecond pulses, to induce material modifications into the bulk without affecting the surface. Due to the nonlinear nature of the process, the modifications are induced just in the focal point of the irradiation, providing the technique with great 3D capability[57]. This is one of the main features of femtosecond laser micromachining, compared to popular microfabrication techniques, such as photolithography, that can process only 2D structures. Moreover, the fabrication setup require way less space and cost, making femtosecon laser micromachining suitable for device prototyping. The nonlinear absorption process can be easily induced in many materials, so the technique shows also a good versatility. Finally, again due to the nonlinearity, feature sizes can reach the submicrometric scale[58].

### 2.1 Laser-matter interaction

A photon of frequency  $\nu$  can provide a transition between two states of a particle only if its energy  $h\nu$ , where  $h$  is the Plank's constant, is equal to the energy difference of those states. Therefore if the photon is hitting a dielectric with energy

gap  $E_g$ , electronic transition may occur between the valence and the conduction band only if  $h\nu \geq E_g$ . In this case, light is said to be linearly absorbed. Material with  $E_g > h\nu$  are therefore *transparent* to irradiation of frequency  $\nu$ .

Actually, high optical intensities can trigger nonlinear processes that make absorption possible also for material transparent at the irradiation frequency. In this kind of processes, two or more photons are absorbed simultaneously in order to achieve an electronic transition. Such nonlinear absorption processes are at the basis of the femtosecond laser micromachining technique.

### 2.1.1 Absorption processes

There are three main absorption processes to induce electron promotion in transparent materials: *multiphoton ionization*, *tunneling ionization* and *avalanche ionization*. Multiphoton ionization and tunneling ionization have the same nonlinear nature and are called *photoionization* process, since they can provide electron promotion to conduction band. The occurrence of either of the two has been modelled by Keldysh and can be predicted by the parameter  $\gamma$ , which assumes value  $\gamma < 1.5$  when tunneling ionization occurs, and  $\gamma > 1.5$  when multiphoton ionization dominates[59]. Avalanche ionization on the other hand requires the presence of *seed electrons* to take place, i.e. some electrons already in the conduction band[60]. These electrons can be provided by the previously mentioned photoionisation processes or by impurities and defects of the material.

We report here a brief description of the three processes which are represented schematically in Figure 2.1.

- Multiphoton ionization: this process involves the simultaneous absorption of multiple photons of frequency  $\nu$ . At low intensities, the probability of absorbing more than one photon at a time is negligible, therefore only linear absorption may occur. However, if the intensity is sufficiently high, the probability for two or more photons to be absorbed simultaneously increase enough to be no longer negligible. If the number  $m$  of photons satisfies the condition  $m h\nu \geq E_g$ , they can be simultaneously absorbed and the electron can bridge the energy gap. The probability of a multiphoton absorption event scales roughly exponentially with  $m$ . Lower-order processes, which involve a lower number of photons with higher frequency, are thus more likely to occur with respect to higher order ones.
- Tunneling ionization: when a strong field is applied to a material, it can alter its band structure, suppressing the Coulomb field that binds a valence electron to its parent atom[60]. If the bending of the conduction and valence bands brings the two to have similar energies, a bound electron in the valence band can undertake a band-to-band transition by tunnel effect (see Figure 2.1). If the irradiation is intense enough, it can provide the field for

the band distortion itself. This process is therefore more common for high intensity irradiation and lower frequencies.

- **Avalanche ionization:** this process can be divided into two steps: *free carrier absorption* and *impact ionization*[60]. During free carrier absorption, seeds electrons, already in the conduction band, can increase their energy by linearly absorbing the irradiated photons. Once the electron has gained enough energy, it can promote a further electron from the valence to the conduction band, by colliding with it. This is the so called impact ionization. Avalanche ionization has been modelled to depend linearly on the intensity of the irradiation due to free carrier absorption[61, 62].

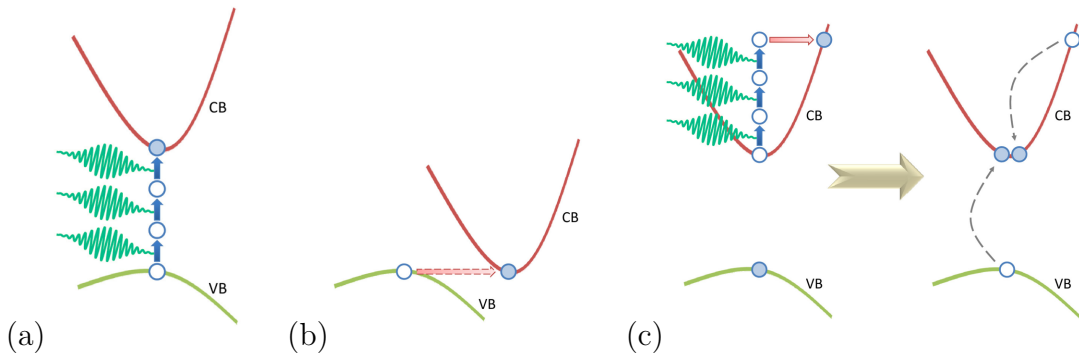


Figure 2.1: Absorption processes:(a) multiphoton ionization, (b) tunneling ionization and (c) avalanche ionization (free carrier absorption followed by impact ionization). VB, valence band; CB, conduction band.[7]

### 2.1.2 Optical breakdown and material modification

When a strong local ionization of the material is reached, due to the absorption process presented above, the dielectric nature of the material is broken and plasma is formed. Material modifications are caused by the relaxation of such a hot electron plasma, that transfers energy to the lattice. In particular, this happens when the plasma reaches the condition of *optical breakdown*. Optical breakdown is a condition in which the plasma oscillates at resonance with the incident irradiation, thus strongly absorbing energy by free carrier absorption.

For longer pulse durations, this condition is met thanks to avalanche ionization[63], while for short pulse durations ( $< 10$  fs in fused silica), multiphoton and tunneling ionization are the main causes of optical breakdown[62, 64].

The process that brings to material modifications can be divided into three steps. First, ionization provides the electrons seed for the plasma. The electron density

$n$  increases in time according to:

$$\frac{dn}{dt} = \alpha I(t)n(t) + \sigma_m I^m \quad (2.1)$$

where  $I$  is the intensity,  $m$  the number of photons,  $\alpha$  and  $\sigma$  are the avalanche and photoionization probability. The plasma frequency depends linearly on the square root of  $n$ ; so, it increases until the electrons in the conduction band reach the so called *critical density of free electrons*, at which the plasma frequency becomes equal to the one of the laser (optical breakdown). At this point, ionization stops and laser power is strongly absorbed by the plasma due to free carrier absorption, thus further increasing the electron energy, heating the plasma. The last step is the energy transfer between the plasma and the lattice that can happen by thermal diffusion or by the emission of a shockwave[62].

Depending on the degree of excitation, plasma relaxation may create cracking, voids or localized melting. The kind of modification depends on the material.

The advantage of using femtosecond laser micromachining is that optical breakdown is obtain with lower energies. Indeed, optical breakdown is a threshold process, being related to the critical density of free electrons. With pulse durations below 1 ps, high intensities are easy to obtain. This enables multiphoton and tunneling ionization to provide seed electrons for the avalanche process. On the contrary, pulses with longer duration (picoseconds scale) cannot exploit nonlinear photionization and therefore rely on linear absorption in material defects, making the optical breakdown process stochastic [58, 62]. The deterministic nature of the process in femtosecond regime enables a more uniform and smooth modification, which is crucial for waveguide writing.

### 2.1.3 Effect of irradiation parameters on the process

Laser-induced modifications are strongly dependent on the irradiation parameters. The main parameters that can be controlled are the wavelength of the irradiation, the pulse duration, the pulse energy, the polarization, the numerical aperture (NA) of the focusing objective, the laser repetition rate and the sample moving velocity and orientation. These parameters must be empirically tailored to obtain the desired modification in terms of quality and typology.

*Wavelength* plays a relevant role in the photoionization process and can, for example in high-band gap materials such as fused silica, determine the quality of a microstructure[65]. Moreover, the intensity threshold for optical breakdown is shown to depend inversely on the square of the wavelength[66]. Indeed, higher laser frequencies require a higher electron density for the plasma to resonate.

We have already mentioned the importance of *pulse duration* in evaluating the deterministic or stochastic nature of the breakdown process. The relation between energy density threshold  $E_{th}$  at a fixed ionization probability  $\eta$  and pulse duration, as modelled in [8], is summarized in Figure 2.2. The model, which considers the

recombination and diffusion time of the electron, predicts well the  $\sqrt{\tau}$  behaviour observed experimentally[67]. For shorter pulse durations, as the ones used in femtosecond laser micromachining, a departure from that behaviour is predicted by the model and observed experimentally[68]. This is due to the insurgence of photoionization as the leading process for the generation of the seed electrons, as mentioned in Section 2.1.2. In general, shorter pulses lead to lower energy threshold, favoring the optical breakdown; however, in the femtosecond regime, the threshold becomes almost constant.

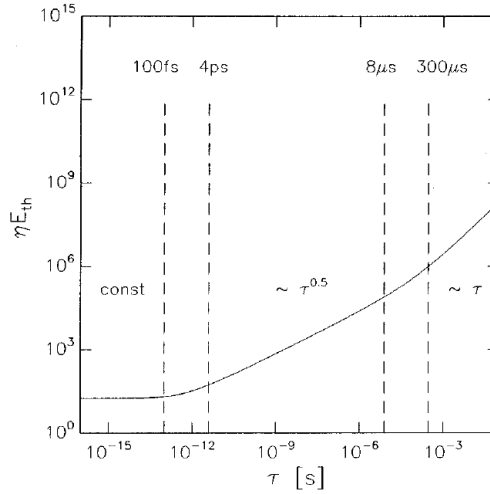


Figure 2.2: Energy density at threshold dependency from pulse duration, where  $\eta$  is a fixed ionization probability. The model considers an illustrative material with electron recombination and diffusion time of respectively 1 fs and 500 ps.[8]

Regarding *pulse energy*, when it is kept near the breakdown threshold, refractive index modification in the order of  $10^{-3}$  are usually obtained[69]. When the energy is far higher than the threshold, the plasma energy increases and so does the Coulomb repulsion between ions, due to reduction of the electronic shielding, causing void formation[57]. With pulse energies inbetween the two, some materials show the formation of birefringent structures and nanogratings, oriented orthogonally to the polarization direction of the irradiating field. The graph in Figure 2.3 represents the regions (in terms of pulse energy and duration) for which the three mentioned regimes of modification occur in the fused silica substrate.

Another important parameter is the  $NA$  of the focusing objective, since it determines the focal volume in which the modification occurs. The focal volume can be estimated by considering the beam waist and the Rayleigh range of the irradiating beam, which are respectively  $w_0 = \frac{M^2\lambda}{\pi NA}$  and  $z_R = \frac{M^2 n \lambda}{\pi NA^2}$  ( $M^2$  is the Gaussian beam propagation factor which has a value of 1 for single mode lasers[70],  $\lambda$  is the wavelength and  $n$  is the refractive index). Due to the different dimensions of beam waist and Rayleigh range, the focal volume takes an elliptical shape, but

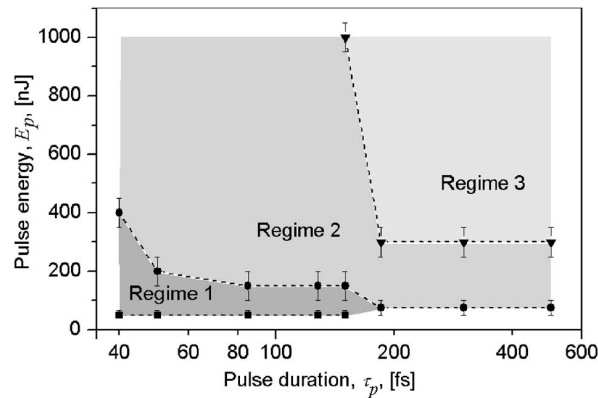


Figure 2.3: Threshold pulse energies for different regimes in a fused silica sample. Squares represent the thresholds for smooth refractive index (regime 1), circles for birefringent structures and nanogratings (regime 2) and triangles for void formation (regime 3).[9]

many techniques have been developed to obtain a circular vertical cross section, useful for waveguide writing[71, 72, 73]. Two processes can alter the focal shape and limit the choice of NA: aberrations and self focusing. Spherical aberrations induced by the focusing objective, relevant for high NA ( $> 0.4$  [60]), becomes negligible if an aspherical lens or a microscope objective are used. On the other hand, the spherical aberration induced by the sample itself, which usually present a plane surface, could alter the focusing volume, making it strongly dependent on the working depth[74, 75]. Self focusing can occur, due to the high peak power of this technique. The electron gas generated by the ionization, on the other hand, act as a negative refractive index change (plasma defocusing), compensating the self focusing effect. This compensation can make the focal volume longer on the direction of propagation. This last effect, which is dominating at low NA ( $< 0.65$  [60]), can be easily reduced by a tight focus.

Finally, the *repetition rate* at which pulses are delivered to the sample influences the induced modification, since it is strictly related to thermal relaxation processes[76]. Low repetition rate, indeed, make thermal relaxation possible between pulses, we speak about *single pulse regime*. As the repetition rate is increased, the absorbed laser power has no time to diffuse before the next pulse arrives, and local temperature builds up as shown in Figure 2.4. In this case we talk about *multiple pulse regime*[10]. This can affect the aspect ratio of the microstructuring and the dimension of the modified area[77]. Related to this, the velocity at which the sample is translated contributes in determining the number of pulses delivered per unit area and per unit time, thus it must be properly adjusted.

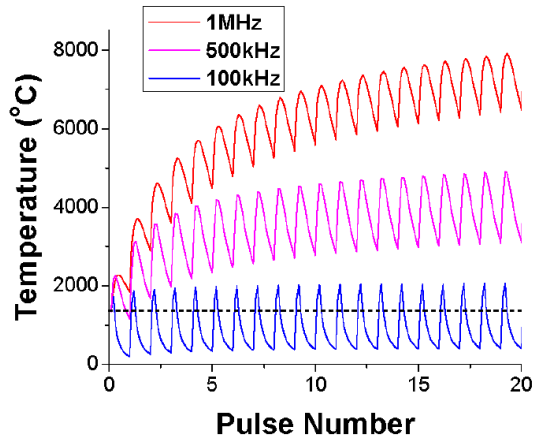


Figure 2.4: Finite-difference model of glass temperature versus pulse number, at a radial position of  $2 \mu\text{m}$  from the center of the laser beam. The difference in heat accumulation is showed for three repetition rate.[10]

## 2.2 Microstructuring capabilities

### 2.2.1 Refractive index modification and waveguide writing

At low energies, just above modification threshold, smooth refractive index variation can be seen in many materials.

The cause of these variation is not yet defined univocally[78], but has been attributed to a densification of the material due to either quenching of melted glass[79] or compression by a shockwave[80]. Also the creation of color centers has been taken into account, as an increase in absorption could lead to a refractive index change in the nearby wavelengths because of the Kramers-Kronig relations.

As described in Section 1.1.1, a refractive index modification can be used to form a waveguide into the bulk of the material, by translating the sample with respect to the laser focus so that the refractive index change induced in the focal volume forms a line. Two main writing geometry can be used, shown in Figure 2.5: transverse and longitudinal. In transverse geometry the sample is moved orthogonally with respect to the irradiation. This leads the waveguide to assume an elliptical cross section following the shape of the focal volume due to the ratio  $z_R/w_0 = n/NA$ ; this may lead to bad mode-matching with optical fibers. Longitudinal geometry on the other hand, moving the sample parallel to the irradiation direction, produces waveguides with circular cross section, because of the transverse symmetry of the Gaussian intensity profile. The main limitation for this geometry is the working distance of the focusing lens.

The writing direction can play a role in the fabrication process, this takes the name of *quill effect* due to the similarity with a writing quill, since the difference

is given by a pulse front tilt of the laser[81].

The capability of femtosecond laser pulses to modify the bulk glass in arbitrary positions, without affecting the surface, has enabled the fabrication of unique photonic devices with 3D geometries[82, 83, 84].

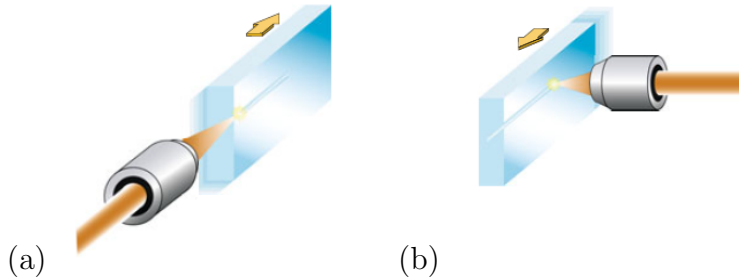


Figure 2.5: (a) Longitudinal and (b) transverse writing geometry.[11]

### 2.2.2 Birefringent structures, nanogratings and FLICE

In some materials, such as fused silica, the generation of birefringent structures has been observed, at energies inbetween the ones used for smooth refractive index modification and those used for void generation.

Such birefringent refractive index changes were firstly observed in the bulk of fused silica glass in [85]. This effect was studied in [86] where they observed the insurgence of periodic structures of nanometric size, the so-called nanogratings. A possible explanation to these features has been found in an interference phenomenon occurring between the electric field of the irradiation and the electron plasma wave, which creates a periodic pattern in the plasma distribution[86]. An alternative explanation has been proposed in [12], which considers the self-ordering of the nanoplanes, induced by inhomogeneous optical breakdown, as the main cause for the nanogratings formation. Both models predict the strong dependence of the nanograting formation on the incident polarization. Indeed, as shown in Figure 2.6, nanogratings are observed experimentally to form along planes perpendicular to the polarization direction of the writing beam.

The irradiated pattern, where the nanogratings are formed, shows an increase in chemical etching rate when the sample is exposed to HF (hydro-fluoric acid) or KOH (potassium hydroxide), with respect to the pristine fused silica. Exploiting this feature, it is possible to irradiate channel-like structures in the sample that are then selectively etched, thus providing a mean to inscribe microchannels into glass samples[87]. The increase in etching rate is linked to the direction of the nanogratings, being maximum when the planes are parallel to the writing direction, favoring the diffusion of the etchant solution[12]. This microstructuring

method, called FLICE (femtosecond laser irradiation followed by chemical etching), has led to the demonstration of many devices based on buried microfluidic channels[12, 88, 89, 90]. One drawback of this technique is that only few materials present the enhanced etching rate[12].

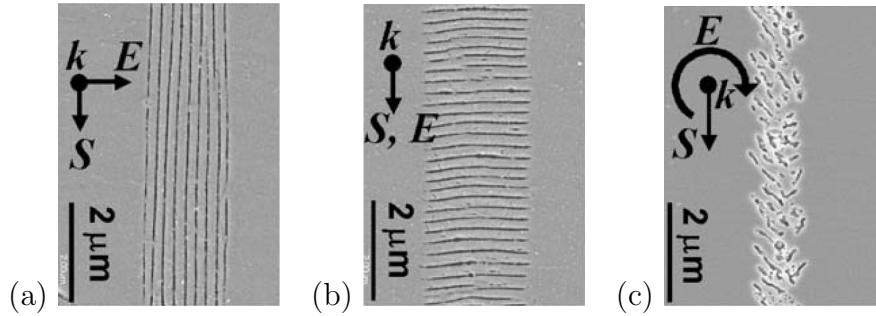


Figure 2.6: Polarization-dependent nanostructure in the transverse writing geometry. The linear polarization  $E$  is (a) perpendicular and (b) parallel to the scan direction  $S$ . The case of circular polarization is shown in (c).[12]

### 2.2.3 Water assisted ablation

Ablation has been observed in almost all materials. It usually begins a few picoseconds after the laser pulse and can be due to several mechanisms such as phase explosion (explosive boiling), evaporation, spallation and fragmentation[91].

Ablation processes are usually confined to the surface, because the formation of debris limits the working depth, by scattering the incident light. This problem is reduced in water-assisted-laser-ablation, which consists in making the ablation process in water instead of air. Water helps in carrying away the debris and reduces thermal accumulation phenomena, acting as coolant. Plasma pressure is shown to increase due to water confinement, preventing it from expanding, and this helps the ablation[92]. Also the plasma duration increases due to confinement, making the ablation process more effective[93]. On the other hand, the formation of bubbles introduces light scattering, thus reducing the efficacy of irradiation absorption[94, 95]. With water-assisted-laser-ablation, microstructuring with much higher aspect ratios than the one in air are obtained[96].

A convenient evolution of the technique involves starting the ablation from the rear surface of a transparent substrate, rather than the top one. Indeed, while ablating the top surface, debris could accumulate near the region of operation, introducing scattering in the light and limiting the 3D capability of the technique. Ablation from the rear surface, on the other hand, doesn't suffer from this problem, since irradiation proceeds from the opposite direction. With this technique, deeper microstructures can be fabricated and three-dimensional channels

can be produced[97, 98]. For instance, complex microfluidic devices, as the one shown in Figure 2.7 (a), are fabricated thanks to a constant motion of the water that increase the debris removal[13]. The depletion of bigger regions than just microchannel has been shown in [14], where a finely threaded through hole (for a male screw) has been fabricated in glass by ablating only the external surface of the volume to remove (Figure 2.7 (b)).

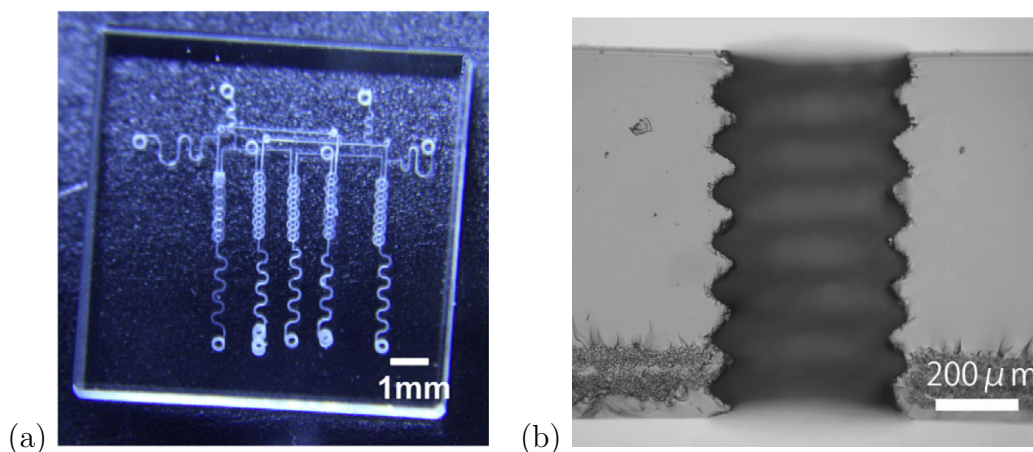


Figure 2.7: (a) Picture of the 3D microchannel based device.[13] (b) Side view of the internal thread fabricated in glass.[14]

In Table 2.1 the main fabrication parameters of the presented ablation studies are reported for a comparison.

In this thesis work, water-assisted-laser-ablation from the rear surface is used to fabricate the micromechanical structure of the device. This is based on a previous work, done in our research group, in which water-assisted-laser-ablation has been studied on EagleXG glass by using pulses of 400 fs ( $\lambda = 1041$  nm) with a repetition rate of 50 kHz, a pulse energy of 3  $\mu$ J, a NA of 0.45 and a writing speed of 500  $\mu$ m/s[6]. Note that the repetition rate has been considerably increased with respect to the one reported in literature, thus enabling higher writing speed than the one used in femtosecond regime. For the device fabrication, an irradiation strategy similar to the one of [14] has been used. Starting from the rear surface,

Work	$\tau_p$ [fs]	$\lambda_{laser}$ [nm]	Rep.[kHz]	$E_p$ [ $\mu$ J]	NA	$v$ [ $\mu$ m/s]	Material
[96]	100	800	1	20-230	0.30	-	Fused Silica
[97]	120	800	1	1-5	0.55	-	Fused Silica
[98]	50	800	1	20	0.3	2	K9 glass
[13]	120	800	1	6	0.45	160	Fused Silica
[14]	$5 \cdot 10^5$	1064(532)	1	90(40)	0.40	1000	Glass slide

Table 2.1: Parameter used in some relevant works on water assisted laser ablation.

the external vertical surfaces of the structure were ablated by the irradiation of lines  $1\ \mu\text{m}$  spaced in the vertical direction. The horizontal surfaces were instead fabricated by the irradiation of a shrinking pattern. After the ablation of the external surface, the box falls, leaving an empty space in the sample. To help the box removal, an ultrasound bath is used. A schematic structure of the pattern used for the ablation of a box is shown in Figure 2.8 with the experimental result.

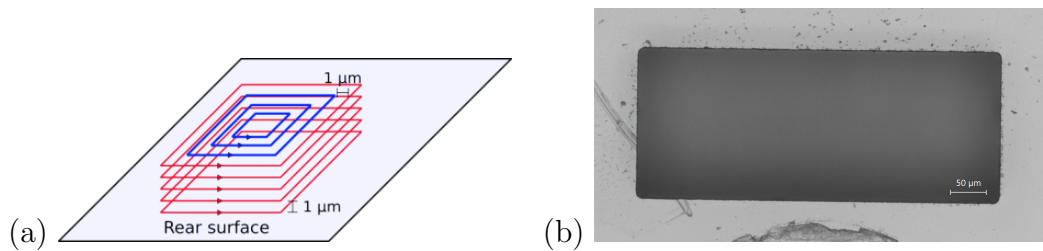


Figure 2.8: (a) Scheme of the irradiation pattern for the ablation and removal of a box structure. (b) Picture of a depleted box.[6]

## 2.3 Examples of devices

We describe here a few representative examples of devices, realized by femtosecond laser micromachining, which allows to illustrate the unique potentials of this technique and its versatility.

Kim *et al.*[15, 16] demonstrated a glass-based optofluidic device for blood cells detection. The device exploited the versatility of femtosecond laser micromachining to combine a microchannel for diluted blood cells flowing (FLICE technique) with two crossing waveguides (one vertical and one horizontal, forming a cross in the center of the channel) for illuminating the cells. The microchannel was fabricated in fused silica by etching with HF the pattern irradiated by a focused (NA=0.55) high repetition rate fiber laser (1 MHz, 500 fs pulse duration, 150-200 nJ pulse energy, 522 nm wavelength). The transverse and longitudinal waveguides were written by scanning respectively with pulse energies of 152 nJ and 84 nJ and with writing speed of  $100\ \mu\text{m}/\text{s}$  and  $10\ \mu\text{m}/\text{s}$ . Thanks to the 3D capability of femtosecond laser micromachining, the microchannel were fabricated with a tapered cross section, which reduces from 10-100  $\mu\text{m}$  to  $\sim 5\ \mu\text{m}$  in the center, where the waveguides are placed, so that to be slightly smaller than the dimension of a

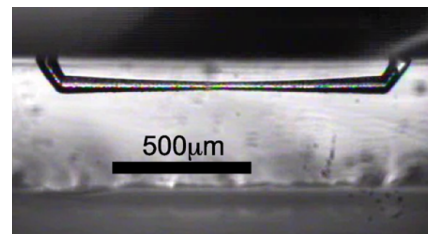


Figure 2.9: Optical microscope image of a typical tapered microchannel.[15]

single blood cell (6-8  $\mu\text{m}$ ) (Figure 2.9). In this way, during its flowing, the blood cell is trapped in the bottle-neck of the channel for an amount of time sufficient to detect it. The two perpendicular waveguides are then used to simultaneously detect the cell, thus increasing the detection capability. Two detection methods were tested (Figure 2.10) and the detection results on the longitudinal waveguide were reported for comparison. An He-Ne laser was coupled into the waveguide to measure the change in transmission from the opposite waveguide induced by the blood cell. The blood cell, having a higher refractive index than the water in which is immersed, acts as a focusing lens, reducing the divergence of the beam exiting the first waveguide and improving the transmission, thus showing an intensity peak. The other method consisted in illuminating the cell with Ar laser and measuring the cell fluorescence from the same waveguides (in this case previously labelled cells were used). This method showed an higher contrast with respect to the transmission measurement. A counting efficiency of 23 particles per second was demonstrated with this device.

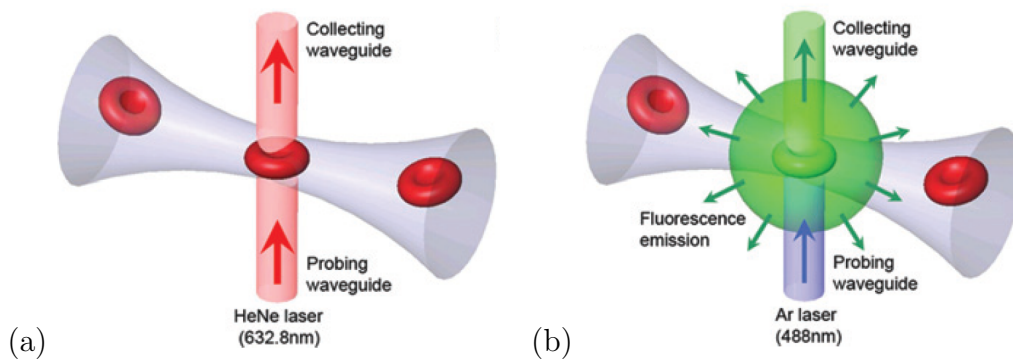


Figure 2.10: Schematic of the two detection methods. (a) Transmission measurement with He-Ne laser. (b) Fluorescence measurement with Ar laser.[16]

Femtosecond laser micromachining has proven also to be integrable with other structuring techniques. Xu *et al.*[17] used FLICE and water-assisted-femtosecond-laser-ablation to machine a microchannel with inscribed surfaces for electrodes deposition. Depositing electrodes into microfluidic channels opens the way to the electrical manipulation of biological samples. In particular, locomotion of specific samples towards the anode or the cathode under the application of an electrical field (electro-tactical control) is an attractive alternative to conventional motion methods. For the fabrication of the 3D microchannels, focused (NA=0.4) fs-laser direct writing (100 kHz, 457 fs pulse duration, 0.25  $\mu\text{J}$  pulse energy, at 1045 nm) at a scan speed of 1500  $\mu\text{m}/\text{s}$  was used, followed by chemical etching and annealing. After FLICE was used for the microchannel excavation, water-assisted ablation was performed on the sidewalls with different geometry to inscribe microcavities with higher roughness, as shown in Figure 2.11. For the ablation step, a higher

pulse energy was used ( $1\text{--}3\ \mu\text{J}$ ) at the same laser conditions. Thanks to the anchoring effect favored by the roughness, a copper film was deposited selectively, with high adhesion, on the ablated parts, forming the basis for the following gold-electrodes deposition (electroless plating process). After gold deposition, vertical sidewall electrodes of  $0.4\ \text{mm}^2$  contact area were obtained (Figure 2.11). The electrodes were successfully used for an electro-tactical control of the flowing direction of a *Caenorhabditis elegans* worm by applying positive and negative DC electric field (Figure 2.12). This demonstrates that the integration of laser ablation and chemical deposition is possible and can be used to fabricate sidewall electrodes monolithically integrated into microfluidic channels for electrical manipulation of biological samples.

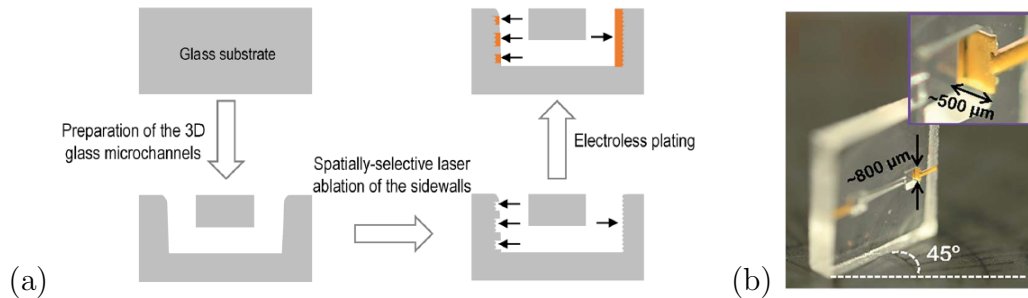


Figure 2.11: (a) Schematic of the procedure for sidewall metal patterning in 3D glass microfluidic structures. (b) Photograph of the on-chip sidewall electrode taken at an angle of  $45^\circ$ . The inset shows a close-up of the electrode.[17]

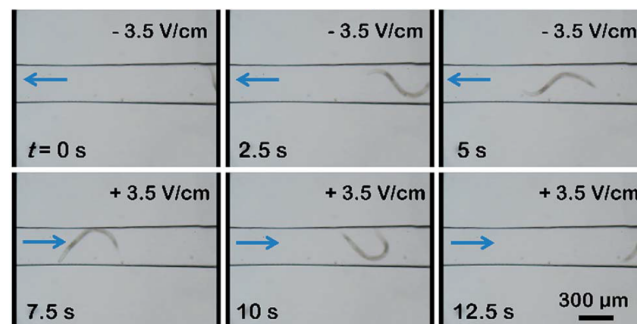


Figure 2.12: Observation of a *C. elegans* worm changing its direction in the microchannel when the polarity of an electric field ( $3.5\ \text{V/cm}$ ) was switched at  $7.5\ \text{s}$ . [17]

The work of I. Bellouard *et al.*[18] is a great example of integration between structural, mechanical and optical elements with a single fabrication technique, thus overcoming any repositioning issues. The device is a high-precision, monolithic, glass-based micro-displacement sensor realized with FLICE and waveguide writing techniques. The complex mechanical structure of Figure 2.13 has been realized by focusing (50x) 100 fs laser pulses at 800 nm with a repetition rate of 250 kHz, scan speed varying between 50 and 2000  $\mu\text{m/s}$  and energy of 0.3  $\mu\text{J}$  for waveguides writing and 0.8  $\mu\text{J}$  for etching. The etching has been carried out in HF. The device exploits an *Integrated Linear Encoder* (ILE) connected to a mobile platform to measure the fine motion of the sensor tip by inducing an intensity modulation into a stationary waveguide. The ILE consists in a series of 9 parallel waveguide as in Figure 2.14 (a). When one of the waveguide is aligned with the stationary waveguide (fed with a 670 nm LED illumination), the output intensity is on a maximum, when the waveguide is displaced, the intensity decrease in a way similar to what presented in Section 1.4.1. The motion of the sensor tip makes the mobile platform and the ILE move, so that the output signal decrease and then increase again when a new waveguide is aligned (Figure 2.14 (b)). The usage of multiple waveguides in the ILE let the sensor measure precisely larger distances than what could be done with a single waveguide. The motion of the mobile platform is guided by a double-compound flexure, a well known structure in precision mechanical engineering for parallel moving (Figure 2.14 (c)). The device was able to measure displacement of more that 0.2 mm with a resolution of 50 nm.

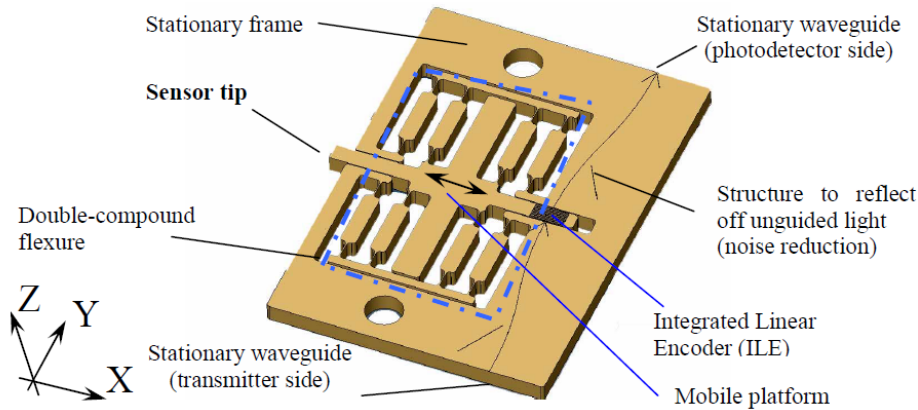


Figure 2.13: Schematic of the motion sensor.[18]

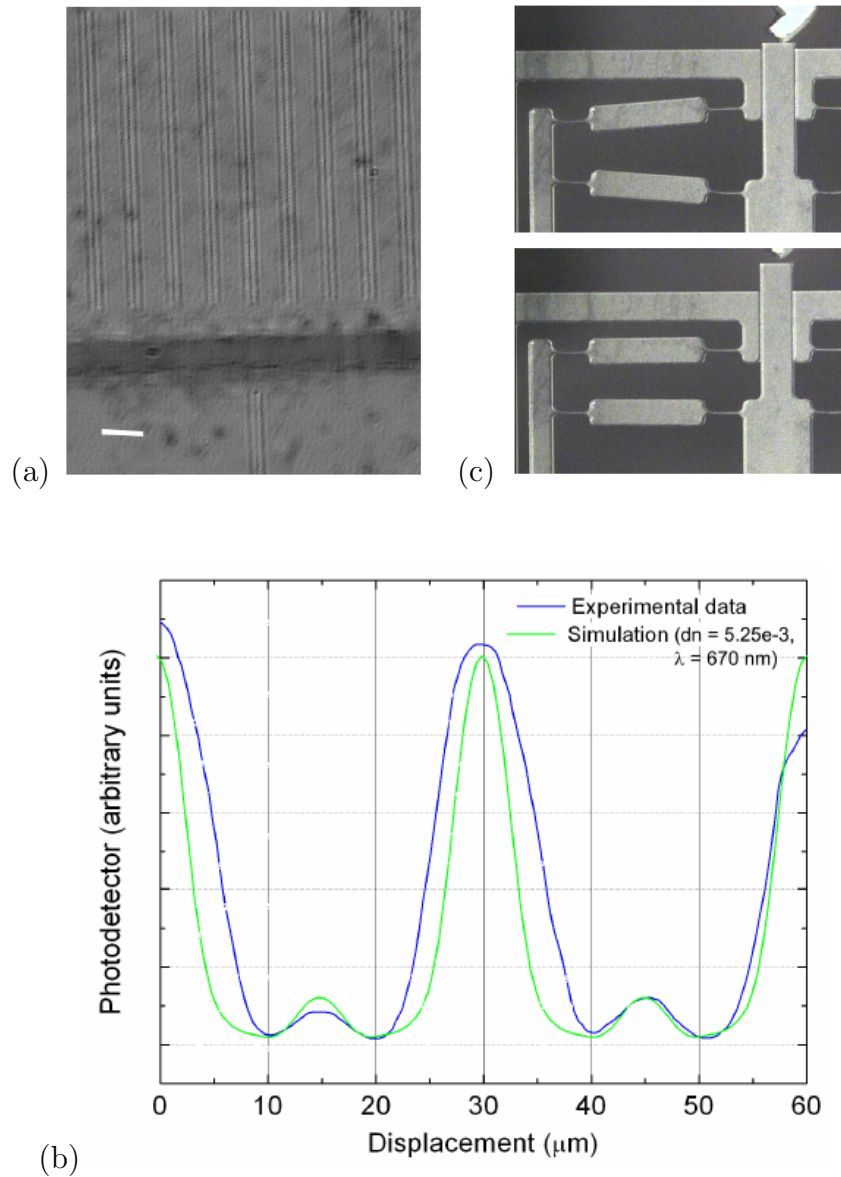


Figure 2.14: (a) ILE (top) and stationary waveguide (bottom). (b) Output behaviour measured and simulated. (c) Particular of the double-compound flexure when moved (top) and in relaxed position (bottom).[18]



# Chapter 3

## Materials and methods

### 3.1 Fabrication setup

#### 3.1.1 Scheme of the apparatus

In this thesis work, femtosecond laser waveguide writing and water assisted laser ablation are employed for device fabrication. The complete fabrication setup is presented hereafter and is schematized in Figure 3.1.

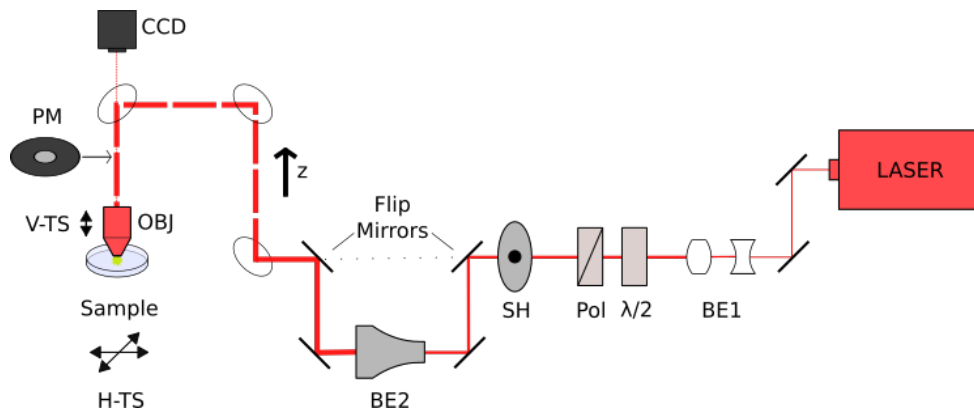


Figure 3.1: Schematic of the fabrication setup. BE1,2: beam expanders;  $\lambda/2$ : half-waveplate; Pol: polarizer; SH: Shutter; PM: power-meter; OBJ: objective; V,H-TS: vertical and horizontal translation stages.

Laser pulses are provided by a commercial infrared laser, which will be discussed in Section 3.1.2.

Two lenses of -75 mm and 150 mm focal distance are used to expand the beam a first time. A rotating half-waveplate, actuated by a miniature gear-driven rotary stage (Aerotech MPS50GR), is set before a linear polarizer for power control of the beam. A mechanical shutter (Uniblits Electronic LS6S2Z1-NL) follows the power control section so that the optical beam can be blocked during the fabrication

if needed. Two following flip mirrors can be used to bring the beam to a two lens telescope (Thorlabs GBE03-C) used as a further beam expander. The beam is then raised up from the optical table with a series of mirrors, so that it can irradiate the sample from above. A water immersion 20x objective with NA=0.5 (Zeiss W N-ACHROPLAN 20x/0.5) focus the beam onto the sample.

The objective and the sample are mounted on translation stages that can control their reciprocal positioning.

The beam power can be measured by a power-meter (Coherent LM-3) which can be inserted before the objective and is removed during fabrication.

Finally, a CCD camera (Thorlabs CP02T/M) is located on the back of the last dielectric mirror to monitor the back reflection of the beam from the sample. This is used to evaluate the focus condition.

### 3.1.2 Femtosecond laser source

The femtosecond laser source is a commercial Satsuma HP<sup>2</sup> laser from Amplitude. It is a compact (tabletop) diode-pumped ultrafast fiber amplified laser system. The fibers are Ytterbium-doped photonic crystals able to amplify pulses up to multi-micro Joule level. The fibers are single mode and the output beam has a Gaussian propagation factor  $M^2 < 1.2$ .

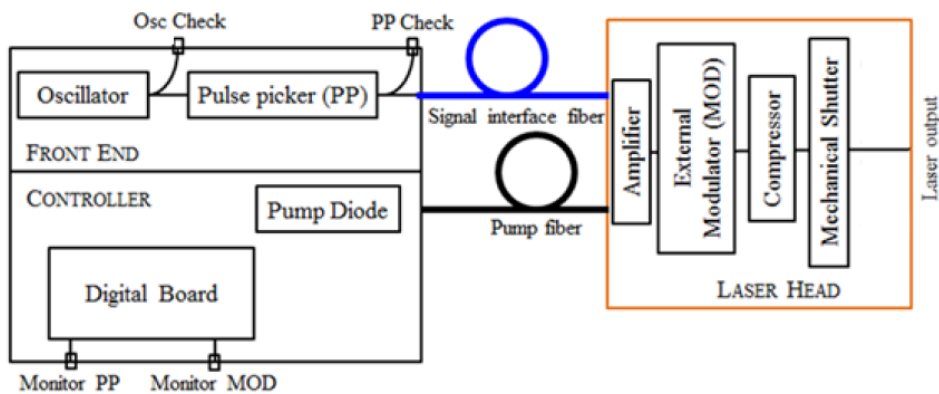


Figure 3.2: Schematic of the femtosecond laser source as presented by the producer.[19]

As shown in Figure 3.2, the laser is composed by a front end, a controller and a laser head. The front end consists of a mode-locked laser oscillator to generate the pulses, a pulse picker to select them and a pre-amplifier stage. The controller has a high-power pump diode and a digital motherboard to generate synchronization signals. The pump diode is connected to the head with a multimode fiber, while the output of the oscillator is coupled to a single mode fiber. The two fibers deliver their power to the main fiber amplifier inside the laser head. An external

acousto-optic modulator is then applied. The compressor stage reduce the pulses up to 250 fs and a mechanical shutter at the end can be used to block the laser.

The repetition rate of the pulses can be controlled using the pulse picker and the acousto-optic modulator. The oscillator produces a pulse train at 40 MHz that is reduced by the pulse picker to 500, 1000 or 2000 kHz. The choice of this repetition rate influences the maximum pulse energy that is respectively 40, 20 and 10  $\mu\text{J}$  without affecting the average power. The repetition rate can be further reduced (by the operator) of a factor  $N$  by the acousto-optic modulator ( $f_{AO} = f_{PP}/N$ ). This modulation operates after the amplification, so it doesn't affect the pulse energy, but reduces the average power.

The laser operates in the infrared (wavelength of 1030 nm) and has a maximum power of 10 W. In our case the pulse picker is set to 1 MHz and the repetition rate is controlled by the acousto-optic modulation (in our work we use 1000 and 50 kHz for waveguide writing and ablation respectively).

### 3.1.3 Translation stages

The objective is mounted onto a vertical translation stage (Aerotech ANT130-035-L-Z-25DU). This let the objective travel 35 mm with a resolution of 2 nm; it can move at a maximum speed of 200 mm/s with a maximum acceleration of 10  $\text{m/s}^2$  (with no load).

The sample is suspended by two millimetric lateral supports and mounted into a Petri dish. It is then immersed in water. The Petri dish is fixed by a custom holder onto a gimbal (Thorlabs GM100/M) with two rotatory axes to set the sample exactly orthogonal to the irradiating beam.

The gimbal is moved by a two direction translation stage (Aerotech ANT95-XY-050). This stage enables a 50 mm translation on both axis, with 1 nm resolution. The maximum velocity and acceleration are 500 mm/s and 27  $\text{m/s}^2$  respectively (without load).

The translation stages can be controlled by the proper computer program (Aerotech A3200 CNC) for high complexity 3D movement. With the same program, also the rotating plate and the shutter described in Section 3.1.1 are controlled. During fabrication, the control of these elements is automatized by loading the proper G-code.



## 3.2 Characterization of microstructures

### 3.2.1 Optical microscope

After the fabrication process the first characterization of the realized microstructures is performed using an optical microscope.

In our laboratory two microscopes are available: a Leica DM2700 M with reflection illumination and a Nikon Eclipse ME600 with both reflection and transmission illumination. Reflection illumination is suggested for the characterization of ablated structure since it is more sensible to surface reliefs. Transmission illumination is instead preferred for discerning the small refractive index differences of waveguides fabricated in bulk. The two optical microscopes provide a magnification power ranging from 4x to 50x. Focus and illumination conditions can be finely adjusted to get the best result. The observation is carried out in real time by a CCD, coupled to the microscope, connected to a computer.

After having assessed the success of the ablation process, a qualitative evaluation of the shape of the structure and its surfaces roughness is done. The calibration of the CCD camera allows also to take quantitative measurements of the size of the fabricated features. The observation can be carried out onto different sides of the structure to completely assess the quality of the fabrication.

### 3.2.2 Actuation of resonant structures

To evaluate the resonant properties of the fabricated structures, a proper method for actuation and detection must be adopted. The setup is schematically shown in Figure 3.4.

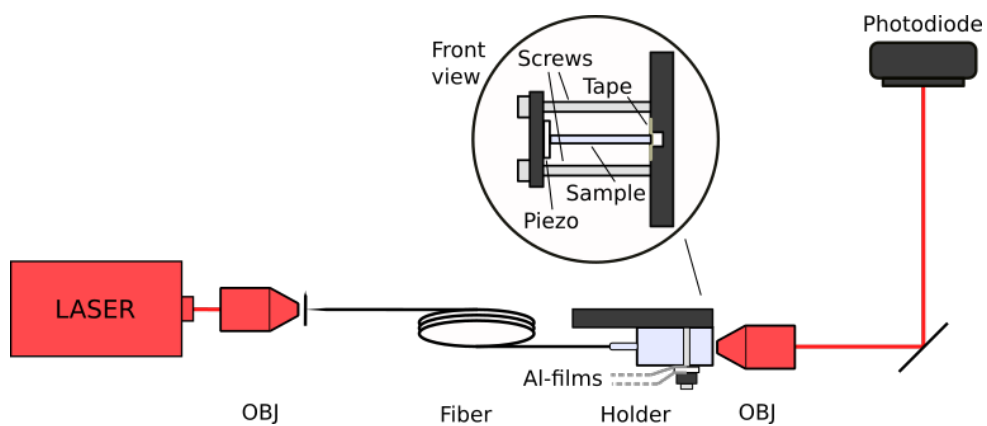


Figure 3.4: Schematic of the setup for oscillation analysis. The bubble presents the detail of the front view of the support.

The device is clamped between a piezoelectric plate (PI Ceramic PRYY+0354) on one side and an elastic rubber tape on the opposite side. The clamp is fixed

to the holder by two screws, which can be used to control the clamping strength. On both sides of the piezoelectric plate, an aluminum film allows for the electrical connection to the function generator (Tektronix AFG3011C). The latter can produce sinusoidal signals at a frequency up to 20 MHz and an amplitude up to 20 V peak-to-peak. The piezoelectric plate is made of PIC255 which has a piezoelectric coefficient  $d_{33} = 400 \cdot 10^{-12}$  m/V, which relates the voltage applied to the increase in thickness of the plate. The mechanical oscillation induced by the maximum 20 V peak-to-peak signal is thus 8 nm peak to peak.

The detection of the oscillations is carried out by measuring the optical signal exiting from the device. Light from a diode laser at 1550 nm is coupled in the device by a single mode fiber. An aspheric lens collects the output signal and focus it onto a 10-MHz-bandwidth InGaAs amplified photodiode (Thorlabs PDA20CS-EC), connected to an oscilloscope (Tektronix DPO2024B) with 200 MHz bandwidth.

### 3.3 Characterization of waveguide device

#### 3.3.1 Microscope observation

As for microstructures, it is common practice to observe the waveguides at the optical microscope in order to spot discontinuities or defects occurred during the fabrication.

Due to the beam deflection induced by the edges of the sample during the fabrication process, waveguides usually don't start and finish precisely at its lateral facets, but a few hundreds of microns inside of them. Moreover, if the input and output facets of the sample are not smooth, losses due to scattering from a rough surface can be induced. For these reasons the two lateral facets of the sample must be properly polished removing a few hundreds of micron of material on each side. A microscope observation of the two facets is required in order to assess their quality and to be sure that the waveguides have reached the edges of the sample. The typical tear-drop shape of a waveguide, as can be observed at the optical microscope after polishing, is shown in Figure 3.5.

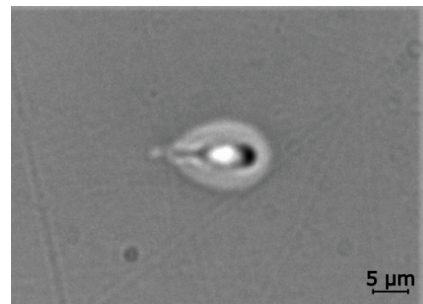


Figure 3.5: Microscope image of a waveguide facet.

### 3.3.2 Optical transmission

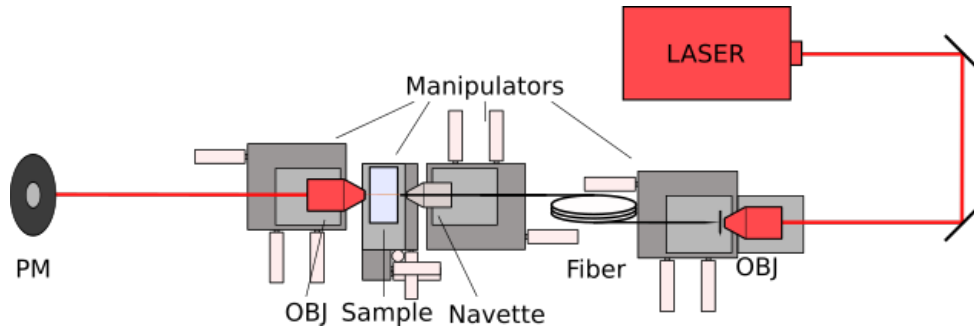


Figure 3.6: Schematic of the optical setup for the characterization of the transmission.

The setup for waveguides characterization is shown in Figure 3.6.

The light source is a 1550 nm diode laser, which is fiber-coupled using a 0.25 NA objective. A 3-axis manipulator is used to align the tip of the single mode fiber with the focal point of the objective.

The other end of the fiber is attached, using a fiber navette, to another 3-axis translator. This is required to align the fiber output to the input facet of the waveguides in the sample.

The sample is mounted onto a 4-axis manipulator able to move and rotate the sample on the two orthogonal directions with respect to the fiber. To facilitate the alignment, an optical microscope (Leica MZ 125) can be used. The manipulator is used also to move the sample so that to pass from one waveguide to the other. At the output face of the sample, another objective with higher NA (usually 0.4) is used to collect light and focus it onto a power-meter (Ophir Photonics NOVA II).

The transmission measurement is carried out by recording the output power of the waveguides, to be compared to the power coming from the input fiber. It is important to keep the laser power constant during all the process in order to perform reliable measurements.

### 3.3.3 Guided mode

For the analysis of guided mode, a setup similar to the one presented for optical transmission is used, with the difference that the power-meter is replaced by a CCD camera (Xenix Bobcat-640-GigE-10331).

The laser power must be adjusted for each measurement in order not to reach saturation of the camera. The magnification ratio must remain the same for all measurements, so that different waveguide modes can be directly compared.

The guided mode of an optical fiber is typically acquired at the end of the measurement, for comparison and calibration purposes.

The analysis of mode dimension is carried out by a custom Matlab program. For the calibration step, the program receives as an input the known mode dimension of the fiber (from fiber producer) and the collected image of the fiber mode. The program then executes a fit of the intensity profile with a Gaussian function. By comparing the fitted spot dimension (in pixels) and the nominal one from the producer (in micron) the calibration is completed. Loading now into the program the acquired modes of the waveguides, it is possible to measure their size. The program can also calculate the overlap integral between the mode profile of the fiber and the one of the waveguide.

### 3.3.4 Losses

In Chapter 1 we have introduced many sources of losses and how to evaluate them. Here we present a practical procedure to fully characterize a waveguide in terms of losses.

For what concerns coupling, Fresnel and propagation losses, straight waveguides are used. First, from a transmission measurement we recover both the power exiting the waveguide  $P_{out}$  and the one exiting the fiber  $P_{in}$ . The insertion loss is evaluated as  $IL = 10 \log(P_{in}/P_{out})$ .

Then a guided-mode analysis is used to obtain the overlap integral  $OI$ , from which the coupling loss is recovered by  $CL = -10 \log OI$ .

Fresnel losses due to air-glass interface is simply  $FL = -10 \log \left\{ 1 - \frac{(n_g - 1)^2}{(n_g + 1)^2} \right\}$ , which is straightforward once we know the refractive index of the glass  $n_g$ .

Thus, for straight waveguides of length  $l$ , the propagation losses are simply recovered from Equation 1.4 as  $PL = (IL - CL - FL)/l$ .

For evaluating the bending losses, on the other hand, we realize a sample with a reference straight waveguide and s-bent waveguides with a different radius of curvature each. So, once obtained from a transmission measurement the IL of each s-bent waveguide and of the reference one, the bending losses for every radius of curvature can be simply evaluated by  $BL = (IL_{bend} - IL_{ref})/l_{bend}$ .

### 3.3.5 Coupling between waveguides

To evaluate the evanescent coupling between two waveguides, i.e. their coupling coefficient  $k$ , a common practice is to fabricate directional couplers.

The directional couplers should be fabricated with a common interaction distance  $D_c$ , while their interaction length  $L_c$  should be varied (the two quantities are indicated in Figure 3.7). This is needed in order to recover the oscillat-

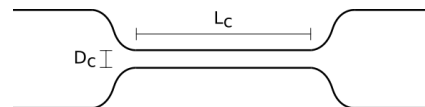


Figure 3.7: Schematized directional coupler.  $L_c$ : interaction length;  $D_c$ : interaction distance.

ing behaviour of the output with respect to the interaction length, described in Section 1.1.3.

For this measure, the setup of Section 3.3.2 should be properly adapted. The output behaviour of a directional coupler depends on the entering polarization, due to birefringence of the waveguides, thus a polarizer is put into the optical path, as shown in Figure 3.8. A half-waveplate is put in cascade to select the direction of the polarization. Since common fibers usually induce random phase rotation, an objective is preferred to directly couple light into the waveguide.

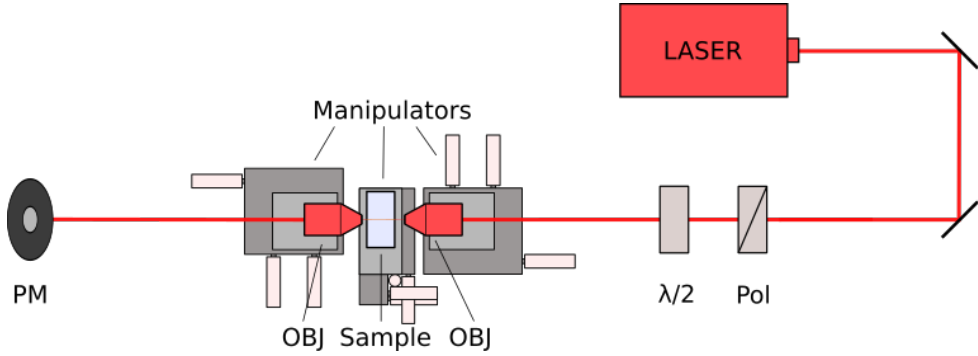


Figure 3.8: Schematic of the setup for characterizing the coupling between waveguides.

The measurement consists in entering one of the two waveguides of each coupler with either vertical or horizontal polarization and then recording the output power from both the bar and cross output port ( $P_{bar}$  and  $P_{cross}$ ). We recall that with bar port, we refer to the output of the waveguide into which the signal is initially coupled, while with cross we refer to the output of the second waveguide. The splitting ratio of the coupler is

$$T = \frac{P_{cross}}{P_{cross} + P_{bar}} = \sin^2(kL_c + \phi_0) \quad (3.1)$$

where  $\phi_0$  is a phase term due to the coupling of the bent part of the waveguides. Clearly, by measuring  $T$  for couplers with different  $L_c$  (but same  $k$ , i.e. same waveguide separation  $D_c$ ), it is possible to estimate  $k$  and  $\phi_0$  from fitting a function of the kind of Equation 3.1 on the experimental data. Note that here we are assuming a coupler with two identical waveguides (but a similar procedure can be used for a  $\Delta\beta \neq 0$  one as well).

### 3.4 Fiber-pigtailing

Fiber-pigtailing is the process to firmly attach a fiber to a waveguide device and it is commonly used for the packaging of complete devices, since it enables the direct connection of the device to a fiber laser source or other fiber-based components. The procedure of fiber-pigtailing makes use of a high-precision alignment system based on two 6-axis hexapods (PI H-811) and a motorized sample manipulator as shown in Figure 3.9. The two hexapods are able to move about 6 mm in height and 15 mm horizontally with a minimum step of 80 and 200 nm respectively. They are also able to rotate of around  $20^\circ$  on the vertical axis and  $10^\circ$  onto the other with a step  $< 5 \mu\text{rad}$ . This enables a fine positioning of the fiber to reduce losses due to tilting and displacement. An optical zoom with magnification 0.75x - 5.5x (Opto 100-ZOS7-25) is mounted above the structure and is equipped with a CCD camera in order to visually check the positioning of the elements. The camera is also attached to translation stages. All motorized equipment is computer controlled. The two hexapods can be controlled also using external controllers.

For the fiber-pigtailing procedure, the optical fiber must be properly prepared. First, the protective cladding should be stripped off. Then, the fiber tip is inserted into a glass ferrule for increase its rigidity and to protect it from breaking. The fiber and the ferrule are fixed together with UV curing glue.

The fiber is mounted onto the first hexapod and it is aligned to the input port of the desired waveguide in the sample, by maximizing the output power. When the optimal position is determined and recorded, the fiber is brought a few millimeters far from the sample, in order to put a droplet of glue on the facet of the sample. The fiber is then moved to the optimal position again, thanks to the high-precision movements of the hexapod. Finally by using an UV lamp, the glue solidify, fixing the fiber.

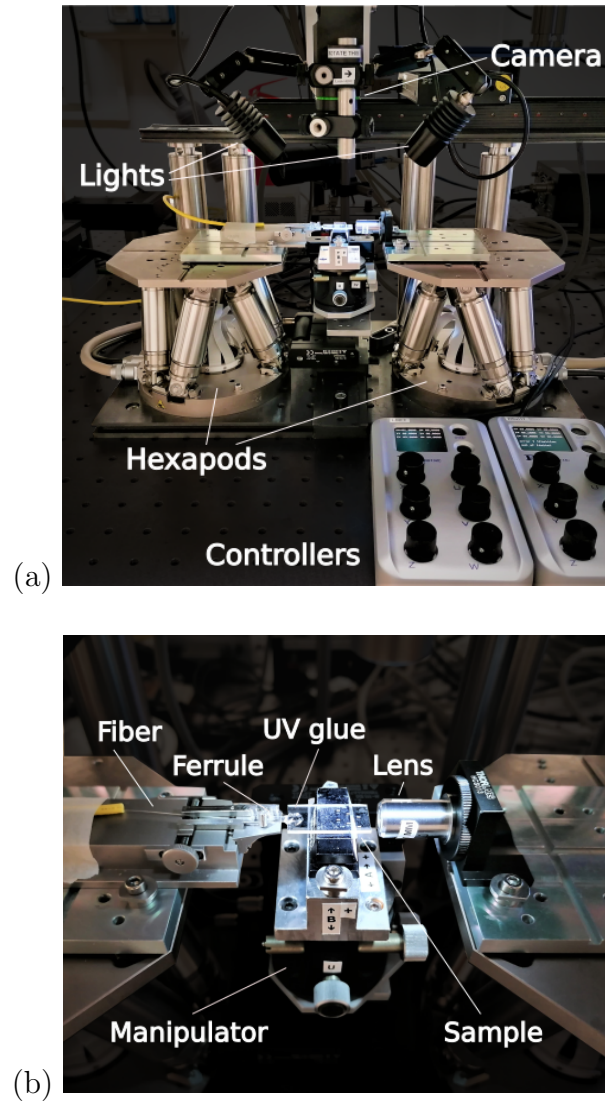


Figure 3.9: Pictures of the pigtail setup. (a) Instrumentation (b) Zoom over the sample area after the glue has solidified.



# Chapter 4

## Optimization of the intensity modulator

### 4.1 Analysis of previous cantilever modulators

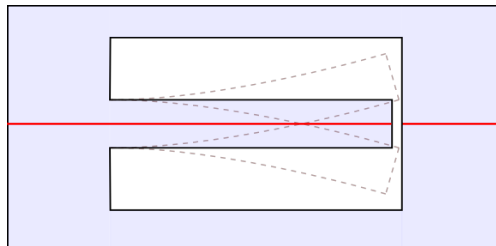


Figure 4.1: Schematized structure of the device with an oscillating cantilever into a cavity and two aligned waveguides (red lines).

This part of the thesis work is dedicated to the optimization of the intensity modulator presented in Section 1.4. We recall that two devices were realized, and that they were based on a cantilever with an embedded waveguide. The oscillation of the cantilever induces a modulation of the coupling efficiency between the waveguide in the cantilever and the one at output, as schematized in Figure 4.1. The two devices have the same nominal dimensions apart from the cantilever lengths which are 1.2 mm and 1.5 mm for *device 1* and *device 2* respectively. The performances of the two realized prototypes were presented in Section 1.4.2, but here we want to focus on the two main issues of such devices and on their possible solutions.

The best modulation results were obtained with *device 1*, thus its measured output is reported in Figure 4.2.

As can be observed, the first problem is that the maximum ER, measured applying 20 V peak-to-peak on the piezoelectric actuator, is 0.4 dB (9 % modulation depth), which is too low for reasonable applications. The ER is determined by

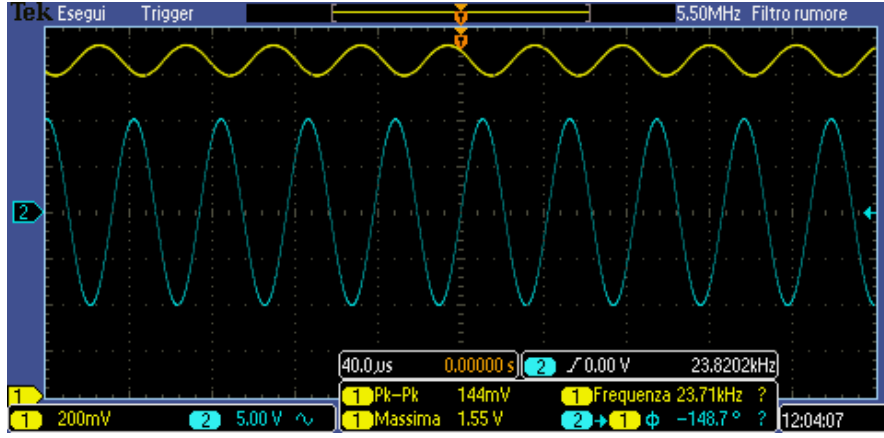


Figure 4.2: Largest oscillation (9 %) observable on the first device. The 23.7 kHz signal, with maximum 1.55 V and peak-to-peak 144 mV, is in yellow while the actuation voltage is in blue.

the maximum coupling efficiency between the waveguide in the cantilever and the waveguide in the bulk of the device. From Equation 1.34 we see that such efficiency is strongly dependent on the mode dimension  $\sigma$  and on the maximum displacement  $d_{max}$  of the cantilever tip. We can directly relate the ER to those quantities as:

$$ER = -10 \log \left( \exp \left( -\frac{d_{max}^2}{\sigma^2} \right) \right). \quad (4.1)$$

Thus, a possible strategy to increase the modulation depth, is to reduce the dimension of the guiding mode. Another strategy could be to increase the maximum displacement. This could be done by fabricating a cantilever with a higher Q factor or by improving the actuation mechanism, for example providing a higher voltage to the piezoelectric.

The other issue is the behaviour of the output, which oscillates at the same frequency ( $f$ ) of the given actuation, rather than twice of it ( $2f$ ). The output maximum should correspond to the rest position of the cantilever, since the waveguide in the cantilever and the one in the bulk are perfectly aligned, being fabricated with the same laser scan. Thus, the maximum should be reached twice during a period of oscillation. What is instead observed in device 1 is a single output peak for each actuation period. Device 2 presented an analogous behaviour up to almost maximum actuation voltage (which was 20 V peak-to-peak), at which a second peak appeared. However the two peaks were asymmetrically distributed in time and the output minima between them had very different depths. To solve this issue, that affects also the modulation depth, a more accurate analysis on the causes of this asymmetry should be carried on.

## 4.2 Maximization of the Extinction Ratio

### 4.2.1 Waveguide optimization

The first strategy to increase the ER of the modulator, is to find a waveguide with a mode dimension smaller than the one used in the previous devices, without increasing the optical losses.

For the choice of the waveguide, a sample with 30 single scan straight waveguides was fabricated and characterized. Three scan speeds (10, 20, 40 mm/s) and pulse energies ranging from 295 to 730 nJ (increasing the energy of  $\sim 10\%$  for each step) were tested. Repetition rate was fixed at 1 MHz, the pulse duration was 250 fs and a water immersion 20x objective with 0.5 NA was used (see also Chapter 3).

The modified region around the fabricated waveguides presented the typical tear-drop shape shown in Section 3.3.1 and no discontinuities were found. The waveguide optimization was carried out for 1550 nm operation wavelength, in accordance to the previous work. From a mode characterization with a CCD, waveguides fabricated with pulse energies above 400 nJ were found to be multimode, therefore were discarded. For our scope, the best waveguides were the ones written at 10 mm/s and pulse energies 330 nJ and 365 nJ, presenting both a circular mode of radius  $\leq 6.5 \mu\text{m}$ , coupling loss with standard single mode fiber  $\leq 0.5 \text{ dB}$  and propagation loss  $\leq 0.4 \text{ dB/cm}$ .

With this optimization we were able to provide a waveguide with a smaller mode than the one previously used ( $8 \mu\text{m}$ ), with good propagation losses.

### 4.2.2 Maximization of the displacement

To improve the output modulation, the oscillation of the cantilever should be enhanced, in order to maximize the displacement between the two waveguides.

From Equation 1.27 we know that a shorter cantilever that resonates at higher frequencies has a higher stiffness  $k$  that should increase the  $Q$  factor ( $Q = (\sqrt{mk})/r$ ), if the other terms are constant. For this reason, we chose to fabricate a shorter cantilever than the previous ones, with a length of 1 mm, in the attempt of getting an higher  $Q$  factor. Indeed, we recall that the  $Q$  factor linearly relates the amplitude of oscillation of the actuator with the one of the cantilever tip, at resonance.

To further increase the maximum displacement of the cantilever tip, the actuation setup was improved. To double the peak-to-peak voltage applied to the piezoelectric actuator  $V_{piezo}$ , the external load resistance  $R_L$  of the function generator was removed. Normally, to provide a voltage  $V_{piezo}$ , the function generator applies  $V_{FG}$  to the load (Figure 4.3). The load resistance is equal to the output resistance  $R_{out} = 50 \Omega$  of the function generator and so  $V_{piezo} = \frac{R_L}{R_{out} + R_L} V_{FG} = \frac{V_{FG}}{2}$ . Removing the load, the relation reduces to  $V_{piezo} = V_{FG}$ , since the piezo can be considered as an infinite resistance. In this way, the maximum peak-to-peak voltage that we can apply onto the piezoelectric actuator passes from 20 to 40 V.

Moreover, in preliminary tests, two piezoelectric were stacked and connected in parallel to the function generator, to further double the actuated displacement with a given applied voltage (reaching the equivalent of applying 80 V peak-to-peak).

Later on, an inductive transformer able to perform a x3 amplification was used, instead of stacking 2 piezo together.

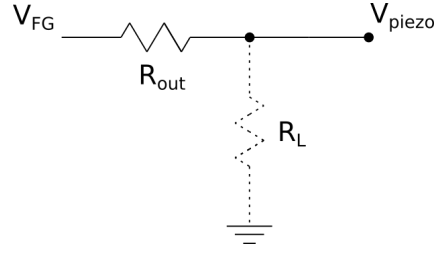


Figure 4.3: Simplified scheme of the function generation output. The dashed line represents the load resistance that has been removed.

### 4.2.3 Modulation improvement

The new device, a 1 mm long cantilever (35.5 kHz resonance frequency) with the optimized waveguide, was fabricated and its output measured to evaluate the modulation amplitude it could obtain.

When 20 V peak-to-peak were applied on the piezoelectric, as with the previous devices, an ER of  $\sim 3$  dB (50% modulation depth) was obtained (Figure 4.4 (a)), proving that the two changes made (the smaller mode waveguide and the shorter cantilever) were effective. Two peaks can be clearly seen during a period of oscillation, even though their distribution is still asymmetric.

After the removal of the load resistance, 40 V peak-to-peak are applied to the piezoelectric. As expected, the modulation strongly increase, reaching an ER of  $\sim 7$  dB (80% modulation depth) as shown in Figure 4.4 (b).

Using the two stacked piezo actuators, an almost complete modulation was reached, with an ER  $\sim 13$  dB (95% modulation depth). In this case, we see that the oscillation is wide enough to almost equalize the minima between the peaks (Figure 4.4 (c)).

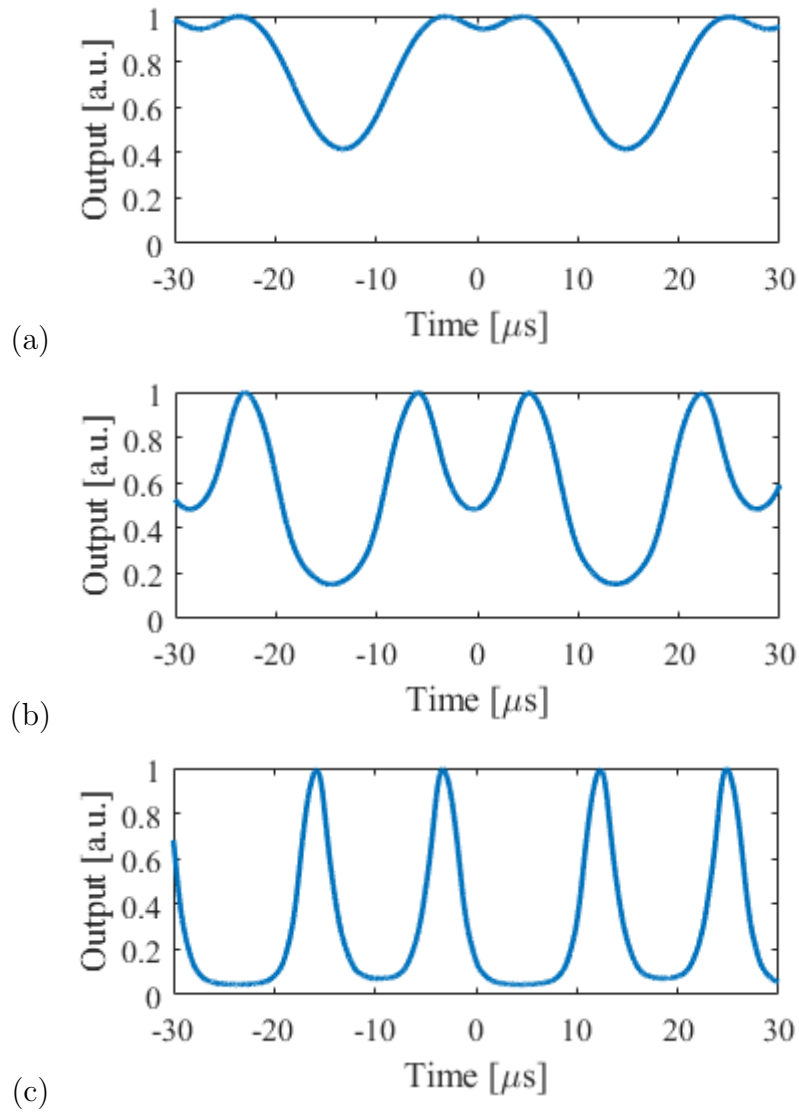


Figure 4.4: Normalized output of the device, measured at the photodetector, when 20 V (a) and 40 V (b) peak-to-peak are applied onto the piezoelectric actuator. (c) Case of 40 V peak-to-peak applied onto two piezoelectric actuator.

## 4.3 Asymmetry correction

### 4.3.1 Analysis of the problem

Two peaks were clearly visible during a period of oscillation. The peaks were not evenly distributed in time, as also observed in *device 2*.

As a first measurement, we evaluated the time interval between consecutive peaks. In a period of oscillation  $T = 28.1 \mu\text{s}$ , the time interval between the two peaks are  $T_1 = 15.4$  and  $T_2 = 12.7 \mu\text{s}$ . We define now, as a figure of merit to compare future devices, the asymmetry:

$$A = \left| \frac{T_1 - T_2}{T} \right| \quad (4.2)$$

that takes a value of 1 when just one peak is seen and 0 when the two peaks are equally distributed. In this case  $A \sim 9.6\%$ .

This asymmetric behaviour could be due to the shift of the center of oscillation of the cantilever, which no longer corresponds to the perfect alignment between the two waveguides. If we introduce a shift  $D$  in the model of Section 1.4.1, indicating that the two waveguides are misaligned by that quantity when the cantilever is at rest position, we get a coupling efficiency:

$$\eta(d) = e^{-\frac{(d+D)^2}{\sigma^2}} \quad (4.3)$$

where  $d$  is the sinusoidal displacement induced by the oscillation:

$$d = d_{max} \sin(\Omega t). \quad (4.4)$$

Figure 4.5 presents the simulation of the output signal, for increasing oscillation amplitudes, when the rest position of the cantilever is at a distance  $D$  from being aligned with the output waveguide. Three maximum displacement are modelled to highlight the main feature of the output in each condition. The displacement from the cantilever rest position is plotted in the same graphs to evaluate the position of the peaks with respect to the oscillation. The schematic of cantilever and waveguide oscillation is reported in Figure 4.5 (a). As can be seen, at small oscillation amplitudes ( $d_{max} < D$ ), the two waveguides are never aligned perfectly and so it is not possible to fully couple light into the output waveguide (Figure 4.5 (b)). In this condition, just one peak for period of oscillation is seen. Increasing the cantilever displacement, as we do by increasing the voltage applied to the piezo, the output increase until saturation, that happens when the two waveguides are aligned (Figure 4.5 (c)). If the maximum displacement is increased further ( $d_{max} > D$ ), the cantilever oscillates enough to bring its waveguide beyond the output one. In this case, the two waveguides are aligned two times during a period of oscillation and thus two peaks are seen (Figure 4.5 (d)). It is clear that the minima between the peaks in this case have a different depth,

since they correspond to a different lateral displacement from the output waveguide. When  $d_{max} \gg D$  the initial distance becomes almost negligible and the two minima reach the same value, but the peak distribution is still asymmetric.

The case of a cantilever with rest position centered with the output waveguide is shown in Figure 4.6 for comparison. In this case the minima have the same value and the peaks are equally spaced.

By using this model, a least square fit of the measured output when 40 V peak-to-peak were applied onto two piezo has been done to recover  $D$  and  $d_{max}$ . A mode dimension of  $6.5 \mu\text{m}$  has been used, as measured in that specific waveguide. The fit, shown in Figure 4.7, provides a distance  $D = 1.89 \mu\text{m}$  and a displacement of  $d_{max} = 13.6 \mu\text{m}$  with a *determination coefficient*  $R^2 = 99.14\%$ .

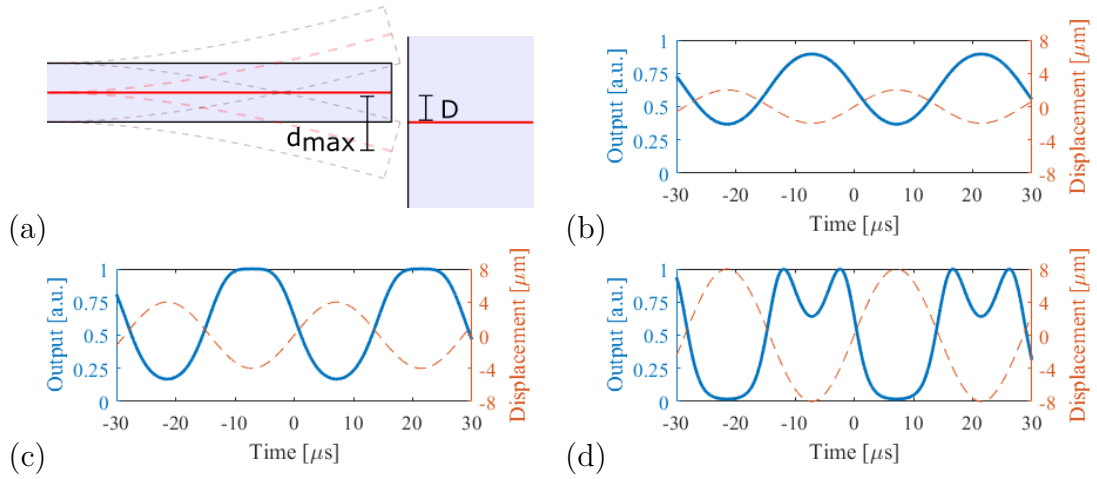


Figure 4.5: (a) Representation of an oscillating cantilever and of the waveguides (red lines). (b-d) Simulations of the device output (blue line) and of the displacement of the tip (red dashed line) when: (b)  $D = 4 \mu\text{m}$ ,  $d_{max} = 2 \mu\text{m}$ ; (c)  $D = 4 \mu\text{m}$ ,  $d_{max} = 4 \mu\text{m}$ ; (d)  $D = 4 \mu\text{m}$ ,  $d_{max} = 8 \mu\text{m}$ .

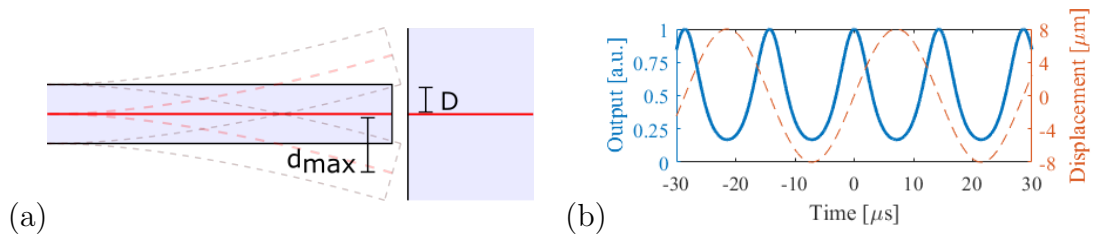


Figure 4.6: (a) Representation of the oscillating cantilever and of its waveguide when they are aligned with the output waveguide at rest position. (b) Simulations of the device output when  $D = 0 \mu\text{m}$  and  $d_{max} = 8 \mu\text{m}$ .

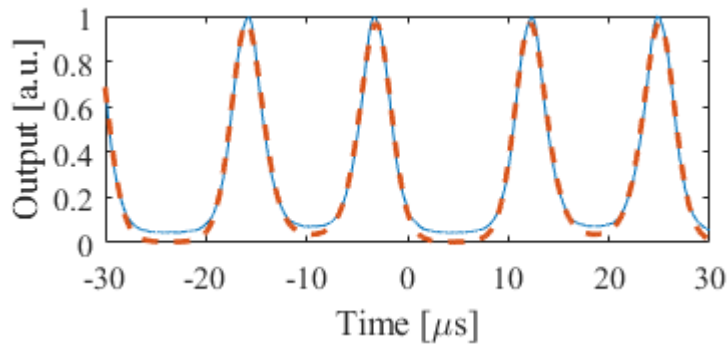


Figure 4.7: Least square fit (red dashed line) of the experimental data (blue line).

**Possible causes** A first hypothesis on the causes of this asymmetry was that the cantilever was bent on one side by its own weight. In fact, in our measurements on the oscillations, the device was mounted vertically on a side. We replaced the setup with a horizontal one and measured the output of the same device. No relevant changes were observed, since the asymmetry was still of  $A = 9.3\%$  and the fitting evaluated a distance of  $D = 1.85 \mu\text{m}$  ( $R^2 = 99.11\%$ ), in the same actuation condition.

An accurate microscope analysis of all the cantilevers fabricated highlighted a systematic curvature difference between the two sides of the basis of each cantilever (Figure 4.8). This aspect may be caused by the fabrication method, which does not process the two side of the cantilever in the same direction, as will be explained in the next section. This could in principle affect the cantilever oscillation and its rest position.

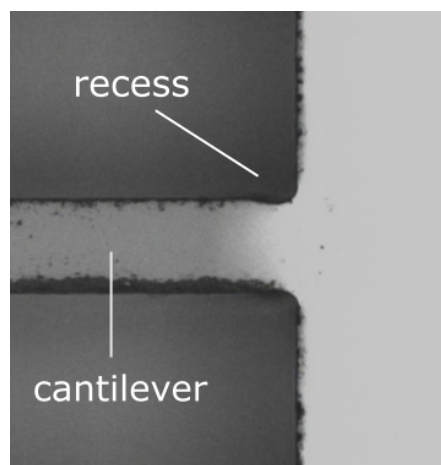


Figure 4.8: Detail of the cantilever basis. On the top side of the basis, a recess is clearly visible.

### 4.3.2 Correction of the fabrication method

**Fabrication pattern in use** To realize the devices, the glass surrounding the cantilever has been divided into many boxes. Smaller boxes are easier to process and it is in general preferred to machine short vertical surfaces, since bubble formation limits the water flow into the thin channels left by the ablation.

For the laser ablation we used a pulse energy of  $1.8 \mu\text{J}$ , a writing speed of  $2 \text{ mm/s}$  and  $50 \text{ kHz}$  repetition rate. The process followed to ablate a box was the same discussed in Section 2.2.3. The pattern used is the one shown in Figure 4.9 (a), where the numbers indicate the order in which the boxes are removed. Note that the lateral surfaces of the external boxes are tilted ( $5^\circ$ ). This has shown to further improve the removal of the ablated box. First, the box on the bottom right is ablated, with an irradiation that encircles the box moving in counter-clockwise direction (looking from above). After the depletion of this box, the second box, just above, is ablated. The same procedure (again with counter-clockwise irradiation) is followed for the two boxes on the left side of the cantilever. The upper part of the cantilever is separated from the glass by a series of parallel straight irradiation lines both from its right and its left side. Now that the water can flow onto the whole top surface, the glass above is removed by the ablation of four boxes. The front tip of the cantilever is separated from the rest of the substrate by the ablation of a last vertical box.

What should be underlined here is that the lateral boxes are all ablated in a counter-clockwise direction, thus the laser pulses process the cantilever surfaces in two opposite directions on the two sides (Figure 4.9 (b)). Moreover, the ablation starts in the bottom right corner of each box, which, for the left-side boxes, corresponds to the cantilever basis. Since the  $1 \mu\text{m}$  step in height is done progressively by a tilted line that starts at the current height and ends at the following one and since it is done on the first side of each box, the left side of the cantilever is machined with inclined lines (even if very slightly), while the right side by horizontal ones.

**Optimized fabrication pattern** To get cantilevers as symmetric as possible, the irradiation pattern of the left-side boxes has been changed to clockwise and the starting point for the ablation moved to the bottom left corner. Moreover, the order of processing the different boxes has been changed in order to machine alternately one box on the right side and then one box on the left side, instead of depleting completely the right side before the left one (Figure 4.10). In this way, also bubble formation was found to be more uniform for both sides.

A microscope inspection onto different cantilevers proved the effectiveness of the optimized machining process. As can be seen in Figure 4.11, no recesses are visible on the side of the basis which presents two equally sharp corners.

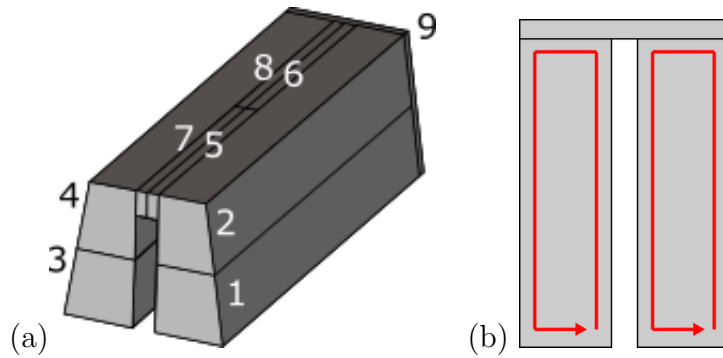


Figure 4.9: (a) 3D in scale representation of the boxes in which the substrate is divided for the ablation. (1-4) Lateral boxes:  $150 \times 150 \times 1010 \mu\text{m}^3$ ; (5-8) Upper boxes:  $25 \times 50 \times 1010 \mu\text{m}^3$ ; (9) Front box:  $350 \times 300 \times 10 \mu\text{m}^3$  (measures refer to the longest edge of each box). (b) Fabrication direction as seen from above.

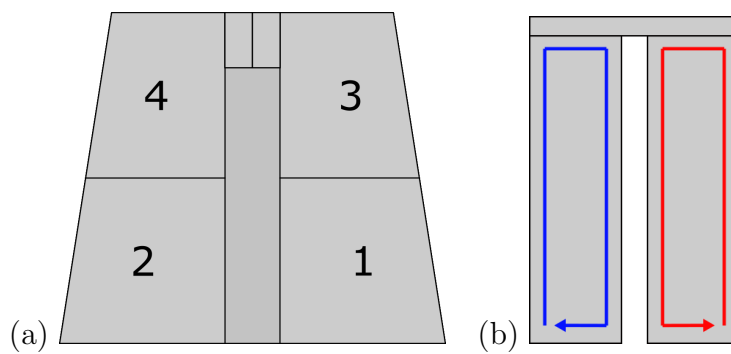


Figure 4.10: (a) Front view representation of the ablated boxes with the number indicating the new fabrication order of the lateral boxes. (b) Fabrication direction as seen from above.

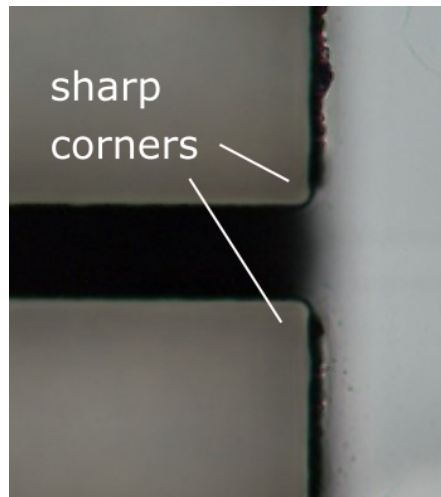


Figure 4.11: Detail of the basis of the cantilever realized with the new method. No recess are present and the corners are sharp as desired.

## 4.4 Fabrication and characterization of an optimized device

Finally, a device with the optimized waveguide ( $E_p = 350$  nJ,  $v=10$  mm/s, 1 MHz) and the symmetric pattern for the ablation ( $E_p = 1.8$   $\mu$ J,  $v=2$  mm/s, 50 kHz) was fabricated and characterized. The cantilever was 1 mm long, with nominal thickness  $t = 50$   $\mu$ m and height  $b = 250$   $\mu$ m by design.

From a microscope inspection, the waveguide presented no interruptions and was well centered inside the cantilever beam. The cantilever basis presented no recesses as expected and a good overall symmetry. The measured size of the cantilever was a bit smaller than designed ( $L = 1000$   $\mu$ m,  $t = 40$   $\mu$ m,  $b = 235$   $\mu$ m) due to tolerances in the ablation process (Figure 4.12).

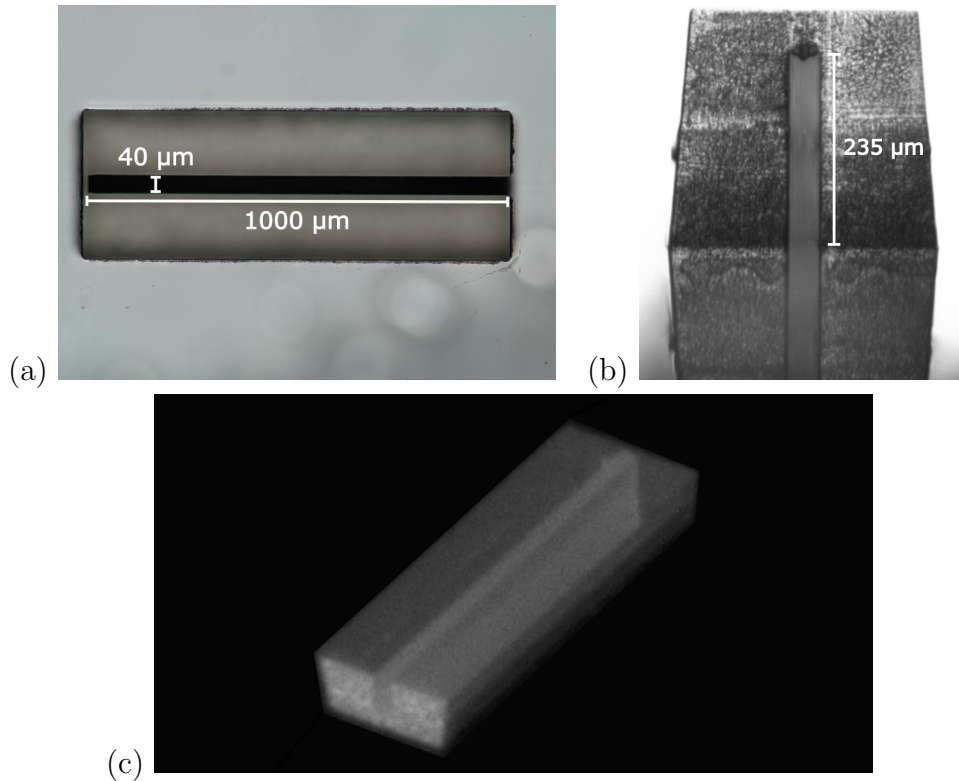


Figure 4.12: Microscope images of the cantilever from top (a) and front (b) with dimensions. (c) Oblique camera photograph of the cantilever.

**Waveguide characterization** The waveguide characterization provided a mode dimension of  $\sigma = 6.5$   $\mu$ m. The device presented IL of 8 dB. Providing that, losses in the straight waveguides (due to coupling, Fresnel reflection and propagation) were about 2 dB, we can deduce that the air-gap between the cantilever and the

following waveguide introduces losses in the order of 6 dB. We suspect that the main contribution to these losses is given by scattering induced by the roughness of the ablated surfaces at the air-glass interface.

**Characterization of natural frequencies** After the waveguide characterization, the input of the device was permanently glued to a single mode IR fiber for the characterization of the oscillating structure as described in Section 3.4.

For what concerns the characterization setup, a voltage transformer has been used to approximately increase the applied voltage onto a single piezo of a factor of 3 as anticipated in Section 4.2.2. The transformer had a frequency range limited to about 300 kHz, as we measured when a capacitive load equivalent to the piezo was applied, therefore the exploration of high order modes was not possible (Figure 4.13).

From the measured dimension of the cantilever, we expect the following natural frequencies for the firsts in-plane oscillations:  $f_1 = 35.9$  kHz,  $f_2 = 225$  kHz. Once fixed the voltage applied to the piezoelectric actuator, the output of the device has been observed at different frequencies, ranging from 1 kHz to some hundreds of kHz. The fundamental mode of oscillation was clearly visible at 35.9 kHz, while the second in plane mode was at a frequency of 223 kHz. Other resonances were experimentally found at 92.8 kHz and 185.6 kHz, which may be due to more complex oscillation modes.

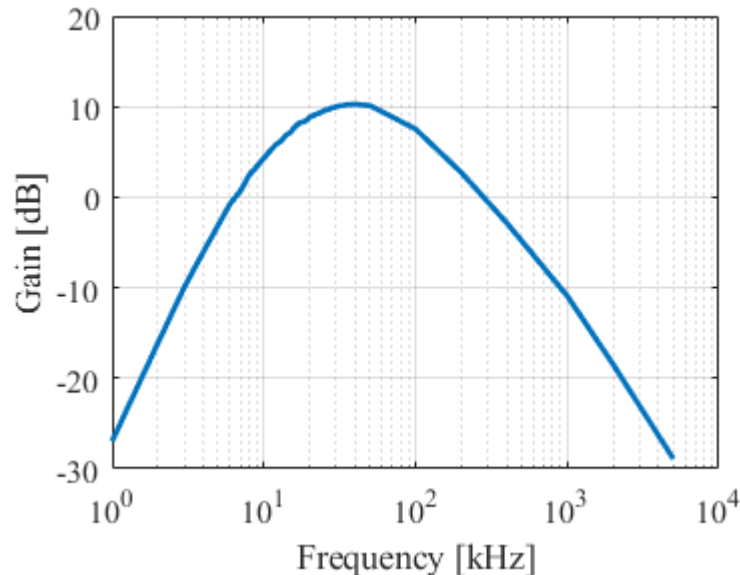


Figure 4.13: Measured frequency response of the custom voltage transformer when a capacitive load of 4.7 nF was used.

**Characterization of resonance peak** After the fundamental mode of oscillation was found, a fine frequency scan around that peak was done with fixed input voltage to retrieve the transfer function between the oscillation of the piezo and the one of the cantilever.

A 40 V peak-to-peak signal was applied to the piezo with frequencies ranging from 34 to 38 kHz. Since the piezoelectric coefficient is known to be  $d_{33} = 400 \cdot 10^{-12}$  m/V, we expect an oscillation with amplitude  $d_{piezo} = 4$  nm.

To estimate the displacement of the cantilever tip, the peak-to-peak voltage was measured at each frequency of actuation  $f_{act}$ . From the knowledge of the mode dimension  $\sigma = 6.5 \mu\text{m}$  and by inverting Equation 1.34, the displacement can be written as:

$$d = \sigma \sqrt{-\ln \left( 1 - \frac{V_{pp}(f_{act})}{V_{max}} \right)} \quad (4.5)$$

where  $1 - \frac{V_{pp}}{V_{max}}$  corresponds to the minimum coupling efficiency  $\eta(d_{max})$  between the cantilever waveguide and the output one.

The displacement and the piezoelectric amplitude of oscillation are related by the transfer function discussed in Section 1.3.1. In particular, we can use Equation 1.13 to fit the ratio  $r = d/d_{piezo}$ , leaving the resonance frequency  $f_{res}$  and the damping coefficient  $\xi$  as free terms. Since we are interested in the shape of the transfer function, a multiplicative factor  $A$  has been introduced and the measurements have been normalized between zero and one to improve the fit:

$$r_{norm}(f_{act}) = \frac{r(f_{act}) - r_{min}}{r_{max} - r_{min}} = \frac{A f_{act}^2}{\sqrt{f_{act}^4 + 2(2\xi - 1)f_{act}^2 f_{res}^2 + f_{res}^2}}. \quad (4.6)$$

where  $r_{min}$  and  $r_{max}$  represents the minimum and maximum measured ratios.

The result of the fit, with determination coefficient of  $R^2 = 99.48\%$ , is shown in Figure 4.14. From the fitted damping coefficient, the  $Q$  factor was estimated to be 463.

**Symmetry characterization** To characterize the temporal asymmetry of the modulation peaks, the time intervals between the peaks of an output at 80 V peak-to-peak input (onto the piezo actuator) have been measured ( $T_1 = 14.1 \mu\text{s}$  and  $T_2 = 13.7 \mu\text{s}$ ), providing an asymmetry  $A \sim 1.5\%$ .

A theoretical output function, as the one used in Section 4.3.1, was also fitted on the acquired signal. In the fit, a mode dimension of  $6.5 \mu\text{m}$  was considered. Figure 4.15 presents the measured signal (blue line) and the one fitted with a determination coefficient of  $R^2 = 95.79\%$  (red dashed line). Thanks to the new fabrication pattern, the estimated distance between the cantilever rest position and the output waveguide reduced to  $D = 0.66 \mu\text{m}$ . The fitting also allows to estimate a maximum displacement of  $13.4 \mu\text{m}$ .

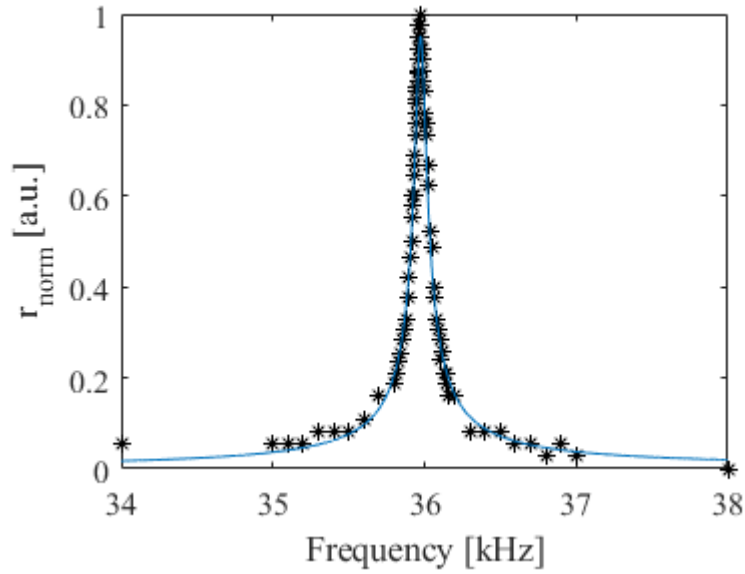


Figure 4.14: Least square fit (blue line) of the transfer function derived from the measurements (stars).

This estimation is comparable to what can be obtained with Equation 4.5 introducing the measured voltages ( $d = 13 \mu\text{m}$  for  $V_{pp} = 648 \text{ V}$  and  $V_{max} = 656 \text{ V}$ ). But, on the other hand, these results are not in accordance to the estimated  $Q$  factor, which can be used to predict the maximum displacement starting from the piezoelectric coefficient and the voltage applied onto the piezo (estimated displacement of  $\sim 7.4 \mu\text{m}$ ).

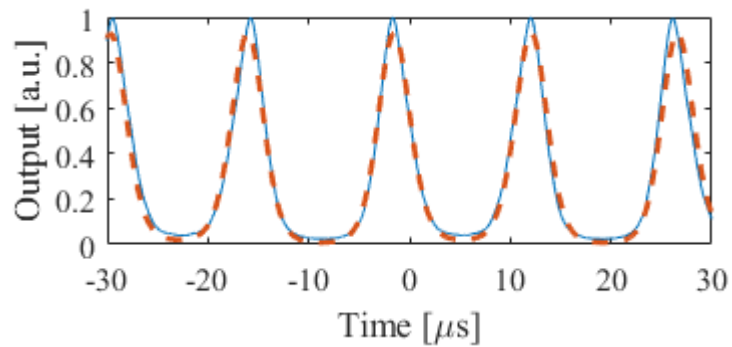


Figure 4.15: Least square fitting (red dashed line) of the normalized oscillating output from the device (blue line).

**Performance of the intensity modulation** Having fixed the actuation at the resonance frequency of the first in plane oscillation, a scan over peak-to-peak input voltages was performed, ranging from 2 V to 120 V. For each actuation voltage, the signal on the oscilloscope was recorded in a time window of about 60  $\mu$ s, in order to perform a more precise analysis on MATLAB.

Figure 4.16 presents the output observed at 18, 40 and 76 V, which we can compare with the one of the previous device at similar input voltages (Figure 4.4). As can be seen, this device presents deeper minima, thus a higher modulation, for the same input voltage. At 80V, thin peaks with deep minima are obtained.

To quantify the modulation capability of the device, we can calculate the ER by using Equation 4.1, that here becomes:

$$ER = -10 \log \left( 1 - \frac{V_{pp}}{V_{max}} \right). \quad (4.7)$$

Figure 4.17 presents the ER in relation to the applied voltage. An ER > 17 dB can be obtained with this device, corresponding to a modulation depth > 98 %.

**Complementary analysis of the maximum displacement** A linear relation between the maximum displacement of the cantilever tip (in one oscillation cycle) and the amplitude of oscillation of the piezoelectric actuator is expected. By means of Equation 4.5, the maximum displacement can be estimated for each input voltage.

Figure 4.18 reports the displacements measured at different input voltages. When no voltage is applied, the (small) measured displacement should be attributed to the presence of noise. Then, the displacement follows the linear behaviour expected. At high voltage, the displacement no longer follows a linear behaviour, since the output minima have reached a value comparable to the noise, so we are no longer able to measure the minimum.

Figure 4.19 presents the linear regression done onto the displacement measured before saturation occurred. From that linear regression a  $Q$  factor of 983 can be estimated, which has doubled with respect to previous calculations. This could be due to the fact that this measure is strongly dependent on the estimated mode dimension. Another reason could be that the noise, which is always present, have worsen the measured values used in the resonant peak analysis, enlarging the peak, thus reducing the  $Q$  factor.

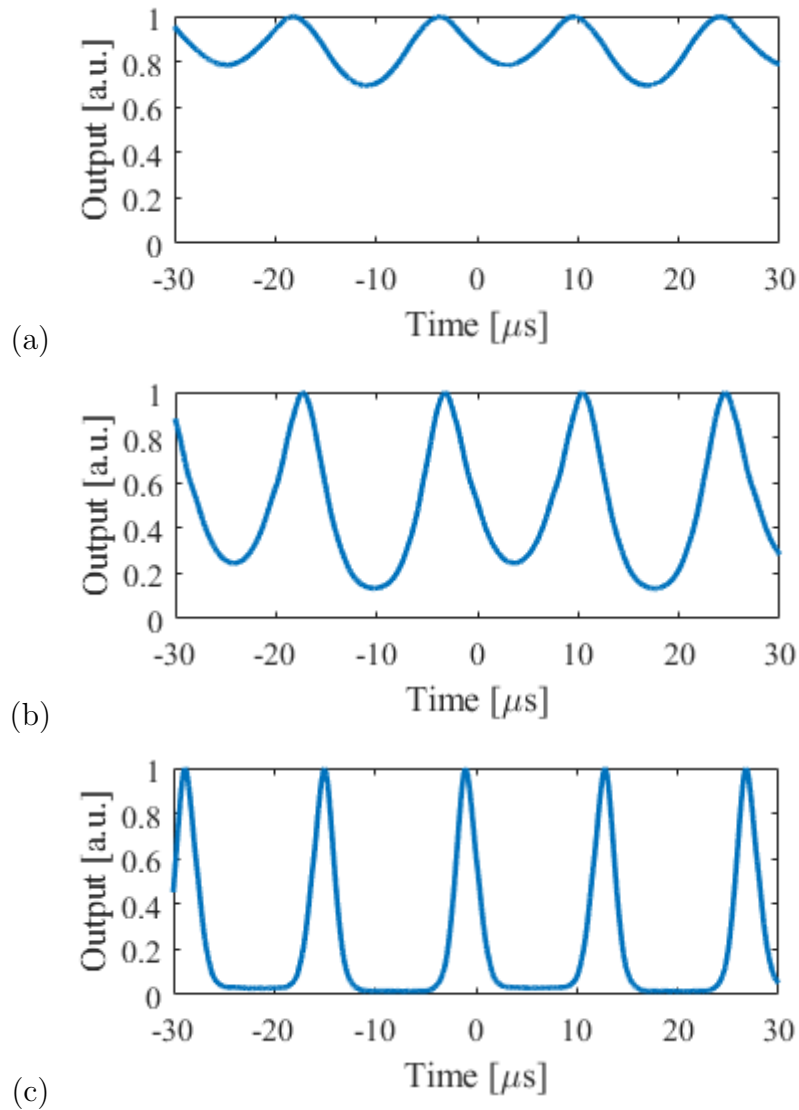


Figure 4.16: Normalized output of the device, measured at the photodetector, when 18 V (a), 40 V (b) and 76 V (c) peak-to-peak are applied onto the piezoelectric actuator.

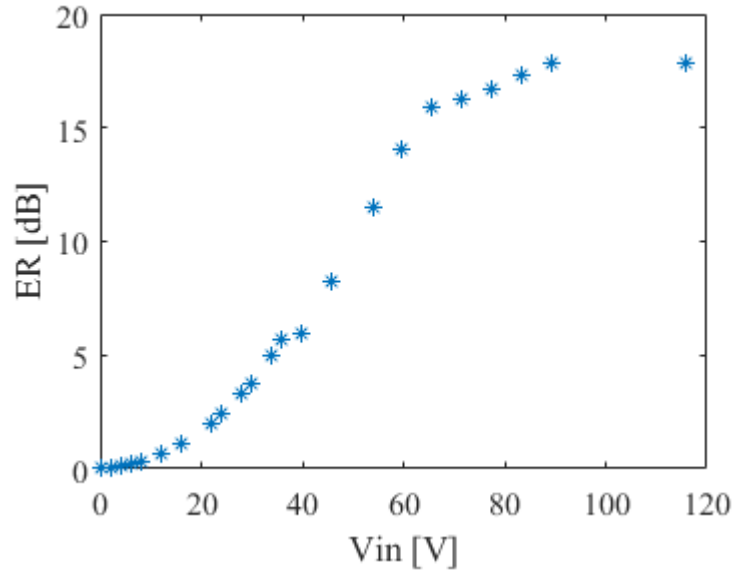


Figure 4.17: Extinction ratio with respect to input voltage (peak-to-peak) onto the piezo actuator.

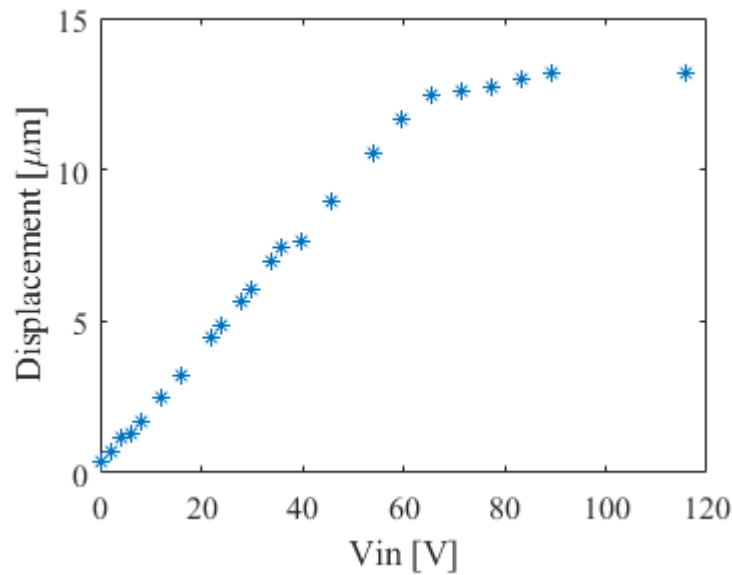


Figure 4.18: Displacement of the cantilever tip with respect to the peak-to-peak voltage input given to the piezoelectric actuator, as recovered from oscilloscope measurement.

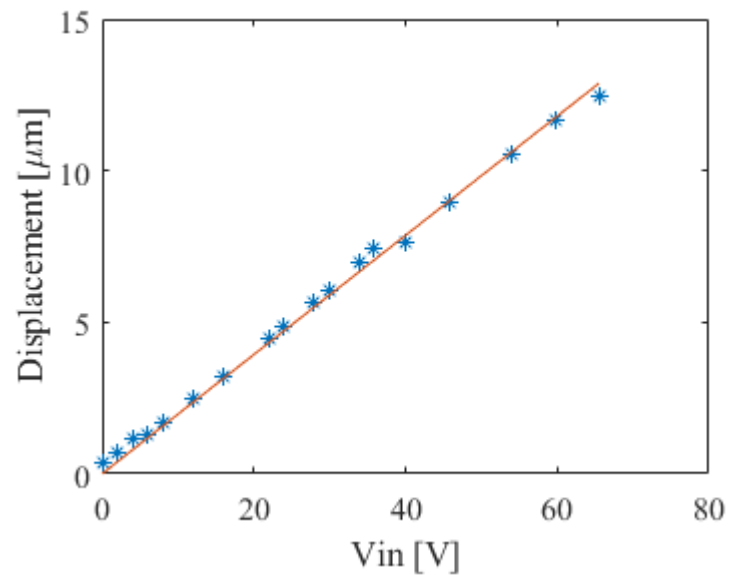


Figure 4.19: Regression line (red) of the displacement behaving linearly with the input voltage.



# Chapter 5

## Design and realization of a resonant switch

In this part of the thesis, we discuss the design and the realization of an optical switch based on the same principle of the modulator. We want to realize a 1x2 resonant switch for 1550 nm wavelength able to periodically alternate light between the two output waveguides. With such device we want to demonstrate that a fast switch ( $> 1$  kHz) can be realized in glass by using femtosecond laser micromachining.

### 5.1 Design of the micro-opto-mechanical device

#### 5.1.1 Design constraints

For the realization of the switch, we want to exploit the oscillation of the cantilever to couple alternately into two separate output waveguides the light that is propagating in the waveguide embedded in the beam. The two waveguides should be placed symmetrically on the two sides of the center of oscillation (Figure 5.1). Of course, a good switch should grant good *port isolation* (PI) and *cross talk* (CT), so that no undesired output are obtained. We recall that for a 1x2 switch, the CT and the PI of a port  $i$  can be defined as:

$$PI_i = -10 \log \left( \frac{P_{min,i}}{P_{max,i}} \right); \quad CT_i = 10 \log \left( \frac{P_j}{P_{max,i}} \right) \quad (5.1)$$

where  $P_{min,i}$ ,  $P_{max,i}$  are the minimum and maximum output power from port  $i$ , while  $P_j$  is the power exiting port  $j$  when the output from  $i$  is at its maximum.

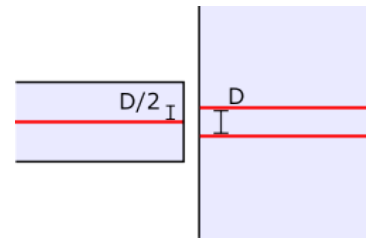


Figure 5.1: Schematic of the cantilever (on the left) and of the waveguides (red lines).

To realize the device and to satisfy these requirements, some considerations must be done on the design constraints:

- **The two output waveguides cannot be placed too far from the center of oscillation.** Indeed, the bigger it is the distance  $D/2$  between one output waveguide and the center of oscillation of the cantilever, the bigger it is the angle at which the cantilever waveguide couples light into that waveguide. We know from Section 1.1.2 that an angle between two waveguides affects negatively the coupling, increasing the coupling losses. Moreover, we must be sure that the cantilever waveguide is able to reach the required oscillation amplitude to conveniently couple the waveguides at a given separation. In any case, the closer are the waveguides, the lower actuation voltage is required on the piezo actuator.
- **We should be conservative on the displacement estimation.** Previous displacement estimation were related to the waveguide mode dimension. Thus, a measurement error during the mode characterization influences all the displacement estimations. Moreover, from the resonant peak analysis we obtained a lower  $Q$  factor than the one needed to reach the displacement measured. Thus, these estimations have a certain degree of uncertainty and it is safer to assume lower values for the maximum possible displacement.
- **The two output waveguides should be separated enough to have low CT.** Indeed, when light is coupled into one of the two waveguides, part of the light exiting the cantilever waveguide could be coupled into the other output. Since we estimate a Gaussian dependence of the coupling with the lateral distance, we should place the two waveguides in such a way that when the waveguide in the cantilever is aligned with one of the output ones, the other is far enough to be on the tail of the Gaussian mode.
- **The two output waveguides should grant a measurable transmitted signal even when the cantilever is at rest position.** This is a more practical constraint related to the coupling with the input fiber. In fact, to best align the input fiber with the input waveguide, the feedback from a power-meter that measures the output is used. If the two output waveguides are too far apart, since no oscillation can be provided before the pig-tail operation, the static coupling between the cantilever waveguide and the output ones will be too poor to enable an observable output when the fiber is not yet perfectly aligned. This will make the first alignment of the fiber very difficult. Therefore, the distance between the waveguides must be chosen so that to grant a measurable output when the cantilever is at rest.

- **The evanescent coupling between waveguides must be considered.** The two output waveguides are close to each other in the initial part, to provide efficient coupling with the light coming from the cantilever, as discussed above. They should then increase their relative distance at the output of the chip, to allow external coupling e.g. with fiber arrays (that typically have fibers  $127 \mu\text{m}$  laterally spaced). Evanescent-field coupling between the two waveguides in the initial part, which may transfer power from one optical mode to the other, should be considered in the design of the device.

### 5.1.2 Quantitative considerations on the waveguides distance

In the following, some of the previous constraints will be quantitatively evaluated to retrieve a range of possible distances  $D$  between the output waveguides, to use in the device design.

- For an approximated evaluation of the losses induced by the tilting angle  $\Delta\theta$  of the cantilever, we used the equation modelled in [20]:

$$L_{angle} = -10 \log \left\{ \exp \left[ - \left( \frac{\pi n \sigma \sin \Delta\theta}{\lambda} \right)^2 \right] \right\} \quad (5.2)$$

where  $n$  is the refractive index of the glass,  $\sigma$  the mode dimension and  $\lambda$  the wavelength.

To evaluate the tilting angle  $\Delta\theta$  of the tip, we can consider an ideal cantilever beam. We have seen that, by using Equation 1.26, it is possible to calculate the displacement  $W_n(x)$  of each point of a cantilever beam of length  $L$  (at coordinate  $x$ ), when the oscillation follows a certain mode  $n$ . By imposing a maximum displacement as the one estimated in the previous chapter  $W_1(L) = 13 \mu\text{m}$  for the first mode of oscillation and by using  $\beta_1 = \pi R_1/L$  (where  $R_1 \sim 0.59686$ ), we can retrieve the constant  $A_1$ :

$$A_1 = \frac{W_1(L)}{(\cosh \pi R_1 - \cos \pi R_1) + \frac{\cos \pi R_1 + \cosh \pi R_1}{\sin \pi R_1 + \sinh \pi R_1} (\sin \pi R_1 - \sinh \pi R_1)}. \quad (5.3)$$

If we now derive Equation 1.26 with respect to  $x$ , we get the tilting angle for every point along the  $x$  axis:

$$\Delta\theta(x) = A_1\beta_1 \left[ (\sinh \beta_1 x + \sin \beta_1 x) + \frac{\cos \pi R_1 + \cosh \pi R_1}{\sin \pi R_1 + \sinh \pi R_1} (\cos \beta_1 x - \cosh \beta_1 x) \right]. \quad (5.4)$$

The tilting angle of the tip of the cantilever is then estimated to be  $\Delta\theta(L) = 0.018$  rad (when a displacement of  $13 \mu\text{m}$  is considered). By introducing this term into Equation 5.2 and considering a mode dimension of  $6.5 \mu\text{m}$ , a wavelength of  $1550 \text{ nm}$  and a refractive index of  $1.5$ , we obtain a loss of  $0.54 \text{ dB}$ . This seems to be quite a small contribution, compared to the loss of about  $6 \text{ dB}$ , measured in our previous device due to the presence of the air gap. Thus, it doesn't seem to be a strong limitation to the range of possible distances.

- From the measurement discussed in Section 4.4 we got two different estimations for the maximum displacement achieved in the oscillation of the cantilever:  $13 \mu\text{m}$  (from the measurement of the modulation depth) and  $7.4 \mu\text{m}$  (from the estimation of the  $Q$  factor). We can assume a conservative estimation of  $10 \mu\text{m}$ , i.e. approximately the average between the two values, as maximum achievable distance, in order to orient the design of our next device.
- A minimum distance  $D$  between the waveguides can be deduced by the third constraint. Indeed, if we assume to have the cantilever waveguide perfectly aligned with one of the two, the light transmitted to the other waveguide can be estimated by  $T_{CT} = \exp(-D^2/\sigma^2)$ . The estimated cross talk is just  $CT = 10 \log T_{CT}$ . If we want to keep a  $CT < -10 \text{ dB}$  ( $T_{CT} < 10 \%$ ) a minimum distance of  $D = 10 \mu\text{m}$  has to be kept for waveguides with mode dimension of  $6.5 \mu\text{m}$ .
- From the fourth constraint we know that a good transmission is needed even at rest position. Since the waveguide should be placed symmetrically on the two sides of the center of oscillation, we can estimate the amount of light coupled into one of the two waveguides when no oscillations are induced by simply  $T_{rest} = \exp(-(D/2)^2/\sigma^2)$ . When  $D/2 = 10 \mu\text{m}$ , as considered from the second constraint, the transmitted light is  $T_{rest} < 10 \%$ , which could be too low for the alignment procedure, so, lower distances should be considered.

These considerations limit to  $10 \div 20 \mu\text{m}$  the range of possible distances  $D$ . In our experiments we will study three distances:  $13$ ,  $15$  and  $17 \mu\text{m}$ .

### 5.1.3 Design choices for managing the evanescent coupling

Since the chosen waveguide distances are comparable to the mode dimension, the evanescent coupling cannot be neglected, as anticipated. We thought about two possible ways to overcome the problem.

One idea was to use two asynchronous waveguides, i.e. two waveguides with different propagation constant. This can be obtained by changing the fabrication parameters, in particular the translation speed during irradiation [99]. In this way, the amount of power that the two waveguides can exchange lowers as the difference in propagation constant increases, as discussed in Section 1.1.3. The drawback of this approach is that such different waveguides may have also a slightly different mode dimension, and this could induce an asymmetry in the output and a reduction of the PI.

Another possibility is to tailor the length of the region in which the waveguides interact by evanescent coupling, in such a way that all the power coupled into a waveguide is transferred to the other and vice versa (cross outputs). To do so, the two waveguides should proceed straight for the chosen length  $L_C$  and then separate with S-bendings to quench the evanescent coupling (Figure 5.2). The drawback of this method is that the length must be finely controlled and that the coupling coefficient between waveguides may experience variations from one fabrication session to the other, due to variability of the laser-pulse characteristics and other features of the irradiation process.

After a careful evaluation, we chose to follow the second approach, which appears more reliable and maintains the previously optimized mode dimension. To meet the requirements of the previous section, an initial separation  $D$  and a final spacing of  $S = 127 \mu\text{m}$  will be considered in the output design, as in Figure 5.2.

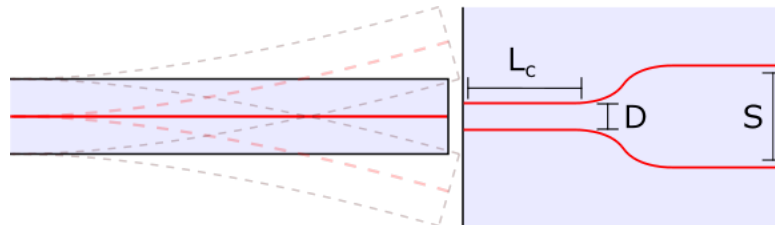


Figure 5.2: Schematic of the two port output design. The two waveguide at a distance  $D$  proceed parallel for the length  $L_c$ , then they separate with the s-bending up to the desired spacing.

### 5.1.4 Expected performance

Assuming now a perfect compensation of the evanescent coupling, we can model the two port output in the three cases of 13, 15 and 17  $\mu\text{m}$  spacing when a mode dimension  $\sigma = 6.5 \mu\text{m}$  is considered. Table 5.1 reports some critical values, estimated with the formulas presented in Section 5.1.2, in the three cases (for the PI an oscillation amplitude of  $d_{max} = D/2$  has been considered in  $PI = 10 \log(\exp(d_{max}^2/\sigma^2))$ ). The transmission at rest position from a single port  $T_{rest}$  reduces a lot by increasing the spacing between the waveguides. This is the main reason for which in future experiments we chose to focus on 13 and 15  $\mu\text{m}$ . The losses induced by the tilting angle are comparable and don't seem to add a considerable contribution to the total losses. When we consider an oscillation that brings the waveguide in the cantilever to be exactly aligned with one of the output waveguides, which is the best working condition for an alternate output, the PI and the CT should have the same absolute value from our model. Values comparable with the maximum ER measured in the optimized modulator of Section 4.4 are modelled, thus we can be satisfied with the choice of the distances.

$D$	$T_{rest}$	CT[dB]	$L_{angle}$ [dB]	PI[dB]
13 $\mu\text{m}$	36.8%	-17	0.14	17
15 $\mu\text{m}$	26.4%	-23	0.18	23
17 $\mu\text{m}$	18.1%	-29	0.23	29

Table 5.1: Predicted values of some parameters discussed during the quantitative analysis of the constraints. The PI has been calculated in the case of an oscillation with amplitude  $D/2$ .  $T_{rest}$ : transmission from a single port at rest position; CT: cross talk;  $L_{angle}$ : losses induced by the coupling angle between the cantilever and the output waveguide; PI: port isolation.

We can treat each waveguide as in the model of Section 4.3.1 by considering a distance of  $D/2$  between the center of oscillation and the waveguide. In this way, we can simulate the behaviour of the two outputs in the different condition.

Figure 5.3 reports the simulation of the output when a distance  $D = 15 \mu\text{m}$  is considered. The maximum displacement of the cantilever assumes the value of 4.5, 7.5 and 10.5  $\mu\text{m}$  in the three cases. As can be seen, when the displacement is bigger than half the separation, two peaks are seen in each output, which is not useful for the desired switching behaviour. We will use this model to asses the performance of the final device.

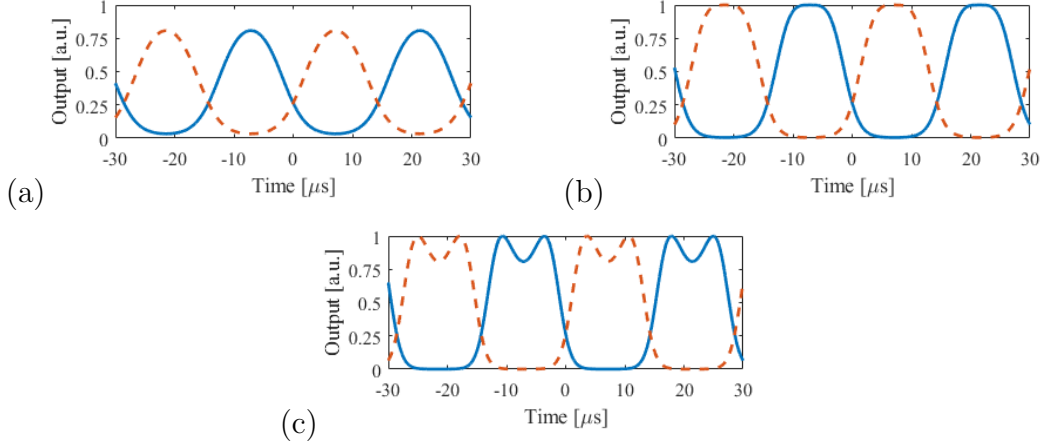


Figure 5.3: Simulation of the output from port one (blue line) and two (red dashed line) when they are separated by  $D = 15 \mu\text{m}$ . The cantilever oscillates at 35 kHz with a maximum displacement of  $4.5 \mu\text{m}$  (a),  $7.5 \mu\text{m}$  (b) and  $10.5 \mu\text{m}$  (c).

## 5.2 Optimization of design parameters

### 5.2.1 Choice of the radius of curvature

The chosen design include S-bent waveguide segments, which may introduce further optical loss (i.e. bending loss). To estimate the amount of losses introduced and to chose a proper radius of curvature  $R$  to use, one dedicated sample was fabricated as described in Section 3.3.4. In particular, 6 radii of curvature were tested, ranging from 40 to 90 mm. For each radius of curvature two waveguides were fabricated. The sample was 2.5 cm long and the S-bent part was 2 cm long in each waveguide

The results of the characterization are reported in Figure 5.4: losses reduce dramatically when the radius of curvature is increased.

In our device, the separation distance of the initial ( $D$ ) and final ( $S$ ) part of the waveguide is fixed by design. We should consider that, if a larger radius of curvature is used, the length of the bent part required to reach a certain waveguide separation becomes longer. The optimum radius of curvature must provide the minimum overall loss, taking into account the required length for the bent segment.

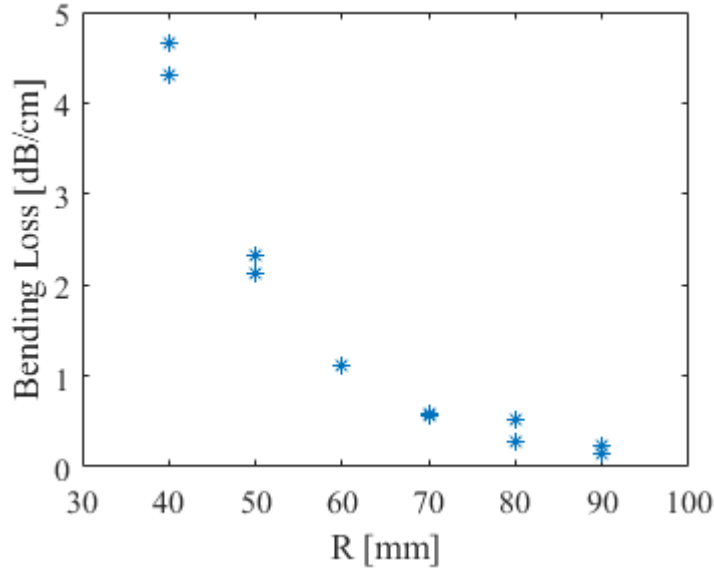


Figure 5.4: Measured bending loss as function of the radius of curvature.

The length of the bent part  $l_b$  can be simply calculated from  $D$ ,  $S$  and  $R$ . As can be seen in Figure 5.5,  $a = (S - D)/4$  so that the angle subtended by each of the two arcs is  $\theta = \arccos(1 - a/R)$ . The length of the bent part is just  $l_b = 2R\theta$ .

From this we observe that the dependence of the length of the bent part from the radius of curvature is less than linear while the losses follow an exponential behaviour. Thus, a minimum is expected at high radii of curvature. In the range of radii we tested, the overall losses due to the bending reduced while increasing the radius. Since we don't have particular constraints on the dimension of the final device, we chose a radius of curvature  $R = 90$  mm.

The estimated contribution to the total losses is about 0.1 dB for all three initial distances  $D$ .

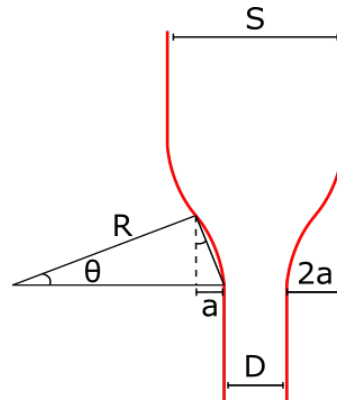


Figure 5.5: Schematic of the two bent waveguides (red lines) in the device with the discussed dimensions.

### 5.2.2 Determination of the coupling length

To choose the interaction length  $L_C$  for our device, we first need to determine the coupling coefficient  $k$  between the two waveguides in the three cases considered ( $D = 13, 15$  and  $17 \mu\text{m}$ ).

We fabricated a first chip with 9 directional couplers for each interaction distance  $D$ . The 9 couplers had interaction length  $L_C$  ranging from 0.2 to 1.6 mm with regular steps of 0.2 mm.

Figure 5.6 presents the measured splitting ratio  $T = P_{cross}/(P_{cross} + P_{bar})$  in the three sets for vertically polarized input light. In the graph it is shown also the fitting curve  $\sin^2(kL_C + \phi_0)$  used to obtain  $k$  and  $\phi_0$ . The results are shown in Table 5.2. The predicted interaction length  $L_B$  at which light makes a full transfer cycle is also reported. Namely, light entering from one input port is entirely transferred to the other waveguide within the coupler, and then transferred back again on the initial waveguide so that it exits from the bar port. The total phase term  $kL_C + \phi_0$  have a linear dependence with the coupling length, thus the standard deviation from a linear regression is also shown in the table, which will be useful later during an error analysis.

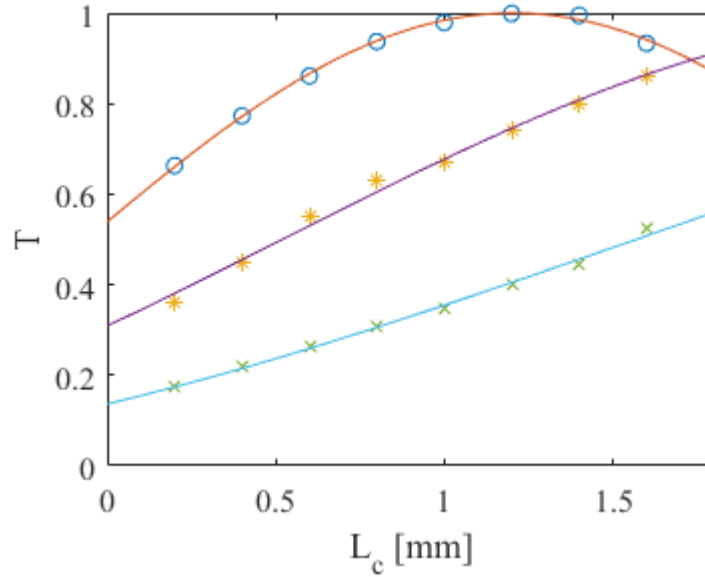


Figure 5.6: Splitting ratio measured (dots) and fitted (lines) for the three sets of couplers with interaction distance  $13 \mu\text{m}$  (o),  $15 \mu\text{m}$  (\*) and  $17 \mu\text{m}$  (x).

The length  $L_B$  is important for our design, because the structure we will use in our device can be assimilated to half of a coupler, as shown in Figure 5.7. Thus, if the complete coupler has an interaction length  $L_B$  and an initial phase term  $\phi_0$  so that  $kL_B + \phi_0 = \pi$ , a device made by half of such coupler will have an interaction length  $L_C = L_B/2$  and a phase  $\varphi_0 = \phi_0/2$ . In these conditions the

$D$	$k[\text{mm}^{-1}]$	$\phi_0[\text{rad}]$	$L_B[\text{mm}]$	St.Dev[rad]
13 $\mu\text{m}$	0.62	0.82	3.74	0.019
15 $\mu\text{m}$	0.38	0.59	6.77	0.016
17 $\mu\text{m}$	0.26	0.38	10.66	0.008

Table 5.2: Parameters obtained from the fit of the measured splitting ratios. The standard deviation is retrieved from a linear regression of the total phase term  $kL_C + \phi_0$ .

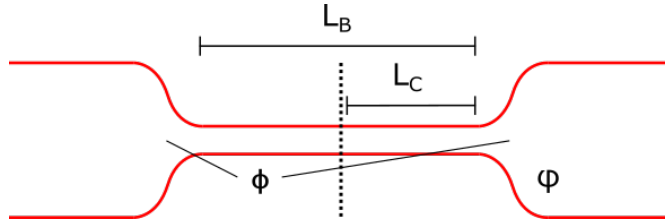


Figure 5.7: Schematic representation of the complete coupler and of its half (structure used in the device). The two different coupling lengths and the contribution of the bent parts to the total phase in both cases are indicated.

input light will be fully transferred to the cross output port, which is our desired design  $kL_C + \varphi_0 = \pi/2$ .

To improve the estimation of  $L_B$  and to check the repeatability of the fabrication process, we fabricated another sample with two sets of 14 couplers. This time only interaction distances of 13 and 15  $\mu\text{m}$  were analysed, as anticipated in Section 5.1.4. Interaction lengths around  $L_B$  were explored. For  $D = 13 \mu\text{m}$  we chose to fabricate couplers with lengths between 2.6 and 4.4 mm, with a shorter step than before (0.15 mm). For  $D = 15 \mu\text{m}$  instead we fabricated couplers with lengths ranging from 5.1 and 7.5 mm with a step of 0.2 mm. The splitting ratios obtained with vertically polarized input light are reported in Figure 5.8, together with best-fit curves. In Table 5.3 the new obtained values are reported; the percentage difference with the ones previously obtained is indicated in the parentheses. The two samples presented similar coupling coefficients and similar phase terms, with a percentage difference  $< 4 \%$ . Also the estimated interaction lengths  $L_B$ , from the two samples, are in good agreement with each other (difference  $< 4 \%$ ).

$D$	$k[\text{mm}^{-1}]$	$\phi_0[\text{rad}]$	$L_B[\text{mm}]$	St.Dev[rad]
13 $\mu\text{m}$	0.61(-1.78%)	0.85(3.59%)	3.76(0.51%)	0.029
15 $\mu\text{m}$	0.36(-3.61%)	0.59(-0.68%)	7.03(3.89%)	0.033

Table 5.3: Parameters obtained from the fit of the measured splitting ratios. The percentage difference with the previous ones is indicated in the parentheses.

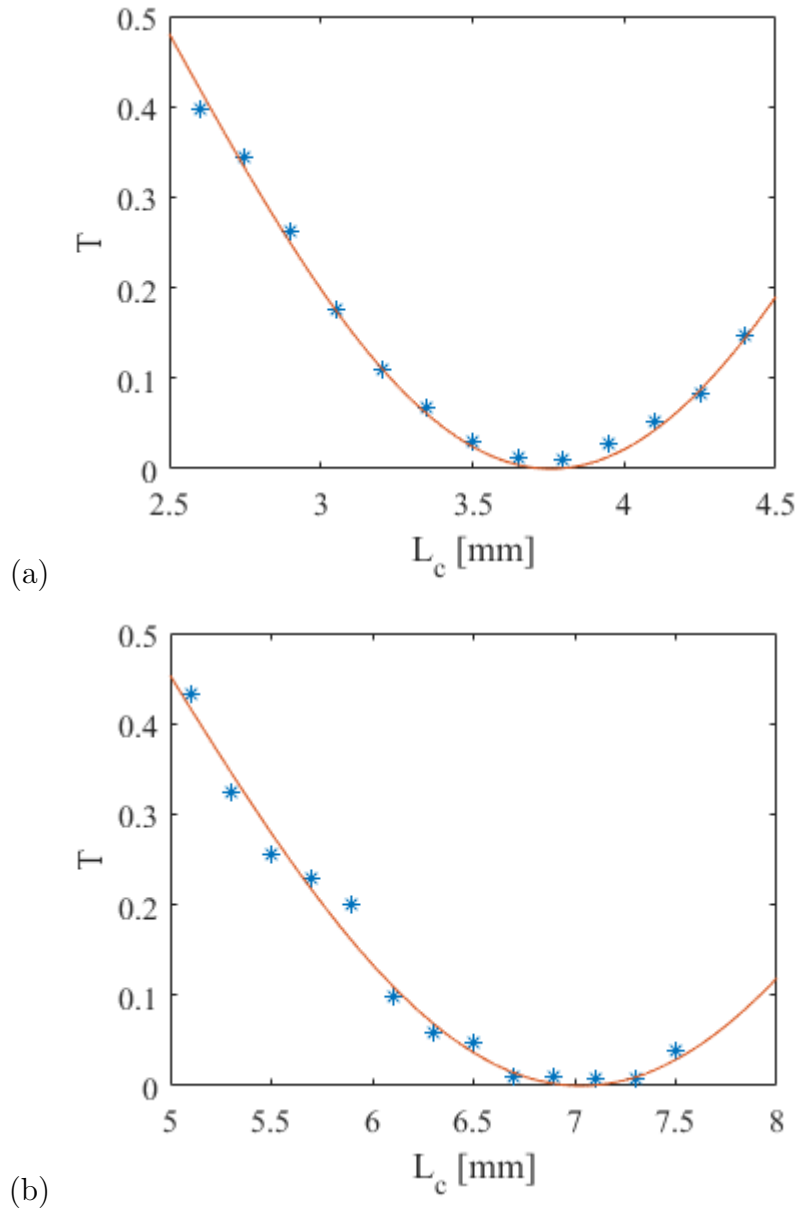


Figure 5.8: Splitting ratios measured from the 14 couplers when the coupling distance was  $13 \mu\text{m}$  (a) and  $15 \mu\text{m}$  (b). The least square fit is also shown in the graphs.

On the basis of these measurements, we chose the design parameters for our devices:  $L_C = 1.88$  mm for  $D = 13$   $\mu\text{m}$  and  $L_C = 3.45$  mm for  $D = 15$   $\mu\text{m}$ .

We can now discuss some other possible sources of error. The device, which is assimilated to a half-coupler, would have a cross output  $\sin^2(kL_c + \varphi) = 1$  in perfect conditions. However, some variation in the parameters can occur, because of fabrication tolerances, therefore we should consider  $\sin^2((k + \Delta k)(L_C + \Delta L) + (\varphi + \Delta\varphi))$  and compare it to the desired condition.

- Assuming  $\Delta k = 0$  and  $\Delta\varphi = 0$ , the only source of error is the length. A possible variation of the length could be due to the tolerances in the ablation process of the wall in front of the cantilever tip. This indeed determines the initial point of the coupler. Assuming a variation of  $\Delta L = \pm 5$   $\mu\text{m}$  we would obtain for 13 and 15  $\mu\text{m}$  distance an error of  $1.2 \cdot 10^{-5}$  and  $8.3 \cdot 10^{-5}$  respectively.
- Assuming instead  $\Delta L = 0$  and  $\Delta\varphi = 0$ , we can consider the percentage difference between  $k$  in different fabrications as the source of error (4 %). In this case the error would be of  $2.1 \cdot 10^{-3}$  and  $1.1 \cdot 10^{-4}$ .
- If we instead consider the case of  $\Delta k = 0$  and  $\Delta L = 0$ , the difference in  $\varphi$  between fabrications should give an error of  $3.1 \cdot 10^{-4}$  and of  $4.2 \cdot 10^{-4}$ .
- The standard deviation of the total phase can be considered, since it is a measure of the quality of our estimations and of the measurements done. In this case, considering the standard deviations of the last sample, we would have an error of  $8.7 \cdot 10^{-4}$  and  $4.9 \cdot 10^{-4}$ .

Finally, the same sample has been characterized with horizontally polarized input light. This was done in order to estimate the robustness of our device with respect to the polarization of the input. Indeed, in the final configuration, the input will be brought by an optical fiber, which induces a random transformation on the input polarization. The retrieved coefficients for horizontal polarization are presented in Table 5.4. When the input of the final device is horizontally polarized, the expected output will be  $\sin^2(k_H L_C + \varphi_H)$ , where  $\varphi_H = \phi_H/2$ . Since  $L_C$  has been optimized for vertical polarization, in the two cases of  $D = 13$  and 15  $\mu\text{m}$ , errors of 2 % and 3 % are expected respectively, predicting a good robustness to input polarization.

$D$	$k_H[\text{mm}^{-1}]$	$\phi_H[\text{rad}]$	$L_B[\text{mm}]$	St.Dev[rad]
13 $\mu\text{m}$	0.65	0.98	3.32	0.029
15 $\mu\text{m}$	0.40	0.71	6.04	0.051

Table 5.4: Parameters obtained from the fit of the measured splitting ratios when entering with horizontal polarization

### 5.2.3 Shutter synchronization

In the modulator device, described in Chapter 4, the waveguide segment within the cantilever and the waveguide segment at the output were inscribed by means of a single laser scan. In this device, instead, the waveguide in the cantilever is supposed to end at the cantilever tip, while the two output waveguides should begin at the following glass surface.

In the fabrication setup, a mechanical shutter is used to select the time window in which the laser pulses are delivered to the sample. The time required for the shutter to open and close can determine a delay at the beginning and at the end of a waveguide. Depending on the writing speed, this can result into a shift in the position of the extremities of the waveguide.

The spacing between the cantilever tip and the following glass surface is about  $10\ \mu\text{m}$ , so we want the waveguides respectively to end and begin in that space with a micrometric precision.

To determine the opening and the closing time of the shutter, a set of 9 parallel tracks were laser-written with different speeds into a glass sample. All the inscribed tracks begin and end well within the glass sample; in this way, it is possible to measure their initial and final position. The nominal initial and final position were the same for all the tracks. One track was written with extremely low writing speed ( $0.1\ \text{mm/s}$ ) to be used as a reference. The other 8 tracks were written with  $1, 5, 10, 15, 20, 25, 30$  and  $35\ \text{mm/s}$  speed. We expect the waveguides written with higher speed to start (and end) with a spacial delay proportional to that time.

After the fabrication, a microscope analysis was carried out. For what concerns the opening time of the shutter, the initial position of the waveguides was measured from the beginning of the  $0.1\ \text{mm/s}$  waveguide (Figure 5.9). Then a linear regression was performed to extrapolate the time delay. A time delay of  $2.0\ \text{ms}$  was found. For the closing time, an analogous approach has been used (Figure 5.9). In this case a delay of  $1.7\ \text{ms}$  was estimated.

Since the writing speed of our waveguides is  $10\ \text{mm/s}$ , we have to set the end position of the cantilever waveguide and the beginning position of the two output waveguides respectively  $17\ \mu\text{m}$  and  $20\ \mu\text{m}$  in advance with respect to their design position.

### 5.2.4 Fabrication of preliminary structures

Before fabricating a complete device, simpler structures were used to estimate experimentally the optical transmission from the waveguide in the cantilever to the output ones, when the first one is centered with respect to the other two, simulating the condition of a cantilever at rest.

Two different kind of structures were fabricated. *Structure 1* consisted in a straight waveguide ending in the glass and followed, at a distance of  $10\ \mu\text{m}$ , by

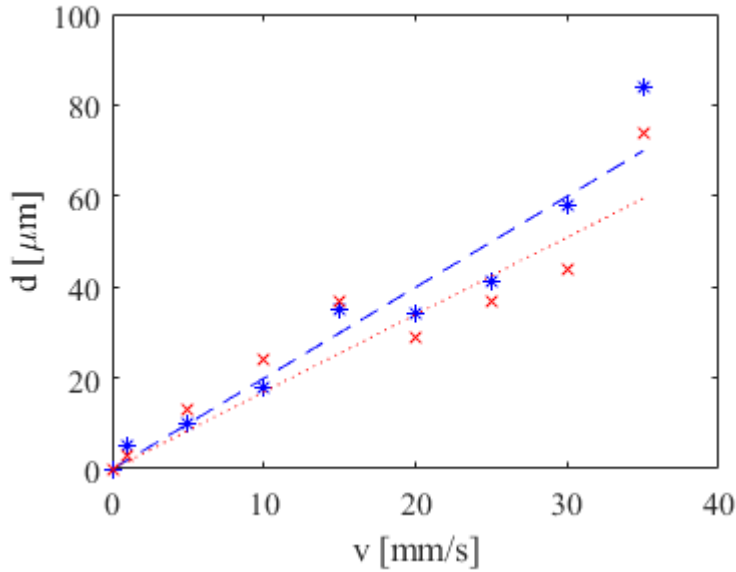


Figure 5.9: Measured distances of the initial (blue stars) and final (red cross) point of each waveguide from the corresponding point of the reference one (0.1 mm/s) due to the opening and closing time of the shutter. The regression line is also shown for the initial (blue dashed line) and final (red dotted line) distances.

other two output waveguides disposed as the half-coupler discussed in Section 5.2.2 (Figure 5.10 (a)). *Structure 2* presented the same waveguide configuration, but had a 10  $\mu\text{m}$  air spacing between the first straight waveguide and the two output waveguides (Figure 5.10 (b)). Both structures were realized with a separation of the output waveguides  $D = 13$  and 15  $\mu\text{m}$ . Figure 5.11 shows a microscope picture of the two structures in the case of  $D = 15 \mu\text{m}$ . Three copies of each structure were realized to evaluate also the variability within a single fabrication.

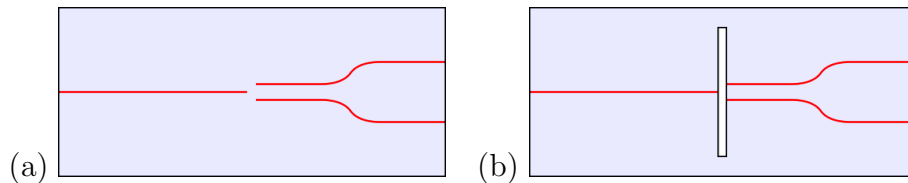


Figure 5.10: Schematic of Structure 1 (a) and Structure 2 (b) where the red lines are waveguides and the central black rectangle in (b) is the air spacing.



Figure 5.11: Microscope image of Structure 1 (left) and structure 2 (right) at the interface between the waveguides when the separation between the output waveguides is  $D = 15 \mu\text{m}$ .

The transmission of the two output waveguides were measured and compared to what we expected by previous estimation ( $T_{rest} = 36.8 \%$  and  $26.4 \%$  respectively for  $D = 13 \mu\text{m}$  and  $15 \mu\text{m}$ , which correspond to a loss of 4.3 and 5.8 dB for each waveguide). Table 5.5 presents the retrieved losses due to the interface between the straight waveguide and the two output ones, together with the losses predicted with the model (the IL from a reference straight waveguide have been subtracted to extrapolate the contribution of the interface only). Note that we are considering the sum of the two output powers, thus the total modelled loss considered is 3 dB lower than the one of a single waveguide.

$D[\mu\text{m}]$	$L_{model}[\text{dB}]$	$L_{glass}[\text{dB}]$	St.Dev.[dB]	$L_{air}[\text{dB}]$	St.Dev.[dB]
13	1.3	2.1	0.1	11.6	3.2
15	2.8	3.0	0.2	13.0	2.1

Table 5.5: Measured losses, considering the sum of the contributions of both outputs. The IL of a reference straight waveguide has been subtracted to retrieve just the contribution of the interface.  $L_{model}$ : expected losses from the model;  $L_{glass}$ : losses due to the glass interface in Structure 1;  $L_{air}$ : losses due to the air interface in Structure 2.

Structure 1 presents similar losses ( $L_{glass}$ ) to the one predicted, with a low standard deviation. Structure 2 presents higher losses ( $L_{air}$ ) and high variability within the set of identical structures. The increase in the losses due to the air spacing seems to be higher than the 6 dB loss observed in the previous device. Moreover, as it was observed by using a vertically polarized input (the one for which the coupler has been tailored), the output power from the two waveguides was unbalanced, being in all cases about 65 % onto the first output waveguide and

35 % onto the second one. To check whether this fact was due to an error in the transverse position of the waveguides, we tried to estimate for each output waveguide  $i$  the lateral distance  $x_i$  from the input one that induced such unbalancing of the output. If we indicate with  $R = P_1/P_2 = 65/35$  the ratio between the power exiting the two outputs, by considering  $D = 13$  and  $15 \mu\text{m}$  and a mode dimension of  $\sigma = 6.5 \mu\text{m}$ , we can write:

$$\begin{cases} x_1 + x_2 = D \\ e^{-\frac{(x_1-x_2)^2}{\sigma^2}} = R \end{cases} \quad (5.5)$$

Then we can recover the two distances from:

$$\begin{cases} x_2 = \frac{D}{2} - \frac{\sigma}{2}\sqrt{\ln R} \\ x_1 = \frac{D}{2} + \frac{\sigma}{2}\sqrt{\ln R} \end{cases} \quad (5.6)$$

For  $D = 13 \mu\text{m}$  we get  $x_1 = 9 \mu\text{m}$  and  $x_2 = 4 \mu\text{m}$ , while for  $D = 15 \mu\text{m}$  we get  $x_1 = 10 \mu\text{m}$  and  $x_2 = 5 \mu\text{m}$  (note that when writing the equation we took into account that the power is perfectly exchanged between the waveguides due to the coupling). By carefully looking at the structures with the microscope, no such asymmetry can be observed, thus we exclude that this is the cause of the problem. We didn't have the means to do a more accurate study at that point, so we chose to proceed with the fabrication of a complete device to check if the problem might occur again.

### 5.3 Fabrication and characterisation of the switch

Two complete devices were realized, with output waveguides initially separated by  $D = 13 \mu\text{m}$  and  $D = 15 \mu\text{m}$  respectively. The two devices were realized within the same fabrication session. For each device, the central input waveguide was inscribed with a first laser scan, then the two output waveguides were fabricated starting  $10 \mu\text{m}$  after the ending of the first as in Section 5.2.4. For the correct positioning of the final and initial part of the waveguides, closing and opening times of 1.7 and 2.0 ms were considered for the mechanical shutter. The two output waveguides were centered with respect to the input one and were initially separated by a distance  $D$ . The two waveguides proceeded straight for the interaction length  $L_C$  ( $1.88 \mu\text{m}$  and  $3.45 \mu\text{m}$  in the two cases), then were separated by S-bends with  $90 \text{ mm}$  radius of curvature in order to reach the final spacing of  $127 \mu\text{m}$  at the output facet of the chip. The cantilever was ablated after the fabrication of the waveguides.

**Device with 13  $\mu\text{m}$  spacing** Measuring the IL of every output and subtracting the ones of a reference straight waveguide, we retrieved the losses induced by the air spacing when the cantilever was at rest position. Similarly to what observed for Structure 2 in Section 5.2.4, we obtained a loss of  $L_{air} = 9.9$  dB, considering the sum of the two outputs. The two outputs were only slightly unbalanced, with the power exiting the first output being 53 % of the total.

After this first observation, a dynamic characterization was carried out. While our device was designed to work with vertically polarized input, we should note that the input light comes from a single mode fiber that induces a random transformation on the polarization. In this first experiment we chose not to perform any polarization compensation; as discussed in Section 5.2.2, we believe in fact that it would minimally affect the output distribution (in the order of 1 %).

First, we characterized the natural oscillation modes with a procedure similar to the one adopted for the other cantilever devices (i.e. by observing non-negligible modulations on the output signals while sweeping the frequency of the piezoelectric actuation). Then, setting the excitation frequency at the first resonance ( $f_1 = 36.0$  kHz) we acquired the signal at the two outputs, for a set of different actuation voltages.

Figure 5.12 shows the outputs measured from the oscilloscope when 12, 30 and 60 V peak-to-peak are applied onto the piezoelectric actuator. As can be observed, by increasing the actuation voltage, the contrast between peaks and valleys of the signal in each port increases. The maximum output of each port saturates at actuation voltage around 30 V and when such actuation voltage is increased further, a second peak appears, indicating that the oscillation of the cantilever has an amplitude higher than the distance at which the waveguides are placed ( $D/2$ ). It can be observed that output 1 (blue line), which had an higher power during the static characterization, is progressively surpassed by output 2 (red dashed line). To understand the reason of such unexpected behaviour further studies should be carried out.

We want now to underline that 30 V peak-to-peak was the highest voltage at which only one peak was visible, thus we can consider it as the best actuation voltage for our switch. Indeed, for an ideal behaviour, we would like to have the perfect alternation of peaks between the two outputs. A large peak can also be a good feature, in certain applications, since it can grant a long time for the data to be transmitted. For this reason the following analysis on the PI, on the CT and on the IL will be carried out at this voltage.

For what concerns the PI, for each port the ratio between a peak and the adjacent valley was measured. The CT was estimated from the ratio between the peak measured at one port and the valley measured on the other.

To retrieve the IL of the device, at each port, we had to convert the output of the photodetector, which is a voltage signal, into an actual power measurement. To do so, the output of each port was measured also with a power-meter to retrieve the mean power. The average of the photodiode signal, within an oscillation

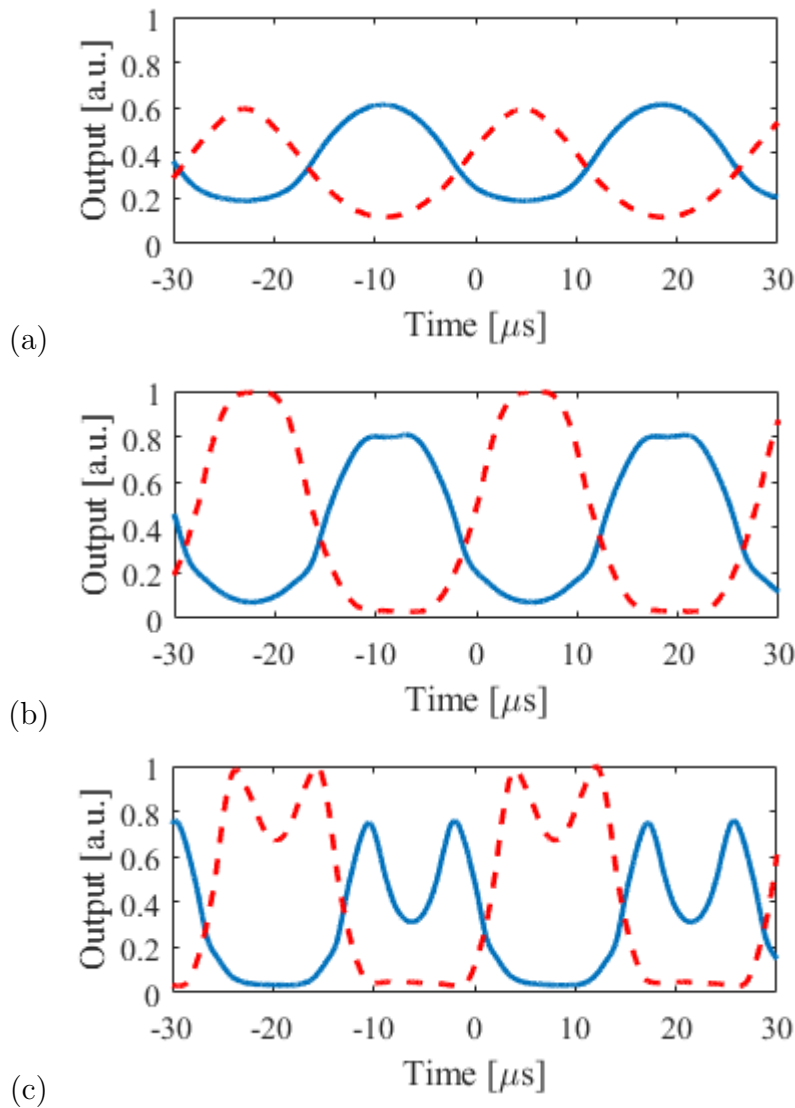


Figure 5.12: Measurements of the output from waveguide 1 (blue line) and 2 (red dashed line) of the  $D = 13 \mu\text{m}$  device when 12 V (a), 30 V (b) and 60 V (c) peak-to-peak are applied onto the piezoelectric actuator. The outputs have been normalized to the maximum voltage measured.

cycle, was evaluated numerically; this average voltage corresponds to the measured mean power and allows to retrieve the proportionality constant between the two quantities.

Table 5.6 reports the values estimated after this analysis. As observed in Section 5.1.4, the PI and the CT assume comparable absolute values. A PI of 10 dB corresponds to a modulation depth of 90 % on that port, thus we can be satisfied with this result. The overall CT is in the order expected for this device (we estimated a CT of -17 dB ideally). Unfortunately the IL of the two ports are quite high if compared to the 8 dB of the modulator of Chapter 4.

	PI[dB]	CT[dB]	IL[dB]
Output 1	10.3	-13.1	11.7
Output 2	14.1	-11.4	10.4

Table 5.6: Relevant quantities measured from the switch at 30 V peak-to-peak actuation.

**Device with 15  $\mu\text{m}$  spacing** A static characterization of the outputs with the cantilever at rest position was carried out also on this device, providing a loss of  $L_{air} = 10.0$  dB and the two outputs exhibit an unbalancing of 62 % in favor of the first output.

The dynamic characterization was carried out in the same way as done for the  $D = 13$   $\mu\text{m}$  device. The resonance frequency for this device was found to be 36.2 kHz.

Figure 5.13 presents the output measured when actuation voltages of 16, 70 and 120 V peak-to-peak are applied. The overall dynamics is similar to the one observed for the other device: increasing the actuation voltage enhance the contrast of the modulation up to a saturation point. Further increase of the actuation voltage brings to the appearance of double peaks. This time, output 1, which presented an higher power during the static characterization, maintains a higher peak value also for higher actuation voltages (differently to what observed in the other device).

The ideal working point for the device corresponds to 70 V peak-to-peak of actuation, since the double peak is not yet visible and so the two peaks alternate regularly. In this condition the PI, the CT and the IL of each port have been characterized. The results are summarized in Table 5.7. The PI on each port is higher than 10 dB and presents values comparable to the previous device. Port one presents a good CT, comparable to the previous ones. The CT on the second port, on the other hand, is quite low, probably due to the very high losses. Thus, the improvement in PI and CT for using a higher separation  $D$  predicted in Section 5.1.4 was not confirmed. The overall IL are higher than the  $D = 13$   $\mu\text{m}$  device.

	PI[dB]	CT[dB]	IL[dB]
Output 1	11.0	-14.4	13.6
Output 2	11.7	-8.4	14.7

Table 5.7: Relevant quantities measured from the switch at 70 V peak-to-peak actuation.

**Measurements with vertically polarized input light** In the measurement discussed up to now, the polarization used was fixed but randomized due to the effect of the optical fiber.

We then investigated whether any enhancement in the performance of the device was reachable when a pure vertically-polarized input state was used. To compensate for the transformation induced by the optical fiber, a half-waveplate and a quarter-waveplate were placed before the optical fiber. By placing a horizontal polarizer after one of the two outputs, we iteratively rotate the two waveplates to minimize the exiting light, so that to obtain a vertically polarized output. Then we removed the polarizer and proceed with the measurements.

We measured each output at the working condition of each device (30 V peak-to-peak input for  $D = 13 \mu\text{m}$  and 70 V for  $D = 15 \mu\text{m}$ ). Values of PI and CT comparable to what previously observed were obtained in both cases, confirming the robustness of the device with respect to polarization, as predicted in Section 5.2.2.

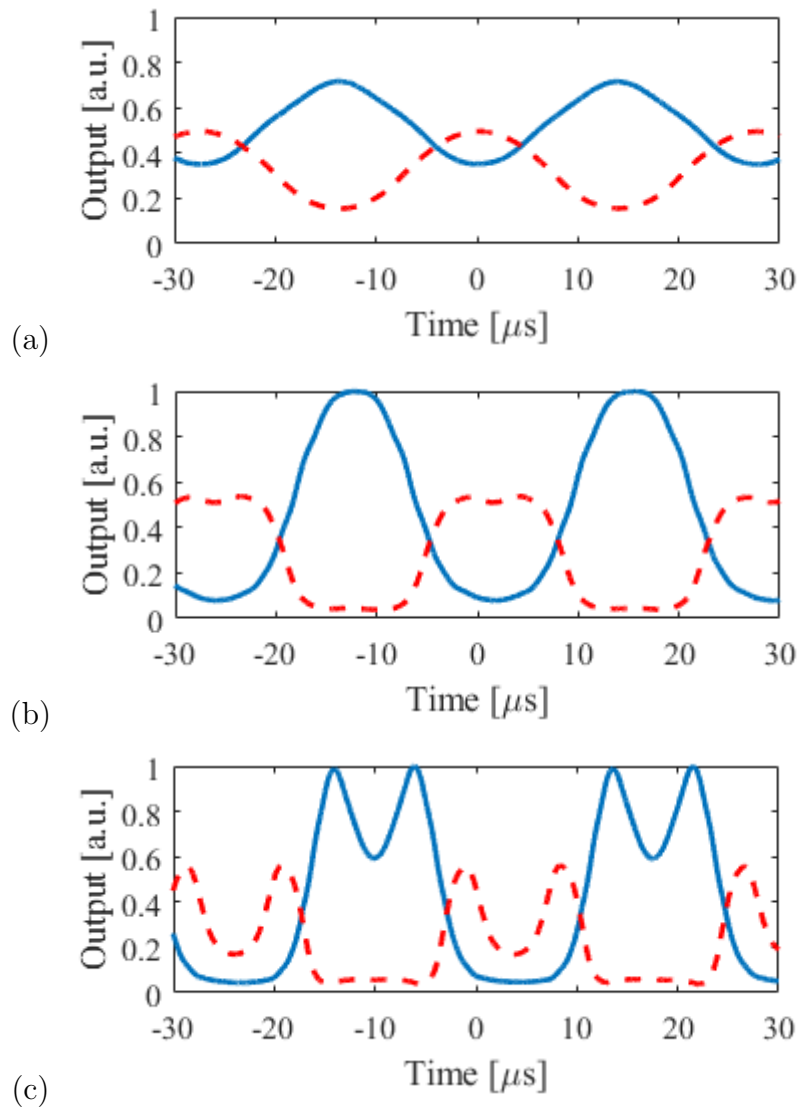


Figure 5.13: Measurements of the output from waveguide 1 (blue line) and 2 (red dashed line) of the  $D = 15 \mu\text{m}$  device when 16 V (a), 70 V (b) and 120 V (c) peak-to-peak are applied onto the piezoelectric actuator. The outputs have been normalized to the maximum voltage measured.



# Conclusions

We have demonstrated an integrated intensity modulator and an optical switch, entirely fabricated by femtosecond laser micromachining.

The two devices were realized in a borosilicate glass substrate by the combination of direct waveguide writing and water assisted femtosecond laser ablation. In both cases, the oscillation of a micro-cantilever structure, containing an embedded waveguide, was used to modulate light transmission towards the output waveguides.

The intensity modulator was developed on the basis of a previous project. In this work, in particular, we have improved the modulation capabilities, increased the modulation frequency and regularized the peak distribution of such device. To improve the modulation contrast, a waveguide with a smaller mode dimension was developed. The length of the cantilever was also reduced from 1.2 to 1 mm, increasing the resonant frequency from 24 to 36 kHz. A method to analyse and evaluate the asymmetry in the temporal distribution of the peaks was developed. We proceeded then with the correction of the fabrication method, which was causing asymmetry in the mechanical oscillations and thus in the peak distribution. Thanks to these improvements, we were able to increase the ER from 0.4 dB (9 % modulation) to more than 17 dB (98 % modulation), with modulation peaks alternating at a frequency of 72 kHz with an asymmetry of just 1.5 %.

The good performances granted by the modulator enabled the design of the resonant 1x2 micro-opto-mechanical switch. An analysis of the constraints imposed by the previous device was done to choose the best geometry for the output waveguides and to predict the output performances. Two devices able to periodically alternate light into the two output ports with frequency 72 kHz were realized. The best device presented  $PI > 10$  dB and  $CT < -11$  dB, with switching times  $< 10 \mu s$  (time to pass from 10 to 90 % of the signal).

These micro-opto-mechanical modulators and switches constitutes a novelty in the field of glass-based integrated-optics devices, where thermo-optic phase modulation is usually employed. In particular, they allow to overcome the limitations of response time typical of thermo-optic actuation. The PI and CT of our devices are comparable to the state of the art of other MOEMS.

Even though the resonant behaviour prevents our device from being used in common telecommunication applications, which often require bi-stable switches, our

device is suitable for glass based optical sensing. For example, the micro-opto-mechanical switch could be used to deliver coordinated light pulses into two different region of a sample. By inverting the input with the outputs, this device could also be adapted to act as an encoder to mix two wavelengths into one alternate signal (after a proper tailoring of the waveguides and of the interaction length), which could be useful, for example, in fluorescence analysis. Moreover, the possibility of fabricating multiple devices with different resonance frequencies opens the way to the realization of an integrated spectrum analyzer for mechanical oscillation, providing that oscillation of the order of 100 nm can be measured and that this could be increased by the optimization of the two output waveguides position.

Currently, both the modulator and the switch presented quite high IL ( $> 8$  dB). We think that this could be due to the roughness of the surfaces between the waveguide in the cantilever and the output ones, thus a profilometer analysis could be carried out to obtain information on how to improve the devices. Another problem encountered is the unbalancing between the two outputs of the switch, which will require further work and optimization to be solved.

# Bibliography

- [1] Robert G. Hunsperger. *Integrated Optics; Theory and Technology*. Springer.
- [2] M. Stepanovsky. A comparative review of mems-based optical cross-connects for all-optical networks from the past to the present day. *IEEE Communications Surveys Tutorials*, 21(3):2928–2946, thirdquarter 2019.
- [3] M. Hoffmann, D. Nusse, and E. Voges. An electrostatically actuated 1 x 2 moving-fiber switch. *IEEE Photonics Technology Letters*, 15(1):39–41, Jan 2003.
- [4] M. . M. Lee and M. C. Wu. Mem-actuated microdisk resonators with variable power coupling ratios. *IEEE Photonics Technology Letters*, 17(5):1034–1036, May 2005.
- [5] Yuta Akihama and Kazuhiro Hane. Single and multiple optical switches that use freestanding silicon nanowire waveguide couplers. *Light: Science and Applications*, 1(e16), June 2012.
- [6] Michele Spagnolo. A micro-optomechanical modulator realized by femtosecond laser micromachining. Master’s thesis, Politecnico di Milano, 4 2019.
- [7] M. Ams, G. D. Marshall, P. Dekker, M. Dubov, V. K. Mezentsev, I. Bennion, and M. J. Withford. Investigation of ultrafast laser–photonic material interactions: Challenges for directly written glass photonics. *IEEE Journal of Selected Topics in Quantum Electronics*, 14(5):1370–1381, Sep. 2008.
- [8] M. H. Niemz. Threshold dependence of laser-induced optical breakdown on pulse duration. *Applied Physics Letters*, 66(10):1181–1183, 1995.
- [9] C. Hnatovsky, R. S. Taylor, P. P. Rajeev, E. Simova, V. R. Bhardwaj, D. M. Rayner, and P. B. Corkum. Pulse duration dependence of femtosecond-laser-fabricated nanogratings in fused silica. *Applied Physics Letters*, 87(1):014104, 2005.
- [10] Shane M. Eaton, Haibin Zhang, Peter R. Herman, Fumiyo Yoshino, Lawrence Shah, James Bovatsek, and Alan Y. Arai. Heat accumulation effects in fem-

- tosecond laser-written waveguides with variable repetition rate. *Opt. Express*, 13(12):4708–4716, Jun 2005.
- [11] Giulio Cerullo Shane M. Eaton and Roberto Osellame. Fundamentals of femtosecond laser modification of bulk dielectrics. pages 3–18.
- [12] C. Hnatovsky, R.S. Taylor, E. Simova, P.P. Rajeev, D.M. Rayner, V.R. Bhardwaj, and P.B. Corkum. Fabrication of microchannels in glass using focused femtosecond laser radiation and selective chemical etching. *Applied Physics A*, 84(1):47–61, Jul 2006.
- [13] Yan Li and Shiliang Qu. Water-assisted femtosecond laser ablation for fabricating three-dimensional microfluidic chips. *Current Applied Physics*, 13(7):1292 – 1295, 2013.
- [14] Hiroyuki Degawa, Noriaki Urano, and Shigeki Matsuo. Laser fabrication of miniature internal thread in glass substrate. *Micromachines*, 8(2), 2017.
- [15] David J. Hwang, Moosung Kim, Kuniaki Hiromatsu, Hojeong Jeon, and Costas P. Grigoropoulos. Three-dimensional opto-fluidic devices fabricated by ultrashort laser pulses for high throughput single cell detection and processing. *Applied Physics A*, 96(2):385–390, Aug 2009.
- [16] Moosung Kim, David J. Hwang, Hojeong Jeon, Kuniaki Hiromatsu, and Costas P. Grigoropoulos. Single cell detection using a glass-based optofluidic device fabricated by femtosecond laser pulses. *The Royal Society of Chemistry*, 9(9):311–318, Oct 2008.
- [17] Jian Xu, Dong Wu, Joanna Y. Ip, Katsumi Midorikawa, and Koji Sugioka. Vertical sidewall electrodes monolithically integrated into 3d glass microfluidic chips using water-assisted femtosecond-laser fabrication for in situ control of electrotaxis. *RSC Adv.*, 5:24072–24080, 2015.
- [18] Yves Bellouard, Ali A. Said, and Philippe Bado. Integrating optics and micro-mechanics in a single substrate: a step toward monolithic integration in fused silica. *Opt. Express*, 13(17):6635–6644, Aug 2005.
- [19] Amplitude systemes, 11, Avenue de Canteranne – Cité de la Photonique – Bâtiment Méropa 33600 Pessac – France. *Satsuma HP<sup>2</sup>, air cooled version, User Manual*.
- [20] Ai-Qun Liu Jing Li. Design of mems optical switches. pages 29–37.
- [21] Petr Beckmann and Andre Spizzichino. *The scattering of electromagnetic waves from rough surfaces*. 1987.

- 
- [22] P. K. Tien. Light waves in thin films and integrated optics. *Appl. Opt.*, 10(11):2395–2413, Nov 1971.
- [23] A. Yariv. Coupled-mode theory for guided-wave optics. *IEEE Journal of Quantum Electronics*, 9(9):919–933, Sep. 1973.
- [24] Richard Soref. Tutorial: Integrated-photonics switching structures. *APL Photonics*, 3(021101), 2018.
- [25] G. Guillot L. Pavesi. *Optical Interconnects; The Silicon Approach*. Springer.
- [26] A. Bianco, D. Camerino, D. Cuda, and F. Neri. Optics vs. electronics in future high-capacity switches/routers. In *2009 International Conference on High Performance Switching and Routing*, pages 1–6, June 2009.
- [27] M. C. Wu, O. Solgaard, and J. E. Ford. Optical mems for lightwave communication. *Journal of Lightwave Technology*, 24(12):4433–4454, Dec 2006.
- [28] D. Roy, S. Dutta, B. Kumam, and G. Das. A cost-effective and energy-efficient all-optical access metro-ring integrated network architecture. In *2018 International Conference on Optical Network Design and Modeling (ONDM)*, pages 154–159, May 2018.
- [29] Xi Chen Qian Hu William Shieh Di Che, An Li. Rejuvenating direct modulation and direct detection for modern optical communications. *Optics Communications*, 409:86–93, 2018.
- [30] A. Sciuto S. Libertino. Electro-optical modulators in silicon. [25], pages 53–96.
- [31] Junfeng Song, Xianshu Luo, Xiaoguang Tu, Lianxi Jia, Qing Fang, Tsung-Yang Liow, Mingbin Yu, and Guo-Qiang Lo. On-chip quasi-digital optical switch using silicon microring resonator-coupled mach-zehnder interferometer. *Opt. Express*, 21(10):12767–12775, May 2013.
- [32] Liangjun Lu, Shuoyi Zhao, Linjie Zhou, Dong Li, Zuxiang Li, Minjuan Wang, Xinwan Li, and Jianping Chen. 16 x 16 non-blocking silicon optical switch based on electro-optic mach-zehnder interferometers. *Opt. Express*, 24(9):9295–9307, May 2016.
- [33] Qiao Lei, Tang Weijie, and Chu Tao. 32×32 silicon electro-optic switch with built-in monitors and balanced-status units. *Scientific Reports*, 7(42306), Feb 2017.
- [34] Shuoyi Zhao, Liangjun Lu, Linjie Zhou, Dong Li, Zhanzhi Guo, and Jianping Chen. 16×16 silicon mach-zehnder interferometer switch actuated with waveguide microheaters. *Photon. Res.*, 4(5):202–207, Oct 2016.

- [35] Finisar. *Waveshaper 16000S Multiport Optical Processor*, 2014. Datasheet.
- [36] Volodymyr Borshch, Sergij V. Shiyanovskii, and Oleg D. Lavrentovich. Nanosecond electro-optic switching of a liquid crystal. *Phys. Rev. Lett.*, 111:107802, Sep 2013.
- [37] Fraunhofer IPMS. *Electro-Optical Liquid Crystal Waveguide Switch*, 2018. Datasheet.
- [38] ThorLabs. *Polarization-Independent Optical Shutter / Switch*, 2019. Rev E.
- [39] Q. Cheng, M. Ding, A. Wonfor, J. Wei, R. V. Penty, and I. H. White. The feasibility of building a  $64 \times 64$  port count soa-based optical switch. In *2015 International Conference on Photonics in Switching (PS)*, pages 199–201, Sep. 2015.
- [40] Yutaka Kai, Kyosuke Sone, S. Yoshida, Yasuhiko Aoki, G. Nakagawa, and Susumu Kinoshita. A compact and lossless  $8 \times 8$  soa gate switch subsystem for wdm optical packet interconnections. In *2008 34th European Conference on Optical Communication*, pages 1–2, Sep. 2008.
- [41] FiberZone Networks. *FiberZone’s AFM Product Line*, 2018. Datasheet.
- [42] DiCon Fiberoptics. *VX 1XN Optical Switch*, 2018. Datasheet.
- [43] Huber+Suhner Polatis. *single mode network optical switch up to  $384 \times 384$  ports*, 2017. Rev. 7000n.072017.001.
- [44] ThorLabs. *Optical MEMS switches with specialty Single Mode Fiber*, 2015. Datasheet.
- [45] Yao-Joe Yang, Wen-Cheng Kuo, Kuang-Chao Fan, and Wu-Lang Lin. A  $1 \times 2$  optical fiber switch using a dual-thickness SOI process. *Journal of Micromechanics and Microengineering*, 17(5):1034–1041, apr 2007.
- [46] E. Ollier and P. Mottier. Integrated electrostatic micro-switch for optical fibre networks driven by low voltage. *Electronics Letters*, 32(21):2007–2009, Oct 1996.
- [47] Martin Hoffmann, Peter Kopka, and Edgar Voges. Bistable micromechanical fiber-optic switches on silicon with thermal actuators. *Sensors and Actuators A: Physical*, 78(1):28 – 35, 1999.
- [48] Ming-Chang M. Lee and Ming C. Wu. Tunable coupling regimes of silicon microdisk resonators using mems actuators. *Opt. Express*, 14(11):4703–4712, May 2006.

- [49] G. N. Nielson, D. Seneviratne, F. Lopez-Royo, P. T. Rakich, Y. Avrahami, M. R. Watts, H. A. Haus, H. L. Tuller, and G. Barbastathis. Integrated wavelength-selective optical mems switching using ring resonator filters. *IEEE Photonics Technology Letters*, 17(6):1190–1192, June 2005.
- [50] Chin C. Lee and Tzu J. Su.  $2 \times 2$  single-mode zero-gap directional-coupler thermo-optic waveguide switch on glass. *Appl. Opt.*, 33(30):7016–7022, Oct 1994.
- [51] Joris Van Campenhout, William M. J. Green, Solomon Assefa, and Yurii A. Vlasov. Low-power,  $2 \times 2$  silicon electro-optic switch with 110-nm bandwidth for broadband reconfigurable optical networks. *Opt. Express*, 17(26):24020–24029, Dec 2009.
- [52] M. W. Pruessner, K. Amarnath, M. Datta, D. P. Kelly, S. Kanakaraju, Ping-Tong Ho, and R. Ghodssi. Inp-based optical waveguide mems switches with evanescent coupling mechanism. *Journal of Microelectromechanical Systems*, 14(5):1070–1081, Oct 2005.
- [53] John Elie Sader. Frequency response of cantilever beams immersed in viscous fluids with applications to the atomic force microscope. *Journal of Applied Physics*, 84(64), 1998.
- [54] Chih-Min Yao and Weileun Fang Jiunn-Horng Lee, Sheng-Ta Lee. Comments on the size effect on the microcantilever quality factor in free air space. *J. Micromech. Microeng.*, 17(139), 2007.
- [55] K. M. Davis, K. Miura, N. Sugimoto, and K. Hirao. Writing waveguides in glass with a femtosecond laser. *Opt. Lett.*, 21(21):1729–1731, Nov 1996.
- [56] G. Korn J. Squier D. Du, X. Liu and G. Mourou. Laser-induced breakdown by impact ionization in sio2 with pulse widths from 7 ns to 150 fs. *Applied Physical Letters*, 64(3071), 1994.
- [57] Rafael R. Gattass and Eric Mazur. Femtosecond laser micromachining in transparent materials. *Nature Photonics*, 2(4):219–225, 2008.
- [58] A.P. Joglekar, H. Liu, G.J. Spooner, E. Meyhöfer, G. Mourou, and A.J. Hunt. A study of the deterministic character of optical damage by femtosecond laser pulses and applications to nanomachining. *Applied Physics B*, 77(1):25–30, Aug 2003.
- [59] L. V. Keldysh. Ionization in the field of a strong electromagnetic wave. *Soviet Physics JETP*, 20(5), May 1965.

- [60] Chris B Schaffer, André Brodeur, and Eric Mazur. Laser-induced breakdown and damage in bulk transparent materials induced by tightly focused femtosecond laser pulses. *Measurement Science and Technology*, 12(11):1784–1794, oct 2001.
- [61] B. C. Stuart, M. D. Feit, S. Herman, A. M. Rubenchik, B. W. Shore, and M. D. Perry. Nanosecond-to-femtosecond laser-induced breakdown in dielectrics. *Phys. Rev. B*, 53:1749–1761, Jan 1996.
- [62] M. Lenzner, J. Krüger, S. Sartania, Z. Cheng, Ch. Spielmann, G. Mourou, W. Kautek, and F. Krausz. Femtosecond optical breakdown in dielectrics. *Phys. Rev. Lett.*, 80:4076–4079, May 1998.
- [63] D. Du, X. Liu, and G. Mourou. Reduction of multi-photon ionization in dielectrics due to collisions. *Applied Physics B*, 63(6):617–621, Dec 1996.
- [64] A. Kaiser, B. Rethfeld, M. Vicanek, and G. Simon. Microscopic processes in dielectrics under irradiation by subpicosecond laser pulses. *Phys. Rev. B*, 61:11437–11450, May 2000.
- [65] Lawrence Shah, Alan Y. Arai, Shane M. Eaton, and Peter R. Herman. Waveguide writing in fused silica with a femtosecond fiber laser at 522 nm and 1 mhz repetition rate. *Opt. Express*, 13(6):1999–2006, Mar 2005.
- [66] Jonathan B. Ashcom, Rafael R. Gattass, Chris B. Schaffer, and Eric Mazur. Numerical aperture dependence of damage and supercontinuum generation from femtosecond laser pulses in bulk fused silica. *J. Opt. Soc. Am. B*, 23(11):2317–2322, Nov 2006.
- [67] B. C. Stuart, M. D. Feit, A. M. Rubenchik, B. W. Shore, and M. D. Perry. Laser-induced damage in dielectrics with nanosecond to subpicosecond pulses. *Phys. Rev. Lett.*, 74:2248–2251, Mar 1995.
- [68] D. Du, X. Liu, G. Korn, J. Squier, and G. Mourou. Laser-induced breakdown by impact ionization in sio<sub>2</sub> with pulse widths from 7 ns to 150 fs. *Applied Physics Letters*, 64(23):3071–3073, 1994.
- [69] R. Osellame, N. Chiodo, V. Maselli, A. Yin, M. Zavelani-Rossi, G. Cerullo, P. Laporta, L. Aiello, S. De Nicola, P. Ferraro, A. Finizio, and G. Pierattini. Optical properties of waveguides written by a 26 mhz stretched cavity ti:sapphire femtosecond oscillator. *Opt. Express*, 13(2):612–620, Jan 2005.
- [70] Thomas F. Johnston. Beam propagation (m<sup>2</sup>) measurement made as easy as it gets: the four-cuts method. *Appl. Opt.*, 37(21):4840–4850, Jul 1998.

- [71] Roberto Osellame, Stefano Taccheo, Marco Marangoni, Roberta Ramponi, Paolo Laporta, Dario Polli, Sandro De Silvestri, and Giulio Cerullo. Femtosecond writing of active optical waveguides with astigmatically shaped beams. *J. Opt. Soc. Am. B*, 20(7):1559–1567, Jul 2003.
- [72] M. Ams, G. D. Marshall, D. J. Spence, and M. J. Withford. Slit beam shaping method for femtosecond laser direct-write fabrication of symmetric waveguides in bulk glasses. *Opt. Express*, 13(15):5676–5681, Jul 2005.
- [73] R. R. Thomson, A. S. Bockelt, E. Ramsay, S. Beecher, A. H. Greenaway, A. K. Kar, and D. T. Reid. Shaping ultrafast laser inscribed optical waveguides using a deformable mirror. *Opt. Express*, 16(17):12786–12793, Aug 2008.
- [74] A. Marcinkevičius, V. Mizeikis, S. Juodkazis, S. Matsuo, and H. Misawa. Effect of refractive index-mismatch on laser microfabrication in silica glass. *Applied Physics A*, 76(2):257–260, Feb 2003.
- [75] C. Hnatovsky, R. S. Taylor, E. Simova, V. R. Bhardwaj, D. M. Rayner, and P. B. Corkum. High-resolution study of photoinduced modification in fused silica produced by a tightly focused femtosecond laser beam in the presence of aberrations. *Journal of Applied Physics*, 98(1):013517, 2005.
- [76] R. Osellame, N. Chiodo, G. Della Valle, G. Cerullo, R. Ramponi, P. Laporta, A. Killi, U. Morgner, and O. Svelto. Waveguide lasers in the c-band fabricated by laser inscription with a compact femtosecond oscillator. *IEEE Journal of Selected Topics in Quantum Electronics*, 12(2):277–285, March 2006.
- [77] C.B. Schaffer, J.F. García, and E. Mazur. Bulk heating of transparent materials using a high-repetition-rate femtosecond laser. *Applied Physics A*, 76(3):351–354, Mar 2003.
- [78] Alexander M. Streltsov and Nicholas F. Borrelli. Study of femtosecond-laser-written waveguides in glasses. *J. Opt. Soc. Am. B*, 19(10):2496–2504, Oct 2002.
- [79] J. W. Chan, T. Huser, S. Risbud, and D. M. Krol. Structural changes in fused silica after exposure to focused femtosecond laser pulses. *Opt. Lett.*, 26(21):1726–1728, Nov 2001.
- [80] Masaaki Sakakura, Masahiro Shimizu, Yasuhiko Shimotsuma, Kiyotaka Miura, and Kazuyuki Hirao. Temperature distribution and modification mechanism inside glass with heat accumulation during 250kHz irradiation of femtosecond laser pulses. *Applied Physics Letters*, 93(23):231112, 2008.
- [81] Weijia Yang, Peter G. Kazansky, Yasuhiko Shimotsuma, Masaaki Sakakura, Kiyotaka Miura, and Kazuyuki Hirao. Ultrashort-pulse laser calligraphy. *Applied Physics Letters*, 93(17):171109, 2008.

- [82] A. M. Kowalewicz, V. Sharma, E. P. Ippen, J. G. Fujimoto, and K. Mino-shima. Three-dimensional photonic devices fabricated in glass by use of a femtosecond laser oscillator. *Opt. Lett.*, 30(9):1060–1062, May 2005.
- [83] R. Osellame, V. Maselli, N. Chiodo, D. Polli, R. M. Vazquez, R. Ramponi, and G. Cerullo. Fabrication of 3d photonic devices at 1.55  $\mu\text{m}$  wave-length by femtosecond ti:sapphire oscillator. *Electronics Letters*, 41(6):315–317, March 2005.
- [84] Wataru Watanabe, Taishi Asano, Kazuhiro Yamada, Kazuyoshi Itoh, and Junji Nishii. Wavelength division with three-dimensional couplers fabricated by filamentation of femtosecond laser pulses. *Opt. Lett.*, 28(24):2491–2493, Dec 2003.
- [85] L. Sudrie, M. Franco, B. Prade, and A. Mysyrowicz. Writing of permanent birefringent microlayers in bulk fused silica with femtosecond laser pulses. *Optics Communications*, 171(4-6):279–284, Dec 1999.
- [86] Yasuhiko Shimotsuma, Peter G. Kazansky, Jiarong Qiu, and Kazuoki Hi-rao. Self-organized nanogratings in glass irradiated by ultrashort light pulses. *Phys. Rev. Lett.*, 91:247405, Dec 2003.
- [87] Kazuyoshi Itoh, Wataru Watanabe, Stefan Nolte, and Chris B. Schaffer. Ul-trafast processes for bulk modification of transparent materials. *MRS Bul-letin*, 31(8):620–625, 2006.
- [88] Andrius Marcinkevičius, Saulius Juodkazis, Mitsuru Watanabe, Masafumi Miwa, Shigeki Matsuo, Hiroaki Misawa, and Junji Nishii. Femtosecond laser-assisted three-dimensional microfabrication in silica. *Opt. Lett.*, 26(5):277–279, Mar 2001.
- [89] Yves Bellouard, Ali Said, Mark Dugan, and Philippe Bado. Fabrication of high-aspect ratio, micro-fluidic channels and tunnels using femtosecond laser pulses and chemical etching. *Opt. Express*, 12(10):2120–2129, May 2004.
- [90] Valeria Maselli, Roberto Osellame, Giulio Cerullo, Roberta Ramponi, Paolo Laporta, Luca Magagnin, and Pietro Luigi Cavallotti. Fabrication of long mi-crochannels with circular cross section using astigmatically shaped femtosec-ond laser pulses and chemical etching. *Applied Physics Letters*, 88(19):191107, 2006.
- [91] Anatoliy Y. Vorobyev and Chunlei Guo. Direct femtosecond laser surface nano/microstructuring and its applications. *Laser & Photonics Reviews*, 7(3):385–407, 2013.

- 
- [92] L. Berthe, R. Fabbro, P. Peyre, and E. Bartnicki. Wavelength dependent of laser shock-wave generation in the water-confinement regime. *Journal of Applied Physics*, 85(11):7552–7555, 1999.
- [93] R. Fabbro, P. Peyre, L. Berthe, and X. Scherpereel. Physics and application of laser-shock processing. *Journal of Laser Applications*, 10(6):265–279, 1998.
- [94] Arvi Kruusing. Underwater and water-assisted laser processing: Part 1—general features, steam cleaning and shock processing. *Optics and Lasers in Engineering*, 41(2):307 – 327, 2004.
- [95] Arvi Kruusing. Underwater and water-assisted laser processing: Part 2—etching, cutting and rarely used methods. *Optics and Lasers in Engineering*, 41(2):329 – 352, 2004.
- [96] Xin Zhao and Yung C. Shin. Femtosecond laser drilling of high-aspect ratio microchannels in glass. *Applied Physics A*, 104(2):713–719, 2011.
- [97] Yan Li, Kazuyoshi Itoh, Wataru Watanabe, Kazuhiro Yamada, Daisuke Kuroda, Junji Nishii, and Yongyuan Jiang. Three-dimensional hole drilling of silica glass from the rear surface with femtosecond laser pulses. *Opt. Lett.*, 26(23):1912–1914, Dec 2001.
- [98] Lan Jiang, Pengjun Liu, Xueliang Yan, Ni Leng, Chuancai Xu, Hai Xiao, and Yongfeng Lu. High-throughput rear-surface drilling of microchannels in glass based on electron dynamics control using femtosecond pulse trains. *Opt. Lett.*, 37(14):2781–2783, Jul 2012.
- [99] A. Crespi, S. Longhi, and R. Osellame. Photonic realization of the quantum Rabi model. *Phys. Rev. Lett.*, 108:163601, Apr 2012.



# Ringraziamenti

Innanzitutto, tengo a ringraziare il Dr. Roberto Osellame per avermi dato l'opportunità di lavorare a un progetto poliedrico, che mi ha dato grandi soddisfazioni e che mi ha arricchito sotto molteplici aspetti professionali. Lo ringrazio anche per aver formato un gruppo nel quale è davvero facile lavorare in serenità, ma con grande serietà.

Un sentito ringraziamento va ad Andrea, che si è occupato di guidarmi con scrupolosità e saggezza durante tutto il lavoro sperimentale e di stesura della tesi, preoccupandosi della mia crescita personale, oltre che professionale, battendosi per far sviluppare la mia autonomia e "sbattendosi" per correggere con tempestività le mie bozze piene di errori.

Un grazie enorme va a tutti i membri del gruppo, attuali e non, perchè grazie a loro ho vissuto questa esperienza anche con divertimento. In particolare vorrei ringraziare Michele, che mi ha lasciato in eredità il suo amato progetto e che ha guidato i miei primi passi in questo nuovo mondo, e Roberto, con cui ho condiviso le fatiche per l'ottimizzazione del primo dispositivo. Ringrazio anche Francesco per aver realizzato il trasformatore che ha permesso al mio setup di raggiungere tensioni mai viste, per avermi ispirato l'idea di cambiare il verso di fabbricazione per la simmetria e per quella volta che ha accettato di giocare a calcetto quando ormai le mie speranze stavano per sparire del tutto. Ringrazio i compagni tesisti (ormai molti non più tali), Alessio, Andrea, Ciro, Clement, Federica, Luca, Perto, Valerio, per le chiacchierate ai meeting, per i pranzi in terrazza, per la musica in laboratorio, per gli scherzi a Giacomo sul suo account di Spotify e anche per avermi tirato su il morale con un "per lo meno non fai 2PP". Un grazie speciale a tutti i compagni più esperti non ancora citati, Fede, Francesca, Giacomo, Pelle, Petra, Rebeca, Simo, Simo, chi per aver organizzato le nostre celeberrime uscite di gruppo, chi per avermi ricordato l'esistenza dell'orsetto Ciro, chi per aver condiviso con me le sofferenze per i mille problemi di Satsuma, ma comunque tutti per la grande disponibilità e generosità dimostrate quotidianamente. A particular thanks to Nan for being such a cheerful person and a friend and for sharing with me everything about his very interesting culture.

Vorrei poi ringraziare tutti i miei amici, per essermi stati sempre accanto, chi in ambito universitario, chi nella vita quotidiana, chi in vacanza, perchè durante questo lungo anno di tesi, senza di loro sarebbe stato tutto più noioso, per quanto bello e entusiasmante possa essere lavorare in laboratorio. In particolare ringrazio i colleghi di EDEN, George Best e Albert Dove, per la collaborazione all'avvincente quanto esilarante progetto realizzato in parallelo alla tesi. Ringrazio i Brianzoli (Ari, Fuma, Luca, Lune, Mazza, Ros... e Voicy) per essere stati quelli più presenti e per essere diventati dei drogati di giochi da tavolo come me. Ringrazio Fra, Gre, Pollo, Sofi e Trezzi, perchè, nonostante ci siano meno occasioni per vedersi, riescono tutte le volte a farmi sentire come un tempo. Ringrazio il gruppo Spiaggiata per le bellissime estati che mi fanno passare e per essere riusciti finalmente quest'anno a organizzare quella benedetta pizzata prima di Natale. Ringrazio Macco-e-Mella per le grandi mangiate e per essere sempre sulla mia lunghezza d'onda. Ringrazio Ale per tutte le volte che è uscito con me al Solobirra e per aver tentato invano di farmi capire la sua tesi, nonchè per aver annuito perplesso quando ero io a provare a spiegare la mia. Approfitto per ringraziare Armando, ritrovato dopo tanto tempo: vedrai che prima o poi, io, te e Ale saliremo sul palco...del Madrigal! Ringrazio infine gli altri vecchi amici (Michele, Mark, Sibò, Vale...) perchè basta incontrarli anche solo per caso per tornare alle medie e sentirmi di nuovo bambino.

Un paragrafo speciale va ai miei genitori, che mi hanno sempre spronato a dare il massimo, senza mai chiederlo, dandomi fiducia e congratulandosi quando ottenevo buoni risultati. Grazie a loro sono sempre stato orgoglioso del mio percorso e ho potuto fare le mie scelte in serenità, sentendomi sempre appoggiato. Grazie per avermi permesso di coltivare le mie tante passioni che sono state una valvola di sfogo costante. Vi ringrazio perchè sento che è proprio questo clima che mi ha consentito di crescere e migliorare senza preoccupazioni. Grazie per avermi sostenuto, sia moralmente che materialmente, perchè senza di voi non ce l'avrei mai fatta.

Infine voglio ringraziare Ilaria, ma anche Buffy, Terribilia, Stella marina, il Castoro e... che insieme a lei mi hanno riempito la vita con le loro mille facce buffe. Grazie per esserci sempre, per avermi ascoltato, per avermi dato un parere, aiutandomi a compiere le scelte che non so mai prendere. Grazie per essere un'ispirazione, per permettermi di guidarti, facendomi sentire importante, per giocare con me, per avermi sgridato e spronato a migliorare, per la nostra sintonia, per aver assecondato le mie fisse e per tutte le esperienze che mi fai fare... Ah dimenticavo! Ti ringrazio anche per la consulenza tecnica e ingegneristica, mia cara compagna di studi.